

University of Windsor

Scholarship at UWindor

Electronic Theses and Dissertations

Theses, Dissertations, and Major Papers

2007

Reduced mesoporous and microporous titanium oxide composites as novel hydrogen storage materials

Xin Hu

University of Windsor

Follow this and additional works at: <https://scholar.uwindsor.ca/etd>

Recommended Citation

Hu, Xin, "Reduced mesoporous and microporous titanium oxide composites as novel hydrogen storage materials" (2007). *Electronic Theses and Dissertations*. 8226.

<https://scholar.uwindsor.ca/etd/8226>

This online database contains the full-text of PhD dissertations and Masters' theses of University of Windsor students from 1954 forward. These documents are made available for personal study and research purposes only, in accordance with the Canadian Copyright Act and the Creative Commons license—CC BY-NC-ND (Attribution, Non-Commercial, No Derivative Works). Under this license, works must always be attributed to the copyright holder (original author), cannot be used for any commercial purposes, and may not be altered. Any other use would require the permission of the copyright holder. Students may inquire about withdrawing their dissertation and/or thesis from this database. For additional inquiries, please contact the repository administrator via email (scholarship@uwindsor.ca) or by telephone at 519-253-3000ext. 3208.

**Reduced Mesoporous and Microporous Ti Oxide Composites
as Novel Hydrogen Storage Materials**

by

Xin Hu

A Dissertation

Submitted to the Faculty of Graduate Studies through the Department of
Chemistry and Biochemistry in Partial Fulfillment of the Requirements for
the Degree of Doctor of Philosophy at the
University of Windsor

Windsor, Ontario, Canada
2007

©2007 Xin Hu



Library and
Archives Canada

Published Heritage
Branch

395 Wellington Street
Ottawa ON K1A 0N4
Canada

Bibliothèque et
Archives Canada

Direction du
Patrimoine de l'édition

395, rue Wellington
Ottawa ON K1A 0N4
Canada

Your file Votre référence
ISBN: 978-0-494-47101-2
Our file Notre référence
ISBN: 978-0-494-47101-2

NOTICE:

The author has granted a non-exclusive license allowing Library and Archives Canada to reproduce, publish, archive, preserve, conserve, communicate to the public by telecommunication or on the Internet, loan, distribute and sell theses worldwide, for commercial or non-commercial purposes, in microform, paper, electronic and/or any other formats.

The author retains copyright ownership and moral rights in this thesis. Neither the thesis nor substantial extracts from it may be printed or otherwise reproduced without the author's permission.

AVIS:

L'auteur a accordé une licence non exclusive permettant à la Bibliothèque et Archives Canada de reproduire, publier, archiver, sauvegarder, conserver, transmettre au public par télécommunication ou par l'Internet, prêter, distribuer et vendre des thèses partout dans le monde, à des fins commerciales ou autres, sur support microforme, papier, électronique et/ou autres formats.

L'auteur conserve la propriété du droit d'auteur et des droits moraux qui protègent cette thèse. Ni la thèse ni des extraits substantiels de celle-ci ne doivent être imprimés ou autrement reproduits sans son autorisation.

In compliance with the Canadian Privacy Act some supporting forms may have been removed from this thesis.

Conformément à la loi canadienne sur la protection de la vie privée, quelques formulaires secondaires ont été enlevés de cette thèse.

While these forms may be included in the document page count, their removal does not represent any loss of content from the thesis.

Bien que ces formulaires aient inclus dans la pagination, il n'y aura aucun contenu manquant.


Canada

Abstract

In this work, mesoporous and microporous titanium oxides were reduced and/or impregnated by a variety of reducing agents, such as alkali metals, organometallic sandwich compounds of Ti, V, and Cr, as well as alkali fullerides. These new composite materials were characterized by nitrogen adsorption, powder X-ray diffraction, X-ray photoelectron spectroscopy, Raman spectroscopy and elemental analysis. The hydrogen sorption properties were investigated as a function of surface area, pore size, and reducing agent for these new composite materials at 77 K. Unlike MOFs and porous carbons, the hydrogen sorption performance of these new composite materials does not depend greatly on surface area; however, the reduction in the surface Ti species seems to be the crucial factor in determining hydrogen sorption capacities. For example, microporous Ti oxide reduced with bis(toluene) Ti possesses a surface area of 208 m²/g, but exhibits an overall volumetric storage capacity of 40.46 kg/m³ at 77 K and 100 atm. This volumetric storage capacity is higher than that of pristine material, which has a surface area of 942 m²/g. The improved performance for these reduced composite materials relative to the untreated sample was attributed to the increased reduction level of the metal centers in the framework of the structure, which allows for more facile π -back donation to the H-H σ bond, a factor known to strengthen hydrogen binding to metals. Another surprising feature in these reduced materials is the unusual trend in enthalpies, which show an unprecedented increase in binding strength as the surface coverage increase. The binding enthalpies also increase on progressive reduction, from 4.21 to 8.35 kJ/mol. This highly unusual behavior reflects a different mechanism of

surface binding than simple physisorption, and indicates that further efforts are required to find a suitable reducing reagent in order to reach even higher volumetric storage densities and tune the hydrogen binding enthalpies to over 20 kJ/mol, which is proposed to be ideal value for porous samples operating at ambient temperature.

Acknowledgements

First, I would like to express my deep sense of gratitude to my supervisor Professor David Antonelli for his help, support and friendship along the way. His guidance, patience and insightful knowledge on my research project have inspired me throughout my graduate study.

A special thank goes to Dr. Michel Trudeau who gave me a lot of help with the analysis of XPS and TEM samples. I also want to thank Dr. Nickolas Pieczonka for his help with Raman Spectroscopy measurements.

I am grateful to my committee members Dr. Charles Macdonald, Dr. Jichang Wang and Dr. Derek Northwood for valuable advice and guidance. I also like to thank Faculty and Staff in the Department of Chemistry and Biochemistry. In addition, many thanks are given to our past and present group members: Dr. Boris Skadtchenko, Dr. Abdul Seayad, Dr. Junjie Kang, Mr. Chaoyang Yue, Mr. Yuxiang Rao, Mr. Ahmad Hamaed and Mr. Tuan Hoang for their help and advice.

Last but not least, I would like to thank my wife Linlin Wang, my parents and all my family for their constant love, encouragement and support throughout my life.

Table of Contents

Abstract	iii
Acknowledgements	v
List of Figures	xii
List of Tables	xvii
List of Schemes	xix
List of Abbreviations	xx
Chapter 1. Introduction	1
1.1. Physisorption of Hydrogen	2
1.1.1. Theoretical Hydrogen Storage Investigations of Carbon Nanostructured Materials	4
1.1.2. Experimental Results of Carbon Nanostructured Materials	8
1.1.2.1. Initial Promising Results and Appearance of Discrepancy	8
1.1.2.2. Comparative Hydrogen Storage Studies in Different Carbon Nanostructures	11
1.1.2.3. Hydrogen Storage in Carbon Nanotubes	13
1.1.2.4. Hydrogen Storage in Graphite/Carbon Nanofibers	16
1.1.2.5. Hydrogen Storage in Activated Carbon	18
1.1.2.6. Hydrogen Storage in Other Carbon Nanostructures	19
1.1.2.7. Hydrogen Storage in Carbon Nanostructures by Spillover	21
1.1.3. Hydrogen Storage of Metal Organic Frameworks	23

1.1.4.	Hydrogen Storage of Zeolites	36
1.1.5.	Hydrogen Storage of Clathrates	38
1.2.	Chemisorption of Hydrogen	41
1.2.1.	Hydrogen Storage of Metal Hydrides	42
1.2.2.	Hydrogen Storage of Complex Hydrides	44
1.3.	Hydrogen Storage in Microporous and Mesoporous Ti Oxides	47
Chapter 2.	Hydrogen Storage in Chemically Reducible Mesoporous and Microporous Ti Oxides	51
2.1.	Experimental Section	51
2.1.1.	Materials and Equipment	51
2.1.2.	H ₂ Sorption Measurements	52
2.1.3.	Synthesis	53
2.2.	Results	58
2.2.1.	X-ray Powder Diffraction (XRD) Pattern, Nitrogen Adsorption Study of Unreduced Mesoporous and Microporous Ti Oxides	58
2.2.2.	Hydrogen Sorption Properties of Unreduced Mesoporous and Microporous Ti Oxides	61
2.2.3.	X-ray Powder Diffraction (XRD) Pattern, Nitrogen Adsorption Study of Li, Na and Bis(toluene) Titanium Reduced Microporous Titanium Oxide Materials	66
2.2.4.	Hydrogen Sorption Properties of Li, Na and Bis(toluene) Titanium Reduced Microporous Titanium Oxide Materials	68
2.3.	Discussion	71

2.4.	Conclusion	73
Chapter 3.	Hydrogen Storage in Microporous Titanium Oxides Reduced by Early Transition Metal Organometallic Sandwich Compounds	74
3.1.	Experimental Section	75
3.1.1.	Materials and Equipment	75
3.1.2.	Synthesis	75
3.2.	Results	76
3.2.1.	X-ray Powder Diffraction (XRD) Pattern, Nitrogen Adsorption Study and Elemental Analysis of Bis(benzene) Chromium Reduced Microporous Titanium Oxide Composite	76
3.2.2.	X-ray Photoelectron Spectroscopy (XPS) Studies of Bis(benzene) Chromium Reduced Microporous Titanium Oxide Composite	78
3.2.3.	Hydrogen Sorption Properties of Bis(benzene) Chromium Reduced Microporous Titanium Oxide Composite	80
3.2.4.	X-ray Powder Diffraction (XRD) Pattern, Nitrogen Adsorption Study and Elemental Analysis of Bis(benzene) Vanadium Reduced Microporous Titanium Oxide Composite	84
3.2.5.	X-ray Photoelectron Spectroscopy (XPS) Studies of Bis(benzene) Vanadium Reduced Microporous Titanium Oxide Composite	86
3.2.6.	Hydrogen Sorption Properties of Bis(benzene) Vanadium Reduced Microporous Titanium Oxide Composite	87

3.2.7.	X-ray Powder Diffraction (XRD) Pattern, Nitrogen Adsorption Study and Elemental Analysis of Bis(cyclopentadienyl) Chromium Reduced Microporous Titanium Oxide Composite	88
3.2.8.	X-ray Photoelectron Spectroscopy (XPS) Studies of Bis(cyclopentadienyl) Chromium Reduced Microporous Titanium Oxide Composite	90
3.2.9.	Hydrogen Sorption Properties of Bis(cyclopentadienyl) Chromium Reduced Microporous Titanium Oxide Composite	91
3.2.10.	X-ray Powder Diffraction (XRD) Pattern, Nitrogen Adsorption Study and Elemental Analysis of Bis(cyclopentadienyl) Vanadium Reduced Microporous Titanium Oxide Composite	93
3.2.11.	X-ray Photoelectron Spectroscopy (XPS) Studies of Bis(cyclopentadienyl) Vanadium Reduced Microporous Titanium Oxide Composite	94
3.2.12.	Hydrogen Sorption Properties of Bis(cyclopentadienyl) Vanadium Reduced Microporous Titanium Oxide Composite	96
3.3.	Discussion	96
3.4.	Conclusion	99
Chapter 4.	Hydrogen Storage in Mesoporous Titanium Oxides Alkali Fullerides Composites	101
4.1.	Experimental Section	102
4.1.1.	Materials and Equipment	102

4.1.2.	Synthesis	103
4.2.	Results	104
4.2.1.	X-ray Powder Diffraction (XRD) Pattern, Nitrogen Adsorption Study, Raman Spectroscopy and Elemental Analysis of Na Fulleride Composites	104
4.2.2.	Hydrogen Sorption Properties of Na Fulleride Composites	108
4.2.3.	X-ray Powder Diffraction (XRD) Pattern, Nitrogen Adsorption Study, Elemental Analysis and Raman Spectroscopy of Li Fulleride Composite	115
4.2.4.	Hydrogen Sorption Properties of Li Fulleride Composite	117
4.3.	Discussion	117
4.4.	Conclusion	119
Chapter 5.	Conclusion	121
Appendix	Hydrogen Storage of Chemically Reduced Mesoporous Ti Oxides at High Temperature.	126
A.1.	Experimental Section	126
A.1.1.	Materials and Equipment	126
A.1.2.	Synthesis	127
A.2.	Results	130
A.2.1.	Hydrogen Sorption Properties of Alkali Fullerides Reduced Mesoporous Ti Oxides	130

A.2.2.	Hydrogen Sorption Properties of Organometallic Compounds	137
	Reduced Mesoporous Ti Oxides	
A.2.3.	Hydrogen Sorption Properties of LiAlH₄ and NaBH₄ Reduced	146
	Mesoporous Ti Oxides	
A.2.4.	Hydrogen Sorption Properties of Superhydride Reduced	148
	Mesoporous Ti Oxides	
A.3.	Summary	149
References		150
VITA AUCTORIS		165

List of Figures

Figure	Description	Page
1.	Hydrogen adsorption isotherm for LiNi ₅ at room temperature.	54
2.	Hydrogen adsorption isotherm for AX-21 at 77 K.	55
3.	XRD spectra of a) C6-Ti, b) C8-Ti, c) C10-Ti, d) C12-Ti, e) C14-Ti.	60
4.	Nitrogen adsorption/desorption isotherms of a) C6-Ti, b) C8-Ti, c) C10-Ti, d) C12-Ti, e) C14-Ti.	60
5.	TEM image of C6-Ti.	61
6.	(a) Hydrogen storage isotherms, (b) hydrogen adsorption isotherms for all the unreduced Ti materials.	62
7.	Schematic representation of H ₂ binding sites in the monolayer wall of micro-and mesoporous titanium materials.	65
8.	Enthalpies of H ₂ adsorption for pristine Ti oxide materials.	66
9.	XRD spectra of a) C6-Ti, b) Li C6-Ti, c) Na C6-Ti, d) BTTi C6-Ti.	67
10.	Nitrogen adsorption/desorption isotherms of a) C6-Ti, b) Li C6-Ti, c) Na C6-Ti, d) BTTi C6-Ti.	67
11.	High-pressure H ₂ isotherms for pristine and reduced C6-Ti materials at 77 K in gravimetric uptake.	69
12.	Hydrogen storage capacity in a 10 cycle test of BTTi C6-Ti at 77 K and 65 atm.	70

13.	Enthalpies of H ₂ adsorption for pristine and Li, Na and bis(toluenes) titanium reduced microporous titanium oxides.	70
14.	XRD of microporous titanium oxide before (upper) and after (lower) treatment with excess bis(benzene) chromium.	77
15.	Nitrogen adsorption/desorption isotherms of microporous Ti oxide before (upper) and after (lower) treatment with bis(benzene) chromium	78
16.	XPS spectra of microporous titanium oxide treated with excess bis(benzene) chromium showing the (a) Ti 3p 1/2, 3/2 regions, (b) Cr 2p 1/2, 3/2 regions.	79
17.	Gravimetric high-pressure H ₂ isotherms for C6-Ti, Bisben Cr-Ti and Bisben V-Ti at 77 K.	82
18.	Enthalpies of H ₂ adsorption for pristine and bis-arene and bis-cyclopentadienyl transition-metal-reduced microporous titanium oxides.	83
19.	XRD of microporous titanium oxide before (upper) and after (lower) treatment with excess bis(benzene) vanadium.	84
20.	Nitrogen adsorption/desorption isotherms of microporous Ti oxide before (upper) and after (lower) treatment with bis(benzene) vanadium.	85
21.	XPS spectra of microporous titanium oxide treated with excess bis(benzene) vanadium showing the (a) Ti 3p 1/2, 3/2 regions, (b) V 2p 1/2, 3/2 regions.	87

22.	XRD of microporous titanium oxide before (upper) and after (lower) treatment with excess bis(cyclopentadienyl) chromium.	89
23.	Nitrogen adsorption/desorption isotherms of microporous Ti oxide before (upper) and after (lower) treatment with bis(cyclopentadienyl) chromium.	90
24.	XPS spectra of microporous titanium oxide treated with excess bis(cyclopentadienyl) chromium showing the (a) Ti 3p 1/2, 3/2 regions, (b) Cr 2p 1/2, 3/2 regions.	91
25.	Gravimetric high-pressure H ₂ isotherms for C6-Ti, Biscp Cr-Ti and Biscp V-Ti at 77 K.	92
26.	XRD of microporous titanium oxide before (upper) and after (lower) treatment with excess bis(cyclopentadienyl) vanadium.	93
27.	Nitrogen adsorption/desorption isotherms of microporous Ti oxide before (upper) and after (lower) treatment with bis(cyclopentadienyl) vanadium.	94
28.	XPS spectra of microporous titanium oxide treated with excess bis(cyclopentadienyl) vanadium showing the a) Ti 3p 1/2, 3/2 regions, b) V 2p 1/2, 3/2 regions.	95
29.	Plot of XPS Ti 3p 1/2 binding energy vs. the hydrogen volumetric storage capacity for all the C6-Ti samples.	99
30.	(a) XRD of mesoporous titanium oxide before (upper) and after (lower) treatment with excess Na ₃ C ₆₀ , (b) XRD of mesoporous titanium oxide before (upper) and after (lower) intercalated with	105

- excess Na_3C_{60} and further reduction by 4 eqv. of Na -naphthalene.
31. (a) Nitrogen adsorption/desorption isotherms of mesoporous titanium oxide before (upper) and after (lower) treatment with excess Na_3C_{60} and (b) Nitrogen adsorption/desorption isotherms of mesoporous titanium oxide before (upper) and after (lower) intercalated with excess Na_3C_{60} and further reduction by 4 eqv. of Na -naphthalene. 106
 32. Raman spectra of (a) Na_3C_{60} Ti, (b) Na- Na_3C_{60} Ti and (c) Li- C_{60} Ti. 108
 33. High-pressure H_2 isotherms for (a) C12-Ti, Na_3C_{60} Ti and Na- Na_3C_{60} Ti and (b) C12-Ti and Li- C_{60} Ti at 77 K in gravimetric uptake. 109
 34. High-pressure H_2 isotherms of gravimetric storage for the alkali fullerides impregnated composites and unreduced material at (a) room temperature and (b) 200° C. 114
 35. Enthalpies of H_2 adsorption for pristine and alkali fulleride reduced mesoporous titanium oxides. 115
 36. XRD of mesoporous titanium oxide before (upper) and after (lower) treatment with 1 eqv. of Li-naphthalene then doped with maximum C_{60} . 116
 37. Nitrogen adsorption/desorption isotherms of mesoporous titanium oxide before (upper) and after (lower) treatment with 1 eqv. of Li-naphthalene then doped with maximum C_{60} . 116
 38. Hydrogen adsorption-desorption isotherm at 200 °C of mesoporous titanium oxide reduced with 1 eqv. of Li-naphthalene and treated with maximum C_{60} . 131

39.	Hydrogen adsorption-desorption isotherm of pristine mesoporous titanium oxide at 200 °C.	131
40.	Hydrogen adsorption-desorption isotherms of (a) 1 , (b) 3 at 200°C.	132
41.	Hydrogen adsorption-desorption isotherm of 4 at 200°C.	133
42.	Hydrogen adsorption-desorption isotherms of (a) 5 , and (b) 6 at 150°C.	134
43.	Hydrogen adsorption-desorption isotherms of (a) 7 , and (b) 8 at 150°C.	135
44.	Hydrogen adsorption-desorption isotherm at 200°C of mesoporous titanium oxide treated with excess bis(toluene) titanium.	137
45.	Hydrogen adsorption-desorption isotherms of (A) 9 , (B) 10 .	138
46.	Hydrogen adsorption-desorption isotherm of 11 .	139
47.	Hydrogen adsorption-desorption isotherms of (a) 18 , (b) 19 at 150 °C.	142
48.	Hydrogen adsorption-desorption isotherm of 21 at 200°C.	144
49.	Hydrogen adsorption-desorption isotherms of (a) 22 , (b) 23 at 150 °C.	145
50.	Hydrogen adsorption-desorption isotherm of 24 at 200 °C.	147
51.	Hydrogen adsorption-desorption isotherm of 25 at 200 °C.	147

List of Tables

		Page
Table 1.	The most important families of hydride-forming intermetallic compounds.	43
Table 2.	Nitrogen adsorption and XRD results of Ti oxide materials.	59
Table 3.	Hydrogen sorption capacities of pristine and reduced Ti oxide materials and AX-21.	64
Table 4.	XPS results for pristine and reduced amine-templated materials.	73
Table 5.	Hydrogen sorption capacities of pristine and reduced C6-Ti materials and AX-21.	82
Table 6.	Elemental analysis values for samples of mesoporous titanium oxides before and after intercalation with alkali fullerenes.	108
Table 7.	Hydrogen sorption capacities of pristine C12-Ti and corresponding reduced materials at 77 K.	112
Table 8.	Hydrogen sorption capacities of pristine and corresponding reduced C12-Ti materials at RT and 200°C.	113
Table 9.	Hydrogen adsorption data for Li reduced mesoporous TiO ₂ doped with C ₆₀ and mesoporous Ti oxides doped with Na ₃ C ₆₀ .	136
Table 10.	Hydrogen sorption data for mesoporous TiO ₂ reduced using different methods.	140
Table 11.	Hydrogen sorption data for mesoporous TiO ₂ reduced with TiCl ₄ and Li-naphthalene.	141

Table 12.	Hydrogen sorption data for mesoporous TiO ₂ reduced with bis(benzene) vanadium.	145
Table 13.	Hydrogen sorption data for mesoporous TiO ₂ reduced with super-hydride.	148

List of Schemes

		Page
Scheme 1.	Schematic illustration of a molecular hydrogen complex.	49
Scheme 2.	Schematic representation of σ H ₂ bonding and π H ₂ antibonding in a Kubas-type interaction.	49
Scheme 3.	Schematic illustration of the change in trend of hydrogen enthalpies from physisorption to chemisorption.	50
Scheme 4.	Schematic drawing of Gas Reaction Controller system manufactured by Advanced Materials Corporation.	53

List of Abbreviations:

Department of Energy	DOE
Carbon Nanotubes	CNTs
Grand Canonical Monte Carlo	GCMC
Single-walled Carbon Nanotubes	SWNTs
Graphitic Nanofibers	GNFs
Double-walled Carbon Nanotubes	DWNTs
Carbon Nanofibers	CNFs
Density Functional Theory	DFT
Multi-walled Carbon Nanotubes	MWNTs
Temperature Programmed Desorption	TPD
Activated Carbon	AC
Brunauer-Emmet-Teller	BET
Temperature Desorption Spectroscopy	TDS
Carbon Aerogel	CA
Carbide Derived Carbons	CDC
Metal Organic Frameworks	MOFs
Activated Carbon Fibers	ACFs
Chemical Vapor Deposition	CVD
1,4-benzenedicarboxylates	BDC
Microporous Metal Coordination Material	MMOM
1,3,5-benzene tricarboxylate	BTC

Aluminophosphates	AlPOs
Powder X-ray diffraction	PXRD
Tetrahydrofuran	THF
Transmission Electron Microscopy	TEM
X-ray Diffraction	XRD
X-ray Photoelectron Spectroscopy	XPS
Trimethylsilyl Chloride	TMSCl
Inductively Coupled Plasma	ICP
N,N-dimethylformamide	DMF
Barret-Joyner-Halenda	BJH
Isorecticular Metal Organic Frameworks	IRMOF
Octahedral	Oh
Scanning Electron Microscopy	SEM
Energy Dispersive Spectroscopy	EDS
Cyclopentadienyl	Cp
Microporous Ti Synthesized by Hexylamine Template	C6-Ti
Microporous Ti Synthesized by Octylamine Template	C8-Ti
Mesoporous Ti Synthesized by Decylamine Template	C10-Ti
Mesoporous Ti Synthesized by Dodecylamine Template	C12-Ti
Mesoporous Ti synthesized by tetradecylamine template	C14-Ti
C6-Ti Reduced by 1 Equivalent of Li-naphthalene	Li C6-Ti
C6-Ti Reduced by 1 Equivalent of Na-naphthalene	Na C6-Ti
C6-Ti Reduced by Excess Bis(toluene)Ti	BTTi C6-Ti

C6-Ti Reduced by Excess Bis(benzene)Cr	Bisben Cr-Ti
C6-Ti Reduced by Excess Bis(benzene)V	Bisben V-Ti
C6-Ti Reduced by Excess Bis(cyclopentadienyl) Cr	Biscp Cr-Ti
C6-Ti Reduced by Excess Bis(cyclopentadienyl) V	Biscp V-Ti
C12-Ti Reduced by Excess Na ₃ C ₆₀	Na ₃ C ₆₀ Ti
C12-Ti Reduced by 1 Equivalent of Li-naphthalene then doped with Maximum C ₆₀	Li-C ₆₀ Ti
Na ₃ C ₆₀ Ti Reduced by 4 Equivalent of Na-naphthalene with respective to C ₆₀ in Na ₃ C ₆₀ Ti	Na-Na ₃ C ₆₀ Ti
C12-Ti Reduced by 1 Equivalent of Li-naphthalene	Li C12-Ti
C12-Ti Reduced by 1 Equivalent of Na-naphthalene	Na C12-Ti

Chapter 1. Introduction

The demand for an efficient and clean fuel alternative has increased in the past decade and is expected to become more pronounced in the future, as fossil fuel supply will become increasingly limited. Hydrogen represents an ideal alternative as a fuel since it exhibits the highest heating value per mass of all the chemical fuels. Furthermore, it is also the most abundant element in the universe,¹ it can be readily synthesized, and when used in a fuel cell with oxygen produces only water as a byproduct, i.e., it is environmentally friendly. However, the main concern to date is the safe and efficient transport of this extremely flammable gas. Two different storage technologies are conventionally used, i.e. high pressure gas cylinders and liquid hydrogen in cryogenic vessels.² But the former suffers from low storage density and safety concerns due to the high pressures required, while the large amount of energy required for liquefaction and continuous boil-off of liquid hydrogen are significant drawbacks for the latter. To overcome these problems, solids which absorb hydrogen reversibly with high gravimetric and volumetric density and operate under moderate temperature and pressure may be used as carriers. In spite of the recent surge in interest, hydrogen storage has been a materials science challenge for decades. The goal is to pack hydrogen as close as possible to achieve the highest volumetric and gravimetric density. The second important criterion for a hydrogen storage system is the reversibility of uptake and release. The U.S. Department of Energy (DOE) has set 9.0 wt% and 81 kg H₂/m³ as the 2015 system targets. The main challenges in the field of hydrogen storage are to devise new materials that 1) are inexpensive to manufacture in large quantities in a pure form, 2) have high

gravimetric and volumetric density, 3) exhibit fast sorption kinetics at near-ambient temperature, 4) have a high tolerance of recycling. One of the most promising classes of materials for hydrogen storage are nanostructured composites, because they have dramatically different chemical, physical, thermodynamic and transport properties as compared to their bulk counterparts. Due to the wide range of compositions, the ability to tailor pore and grain sizes, and the capacity to intimately weave two or more phases together at the nanometer level, nanophase composite materials may open the window to greater hydrogen storage capacities and lower kinetic adsorption barriers as compared to the coarse grained materials. Three basic storage mechanisms can be proposed for hydrogen storage in solid materials: i) the physisorption of hydrogen on materials with a large specific surface area, ii) hydrogen absorbed on interstitial sites in a host metal and iii) hydrogen chemically bonded in covalent and ionic compounds. All these principles will be commented on in this chapter.

1.1 Physisorption of Hydrogen

Physisorption is a principle where the weak intermolecular forces (van der Waals forces) are involved, which does not cause any significant change in the electronic orbital patterns of the relevant species. Responsible for this phenomenon is a combination of attractive dispersive (or van der Waals) interactions and short range repulsive interactions between the adsorbent and the adsorbate molecules. This results in a minimum in the potential energy curve of the gas at approximately one molecular radius from the solid surface. The attractive interaction originates from long-range forces produced by

fluctuations in the charge distribution of the gas molecules and of the atoms on the surface, giving rise to attraction between temporary fluctuating and induced dipoles. However, at small distances the overlap between the electron cloud of the gas molecule and of the substrate is significant and the repulsion increases rapidly. Once a monolayer of adsorbate molecules or atoms has formed, the gaseous species interacts with the liquid or solid adsorbate. Therefore, the binding energy of the second layer of adsorbates is similar to the latent heat of sublimation or vaporization of the adsorbate. Consequently, adsorption at a temperature at or above the boiling point of the adsorbate at a given pressure leads to the adsorption of a single monolayer. Compared with hydrogen storage in metal hydrides and complex hydrides, physical adsorption has the great advantage of being completely reversible and of exhibiting very fast kinetics. In addition, since a very small amount of energy ($< 10 \text{ kJ mol}^{-1}$) is involved both in the adsorption and the release of H_2 , no extra heat management systems are therefore required for on-board applications. On the other hand, because of the low adsorption enthalpy involved in physisorption, typically temperature of about 80 K is necessary to reach high storage capacities.

Carbon nanostructured materials³⁻¹⁰ have received the most attention in this area due to their low density, high surface area, extensive pore structure, wide variety of structure forms, good chemical stability and amenability to a wide range of preparation, carbonization and activation conditions. Newly found carbon nanostructures include activated carbon, carbon nanotube and carbon nanofiber etc. A critical review of hydrogen storage in carbon materials both theoretically and experimentally will be given in this context.

1.1.1 Theoretical Hydrogen Storage Investigations of Carbon Nanostructured Materials

Many theoretical studies have been performed to predict the hydrogen sorption in carbon nanostructured materials utilizing grand canonical Monte Carlo (GCMC) simulations.¹¹⁻¹⁹ Rzepka *et al.*¹¹ investigated the physisorption of hydrogen molecules on the surface atoms of carbon slit pores and carbon nanotubes (CNTs) using GCMC calculations. At room temperature and 10 MPa, a gravimetric storage capacity of 1.3 wt% could be achieved for the optimum pore geometry, where a slit pore consists of two graphitic layers separated by a distance that corresponds to approximately twice the diameter of a hydrogen molecule. Later, Williams and Eklund¹² performed GCMC simulation of H₂ physisorption in finite-diameter ropes of carbon single-walled carbon nanotubes (SWNTs). The strong dependence of the gravimetric adsorption on the diameter of a SWNT rope was found to be correlated with computed values of the specific surface area. They suggested that delamination of nanotube ropes should increase the gravimetric storage capacity. A maximum hydrogen storage capacity of 9.6 wt% was calculated for an isolated SWNT. Wang and Johnson¹³ calculated the hydrogen adsorption isotherms in SWNT arrays, isolated SWNTs, AX-21 activated carbon and idealized carbon slit pores, respectively. The idealized slit pores gave significant better performance for hydrogen storage than SWNT arrays. Whereas, the gravimetric density of hydrogen in isolated tubes at 77 K and 50 atm was well above that for the AX-21 activated carbon and the idealized slit pore, which indicated that the packing geometry of the SWNTs played an important role in hydrogen storage. Furthermore, they¹⁴ optimized

the packing geometry of SWNTs to enhance their hydrogen uptake abilities. It was found that the (9, 9) SWNTs with an intertube distance of 0.9 nm had volumetric density of 60 kg/m³ at 77 K and 10 MPa. In another study, they¹⁵ calculated the hydrogen adsorption for graphitic nanofibers (GNFs). The maximum hydrogen uptake of 1.6 wt% was obtained for a GNF with a pore width of 9 Å at 298 K and 50 atm. Darkrim *et al.*¹⁶ computed the hydrogen adsorption in two arrangements of open SWNTs by Monte Carlo simulations. The simulation predicted maximal hydrogen adsorption of 11.24 wt % for the 2.2 nm diameter tube with a square arranged lattice at 77 K and 10 MPa. Yin *et al.*¹⁷ performed GCMC simulations on hydrogen storage in a triangular array of SWNTs and in slit pores at 298 K and 77 K. The maximum hydrogen adsorption capacity of 4.7 wt % was obtained for the SWNTs with a diameter of 6.0 nm and intertube spacing of 1.0 nm at 298 K and 10 MPa. The simulation predicted that the storage capacity could reach the gravimetric DOE target of 2010 at low temperatures for this sample. Guay *et al.*¹⁸ investigated the hydrogen storage behavior of SWNTs, double-walled carbon nanotubes (DWNTs) and carbon nanofibers (CNFs) using the GCMC method. The amount of hydrogen uptake was strongly influenced by the structure porosity and a maximum capacity of 1.4 wt% could be achieved for the nanostructured carbons with optimum pore diameter of around 0.7 nm at 293 K and 10 MPa. Volpe and Cleri¹⁹ studied the hydrogen sorption in chemically modified matrices of SWNTs by using a combination of tight-binding molecular dynamics and GCMC. A maximum hydrogen uptake capacity of 3.4 wt% was achieved for the SWNTs with an optimized diameter of 11.7Å arranged in a square lattice with a wall-to-wall intertube distance of 7 Å at 293 K and 10 MPa.

In order to study the formation of carbon-hydrogen bonds, density functional theory (DFT) and *ab initio* calculations have been performed by several groups recently. Lee *et al.*²⁰ have reported results of calculation for hydrogen storage behavior in SWNTs by DFT calculations at zero Kelvin and found two chemisorption sites at top sites of the exterior and the interior of the tube wall. Their calculation predicted that the hydrogen storage capacity in (10, 10) nanotube can exceed 14 wt %. Later of that year, they²¹ gave a comprehensive study on hydrogen storage in SWNTs and multi-walled carbon nanotubes (MWNTs) by performing density-functional-based tight-binding calculations. It was found that the storage capacity of hydrogen increased linearly with tube diameters in SWNTs and a maximum uptake of 14 wt% can be predicted, whereas hydrogen storage capacity was independent of diameter in MWNTs and a maximum uptake of 7.7 wt% was estimated. In a further work, they investigated the hydrogen-adsorption mechanism in the (5, 5) SWNTs with DFT calculations at zero temperature.²² The hydrogen atoms first adsorbed on the tube wall and then were stored in the capillary as a form of H₂ molecule at higher coverage. Instead of the capillary effect through the ends of the nanotubes, the H₂ can be stored in the capillary through the tube wall by flip-in and kick-in mechanism, while preserving the wall stability of a nanotube. The authors claimed that this calculation may describe an electrochemical storage process of hydrogen, which is applicable for the secondary hydrogen battery. Moreover, Ma *et al.*²³ studied the hydrogen-storage behaviour of (5, 5) SWNTs using molecular dynamics simulations and *ab initio* electronic calculations. Hydrogen atoms with kinetic energy of 16-25 eV were found to penetrate and be trapped into the tube. The hydrogen storage capacity for a (5, 5) SWNT can be 5 wt% and 132.4 kg/m³ in gravimetric and volumetric

density, respectively. Zhang *et al.*²⁴ studied the adsorption of hydrogen on SWNTs with different diameters by a combination of the classical potential and DFT methods. A maximum value of around 1 wt% was obtained at 20 MPa for the isolated SWNT sample at room temperature. At 77 K and 4 MPa, maximum gravimetric capacities of 7.1 wt% and 9.5 wt% could be achieved for, respectively, bundled and isolated SWNTs with diameter of 2.719 nm. Bauschlicher *et al.*²⁵ calculated the binding energy of H to a (10, 0) CNT at different H coverage using the AM1 and ONIOM approaches. It was found that the 50% H coverage on the carbon nanotube was the most favourable in this study, which corresponds to about 4 wt% of hydrogen storage capacity. Cheng *et al.*²⁶ performed analysis of quantum-mechanical molecular dynamics simulations of hydrogen binding energies in (9, 9) SWNTs, of which 7.51 and 6.75 kcal/mol were obtained at 300 K for the inside tube configuration and the outside tube configuration, respectively. They argued that partial electron-transfer interaction between hydrogen and instantaneously distorted carbon atoms in the SWNT wall was the primary reason for the high hydrogen-SWNT adsorption energy. Han *et al.*²⁷ investigated the interaction of H₂ on the exterior surface of single-walled and bundle CNTs by using molecular dynamics simulations. An interesting phenomenon of hydrogen gas molecules transformed into a liquid phase on the surface of a CNT bundle was observed at 80 K and 10 MPa. This is due to the long-range electrostatic interaction of polarized charges on the deformed CNT bundles with the H₂ molecule. The authors claimed that the H₂ gas might liquefy at the temperature higher than 80 K on a more strongly polarized CNT bundle. Lee *et al.*²⁸ reported the hydrogen storage capacity and desorption mechanisms of Ni-dispersed CNTs by DFT methods and experimental methods. It was calculated that each Ni dispersed on the

surface of CNTs could store up to five hydrogen molecules with an enthalpy change of 0.26 eV/H₂ in hydrogen adsorption, which is consistent with the 0.32 eV/H₂ from the experiment. Furthermore, the maximum H₂ uptake of 10 wt% was predicted for a high Ni-coverage, Ni-dispersed SWNT at room temperature.

1.1.2 Experimental Results For Carbon Nanostructured Materials

1.1.2.1 Initial Promising Results and Appearance of Discrepancy

In 1997, Dillon *et al.* first reported the hydrogen storage properties for the SWNTs. They measured the hydrogen uptake of a small quantity of soot containing 0.1-0.2 wt% SWNTs at room temperature.²⁹ Hydrogen adsorption capacity for pure SWNTs was estimated in the range of 5-10 wt%. A high heat of adsorption of 19.6 kJ/mol was also obtained. The authors claimed that hydrogen can condense to high density inside narrow SWNTs and predicted that SWNTs with a diameter of 1.63 and 2 nm would come close to the target hydrogen uptake density of 6.5 wt% set by the DOE. Later, They³⁰ reported that they have directly measured a hydrogen storage capacity of about 7 wt% after purifying the samples and opening the SWNTs. However, Hirscher *et al.*³¹ clarified the situation and showed that the Ti alloy particles in the sample introduced during the ultrasonic treatment were responsible for most of the hydrogen storage capacity of SWNTs. In further studies, they^{32, 33} reported a low hydrogen storage capacity of 1.0 wt % for purified SWNTs, 0.5 wt% for GNFs and 0.3 wt% for graphite. They noted that the reported positive results of hydrogen storage in CNTs had not been repeated or confirmed

independently at other laboratories. Also, more recent reports by Heben's group^{34, 35} showed significantly lower hydrogen storage capacities of 2-3 wt% for SWNTs.

In 1999, Ye *et al.*³⁶ reported a hydrogen storage capacity of 8 wt% for crystalline ropes of SWNTs at a cryogenic temperature of 80 K and pressure higher than 12 MPa. They suggested that the tube bundle structure expanded under high pressure to enable higher adsorption on newly uncovered surface. Liu *et al.*³⁷ reported that a hydrogen storage capacity of 4.2 wt% could be reached at room temperature and 10 MPa for SWNTs synthesized by the hydrogen arc discharge method and with a larger mean diameter of 1.85 nm. However, about 20% of the absorbed hydrogen remained in the sample after desorption at room temperature. More inspiring, Chambers *et al.*³⁸ reported extremely high hydrogen storage capacities of up to 67 wt% for a herringbone-type CNF at room temperature and 110 atm. In a further study³⁹ they reported results on the interaction of hydrogen with GNFs and proposed that the high hydrogen uptake was due to the special structural conformation of GNF, which can produce a material composed entirely of nanopores that accommodate the H₂ molecules. They also pointed out that the pretreatment of samples before hydrogen storage is very important. These extremely high values, however, could not be confirmed in any laboratory up to now. For example, Ahn *et al.*⁴⁰ found in GNFs applying the volumetric method with a pressure of 8 MPa at 77 K and 18 MPa at 300 K less than 0.01 wt% hydrogen storage. In another work, Tibbetts *et al.*⁴¹ examined different carbon materials (e.g. nanotubes, carbon fibers, high surface area activated carbons) at high pressure but they found the maximum hydrogen uptake for all the samples was less than 0.1 wt% under room temperature and 3.5 MPa. They claimed that hydrogen storage capacity higher than 1 wt% for carbon materials at room

temperature was due to the experimental errors. Ritschel and co-workers⁴² also investigated the hydrogen adsorption of different carbon nanostructured materials at room temperature and high pressure up to 45 bar. The measurement showed limit hydrogen storage capacity for all the samples, which is less than 0.7 wt%. Moreover, Lueking *et al.*⁴³ studied the microstructures and hydrogen storage properties of various CNFs synthesized from different carbon sources and catalysts, and then subjected to various pre-treatments. The CNF possessing a herringbone structure and a high degree of defects exhibited the best performance for hydrogen storage, and a maximum hydrogen desorption capacity of 3.8 wt% was achieved at 69 bar and room temperature. However, this value is much lower than the result previously reported.³⁸

In 1999, Fan *et al.*⁴⁴ investigated the hydrogen absorption of vapor-grown CNFs with a diameter of 5 nm to 300 nm. The maximum hydrogen uptake of 12.38 wt% was obtained at room temperature and 110 atm. The nanofibers had to be boiled in hydrochloric acid before hydrogen storage test. However, in a further publication, the same group⁴⁵ reduced the storage capacity of the CNFs by a factor of two. In the same year, Chen *et al.*⁴⁶ reported in their temperature programmed desorption (TPD) experimental investigation that a high hydrogen uptake of 20 wt% and 14 wt% could be achieved in Li-doped and K-doped MWNTs, respectively at a pressure of 1 atm. However, their results have been taken into doubt by Yang.⁴⁷ Yang repeated their experiments and pointed out that it was the moisture in the hydrogen gas that drastically increased the weight gain by reactions with (or adsorption on) the alkali species on carbon, while the contribution of hydrogen storage might be limited. This conclusion has been supported by Skakalova and co-workers.⁴⁸ In addition, Pinkerton *et al.*⁴⁹ investigated the hydrogen storage properties of

Li-doped CNTs and Li- and K- intercalated graphite and found the K-intercalated graphite showed hydrogen adsorption of 1.3 wt%, while no hydrogen adsorption can be observed for the Li-containing carbon samples.

This discrepancy in the hydrogen storage abilities of carbon nanostructures is considered to be due to difficulties in accurate measurements, impurities in the sample and poor understanding of hydrogen sorption mechanism. Since then, scientists have made strong efforts to identify factors such as measurement methodology, material structure characterization, and synthesis techniques that influence the hydrogen storage capacity of carbon nanostructures. Subsequently, both positive and negative results were reported by different groups.

1.1.2.2. Comparative Hydrogen Storage Studies in Different Carbon Nanostructures

In 2001, Nijkamp *et al.*⁵⁰ reported the hydrogen storage capacities for a wide variety of carbonaceous sorbents, microporous zeolites and non-porous materials at 77 K and up to a pressure of 1 bar. The reversible physisorption took place exclusively in all samples. The approximately linear relationship between the hydrogen uptake capacity and the surface area of samples was proposed. This similar correlation between these two factors was further examined by Zuttel and coworkers.^{51, 52} In another study, Kajiura *et al.*⁵³ measured the hydrogen storage capacities for a various commercially available carbon materials at room temperature and up to 8 MPa. The highest storage capacity was just 0.43 wt% for a purified SWNT. These low values are consistent with previously reported results,⁴¹ which indicating that carbon materials are not suitable for hydrogen storage at

room temperature. Poirier *et al.*⁵⁴ investigated the hydrogen adsorption on high specific surface area activated carbon (AC), CNFs and SWNTs based on experimental and theoretical considerations. Some titanium free SWNTs appeared to surpass large surface area ACs in hydrogen uptake capacity both at room temperature and in cryogenic conditions. Hydrogen adsorption capacities of 0.2 wt% and 4 wt% were obtained for the SWNTs at 1 bar and room temperature and 1 bar and 77 K, respectively. It was proposed that due to the specific bundle structure, the SWNTs could favour hydrogen adsorption over the layered graphitic structures typically found in ACs. Schimmel *et al.*^{55, 56} investigated the hydrogen storage capacities of activated charcoal, CNFs and SWNTs. They found that the hydrogen adsorption capacities of these materials correlated with their corresponding surface areas. The activated charcoal with the surface area of 2200 m²/g showed the highest hydrogen adsorption of 2.2 wt% at 1 bar and 77 K. The adsorption potential of the activated charcoal was found to be 5 kJ/mol, which is in agreement with the result of Benard and coworkers.⁵⁷ Hirscher *et al.*^{58, 59} investigated the hydrogen storage capacity of different carbon nanostructures with various specific surface areas ranging from 22 to 2560 m²/g. An almost linear relation between the storage capacity and the specific surface area was obtained at both room temperature and 77 K with the highest storage capacities of 0.5 and 4.5 wt%, respectively. Kadono *et al.*⁶⁰ examined the hydrogen adsorption properties for two types of different carbon nanomaterials under the temperature of 77 K and pressure up to 2 MPa. They found the one with subnanopores, which had a diameter of 0.5 nm, showed a large hydrogen uptake of 2.8 wt%, compared with 0.7 wt% for the sample with a large pore diameter of 3 nm. Moreover, the estimated density of adsorbed hydrogen of pores with a diameter of 0.5 nm

was found to be comparable to those of the density of bulk liquid hydrogen. Strobel *et al.*⁶¹ measured the hydrogen adsorption on different carbon materials with Brunauer-Emmet-Teller (BET) surface areas ranging from 100 up to 3300 m²/g by using a microbalance at 12.5 MPa and 296 K. The maximum adsorption of 1.6 wt% was found for an activated carbon with a specific surface area of 1400 m²/g. Zuttel *et al.*⁶² presented an empirical model for the hydrogen adsorption on carbon nanostructures. The maximum potential amount of hydrogen adsorbed was calculated to be 3.0 mass % for the adsorption of a monolayer hydrogen and proportional to the specific surface area of the carbon sample $2.28 \times 10^{-3} \text{ mass \% S [m}^2 \text{ g}^{-1}\text{]}$. The potential adsorption for SWNTs started at 1.5 mass% and increased with the diameter of the tube. The SWNT with a diameter of 2.2 nm had the potential to adsorb 5 mass% of hydrogen. However, this model suffered from the assumption that the hydrogen condenses in the nanotubes although the critical temperature of hydrogen is 33 K.

1.1.2.3 Hydrogen Storage in Carbon Nanotubes

Carbon nanotubes can be envisaged as a cylindrical hollow tube rolled up from a single layer of graphene with diameter in the nanometer range and length usually on the micron scale. Depending on the number of tube walls, CNTs can be classified into SWNTs and MWNTs. After the pioneering works of Dillon and coworkers,²⁹ attempts were soon made to use these materials for hydrogen storage. Both SWNTs and MWNTs were investigated.

Chen *et al.*⁶³ studied the hydrogen storage of aligned MWNTs synthesized by a plasma-assisted chemical vapor deposition (CVD) method. It was found that a hydrogen storage capacity of 5-7 wt% was obtained at room temperature under the pressure of 10 atm for the as-synthesized sample and the hydrogen storage capacity increased up to 13 wt% for the heat treated sample; however, the release of adsorbed hydrogen was needed to heat up to 300° C. The authors attributed their high value to the open end of the nanotubes and their alignment. Cao *et al.*⁶⁴ compared the hydrogen adsorption behaviors of well-aligned MWNTs and randomly ordered MWNTs at 290 K and 10 MPa. The hydrogen uptake of aligned MWNTs was much higher than that of randomly ordered MWNTs, with the value of 2.4 wt% and 0.5 wt%, respectively. The authors proposed that intertube channels of the well-aligned MWNTs were the effective domains for the hydrogen adsorption. In another work, Wang *et al.*⁶⁵ reported the hydrogen storage in CNTs and CNTs films at ambient temperature and pressure. The CNTs films adsorbed much more H₂ than CNTs powder and a H₂ adsorption capacity of 8 wt% was achieved for the CNTs films. However, the mechanism of this hydrogen uptake was not clear. Hou *et al.*⁶⁶ studied the hydrogen storage capacities for the as-prepared and purified MWNTs. The hydrogen uptake of the purified sample was much higher than that of the as-prepared one. The hydrogen uptake of 6.3 wt % and 31.6 kg/m³ was obtained for the purified sample at room temperature and 14.8 MPa. The authors attributed this to the opened tips, simpler chemical state, and larger micropore volume of the purified MWNT sample. Later, this group⁶⁷ studied hydrogen storage capacity of MWNTs with diameters ranging from 13 to 53 nm, and found that the hydrogen storage capacity of the MWNTs is proportional to their diameters. Shiraishi *et al.*⁶⁸ studied the hydrogen storage properties

for the SWNT bundles and peapods i.e. C₆₀ encapsulated SWNTs. The hydrogen desorption occurred at about 350 K by the TPD method. From the results it can be concluded that the inter-tube sites in SWNT-bundles can be used as a host for hydrogen storage, and the availability of 'sub-nanometer' sized spaces was responsible for the moderate desorption temperature. In a further research,⁶⁹ however, a low value of H₂ uptake of 0.3 wt% was observed at room temperature and 9 MPa on SWNTs. Gundiah *et al.*⁷⁰ investigated the hydrogen storage performance of several kinds of SWNT and MWNT samples obtained by different methods of synthesis or subjected to different pre-treatment procedures. A maximum capacity of 3.7 wt% was obtained for the acid-treated aligned MWNT sample at 300 K and 145 bar, which coincides well with the result obtained by electrochemical measurements. Gao *et al.*⁷¹ made a comparative study of the hydrogen storage properties of high specific surface area activated carbon, open-tipped MWNTs, close-tipped MWNTs and SWNTs both at room temperature and at 77 K. At both temperatures, the open-tipped MWNT sample showed the highest storage capacity, 6.46 wt% at 77K and 1.12 wt% at room temperature. In another work, Jang *et al.*⁷² examined the hydrogen storage capacities of bamboo-shaped MWNTs and compared with those of SWNTs and MWNTs. It was found that the greatest hydrogen adsorption is about 0.4 wt% at atmospheric pressure and temperature for the bamboo-shaped MWNT sample with a herringbonelike structure. The SWNTs showed a comparable hydrogen storage capacity, whereas the MWNTs were insensitive to the pressure change. Anson *et al.*⁷³ studied the hydrogen uptake of SWNTs before and after heat treatment in air by measuring their adsorption isotherms under nearly 1 bar at different temperatures. Hydrogen storage capacities of 0.01 wt% at 298 K and 1 wt% at 77 K were obtained for

the heat treated sample. The isosteric heats of adsorption were calculated to be 7.42 and 7.75 kJ/mol for the raw and pre-treated SWNTs, respectively. Lawrence *et al.*⁷⁴ reported that the hydrogen adsorption in SWNTs seemed to be saturated at 300 atm at room temperature, and a capacity of 0.91 wt% was achieved, which was lower than that of high specific surface area ACs. Taking into account the specific surface area of the SWNTs (800m²/g) and ACs (2800m²/g), adsorption rates of 0.53×10⁻³ wt% /1000 m²/g and 1.14×10⁻³ wt% /1000 m²/g were obtained for the ACs and SWNTs, respectively. The latter value compares well with the previous result.^{52, 62} Chen *et al.*⁷⁵ reported the hydrogen storage properties of KOH modified MWNT. The high hydrogen adsorption value of 4.47 wt% was obtained by temperature desorption spectroscopy (TDS) experiments. The defect structure of CNTs formed via KOH activation was mainly attributed to this high hydrogen sorption capacity. Zacharia *et al.*⁷⁶ investigated the dependency of the gravimetric hydrogen storage capacity of SWNTs and MWNTs with the specific surface area at room temperature. The capacity scales linearly with the specific surface area, irrespective of the type of nanotubes used. A small amount of hydrogen uptake of less than 0.16 wt% was found for all the samples.

1.1.2.4 Hydrogen Storage in Graphite/Carbon Nanofibers

Graphite/carbon nanofibers can be viewed as an arrangement of graphene platelets in a parallel, perpendicular, or angled orientation with respect to the fiber axis. Stimulated by the extraordinary results of Chambers and coworkers,^{38, 39} many research groups

investigated the hydrogen storage properties of GNFs/CNFs. However, none of the groups can repeat the high hydrogen storage value.

Gupta *et al.*⁷⁷ synthesized and investigated the hydrogen adsorption properties of GNFs at room temperature and the pressure of 120 atm. The Pressure-Composition-Temperature isotherm showed hydrogen storage capacity of around 10 wt% for the GNF prepared through ethylene gas. Marella *et al.*⁷⁸ studied the hydrogen storage capacities of CNFs which were grown by catalytic decomposition of ethylene in presence of hydrogen with different catalysts and treatment procedures. A maximum hydrogen storage of 1.38 wt% can be obtained at 77 bar and room temperature. Blackman *et al.*⁷⁹ investigated the hydrogen storage capacities of CNFs produced by different activation methods and found that the increase of the hydrogen adsorption capacities did not correspond directly with the increase of the surface areas. The hydrogen storage capacity of less than 0.4 wt % was obtained for all the samples at 10 MPa and 30°C. Browning *et al.*⁸⁰ studied the hydrogen storage in CNFs and found the hydrogen adsorption capacities can be up to 6.5 wt% at 12 MPa and ambient temperature. This high capacity of hydrogen storage can be explained by the physisorption on the external surface area and the hydrogen dissociation on graphite edge sites, which is a chemisorption process. Hong *et al.*⁸¹ investigated the hydrogen storage properties of GNFs prepared from catalytic graphitization of electrospun poly (vinylidene fluoride) nanofibers. The hydrogen uptake of 0.11-0.18 wt% was observed at room temperature and 80 bar. They suggested that the ultramicropores (< 1 nm) were responsible for this hydrogen adsorption.

1.1.2.5 Hydrogen Storage in Activated Carbon

Activated carbon is a synthetic carbon modification containing of very small graphite crystallites and amorphous carbon. The pore diameters are usually less than 1 nm and form a specific surface area up to 3000 m²/g. The high surface area and small pore size of AC have attracted much research interest in hydrogen storage.

In 1994, Chahine and Bose⁸² investigated the hydrogen storage capacity of AX-21 at 77 K and 1 MPa and hydrogen uptake of 5.3 wt% was obtained. Zhou *et al.*⁸³ compared the hydrogen storage properties of activated carbon AX-21 and MWNT at ambient temperature. The 0.5 and 0.14 wt% were obtained at 298 K and 6 MPa, respectively. In addition, the corresponding hydrogen adsorption enthalpies for these two samples were calculated to be 6.4 and 1.7 kJ/mol. De la Casa-Lillo *et al.*⁸⁴ reported the hydrogen sorption capacities for a large variety of ACs and activated carbon fibers (ACFs). The highest value of hydrogen adsorption was found to be 1 wt% at room temperature and a pressure of 10 MPa. The experimental results reported here correlated well with those of the theoretical studies^{11, 13} and confirmed that the optimum pore size for hydrogen adsorption in porous carbons is about 0.6 nm, which can hold two layers of adsorbed hydrogen. Texier-Mandoki *et al.*⁸⁵ examined the hydrogen storage properties of different ACs with surface areas ranging from 890 to 3000m²/g. They found that the hydrogen storage capacities correlated well with the Dubini-Radushkevitch volume measured by CO₂ adsorption and proposed that the ultramicropores (pores smaller than 0.7 nm) played an essential role in hydrogen uptake process, which agreed with the work by Zhao and coworkers.⁸⁶ A maximum hydrogen adsorption of 4.5 wt% was obtained for a AC

sample, which has a surface area of 3000 m²/g and Dubini-Radushkevitch volume of 0.6 cm³/g at 77 K and 10 bar.

1.1.2.6 Hydrogen Storage in Other Carbon Nanostructures

Other carbon nanostructures such as graphite, carbon aerogel, mesoporous carbon etc. have also been investigated for hydrogen storage.

Kabbour *et al.*⁸⁷ presented the hydrogen sorption properties of activated and metal-doped carbon aerogel (CA). A maximum hydrogen adsorption capacity of 5.3 wt% was found for the CA sample with a surface area of 3200m²/g at 77 K. A linear dependence of H₂ adsorption value with the surface area was also established. The hydrogen enthalpy of adsorption for the metal-doped CA was measured to be about 7 kJ/mol, which is larger than that of AX-21.⁵⁷ Orimo *et al.*⁸⁸ showed that nanostructured graphite can hold up to 7.4 wt% hydrogen if the graphite is prepared by reactive ball milling for 80 h under a 1.0 MPa hydrogen atmosphere. However, hydrogen desorption started at about 600 and 950 K, respectively.⁸⁹ Chen *et al.*⁹⁰ investigated the hydrogen adsorption/desorption behaviors of mechanically milled graphites under different hydrogen pressures ranging from 0.3 to 6 MPa and found chemisorbed hydrogen concentration decreased with the increasing of the hydrogen pressure, however, the physisorbed hydrogen concentration increased with the increase of the hydrogen pressure. The maximum uptake of hydrogen for chemisorption and physisorption was 6.1 and 0.5 wt%, respectively. Pang *et al.*⁹¹ examined the hydrogen adsorption of mesoporous carbon materials with different surface areas ranging from 886 to 2314 m²/g, different pore sizes and pore volumes and found

that the maximum hydrogen adsorption capacity was 1.78 wt% at 77 K and ambient pressure for the sample with the highest surface area. Furthermore, an approximately linear fashion between the hydrogen adsorption capacities and the surface areas of the samples was found. Shao *et al.*⁹² investigated the hydrogen storage behaviour of an activated mesocarbon microbead sample with a BET surface area of 3180 m²/g both in experimental and theoretical methods. Hydrogen adsorption of 0.3 wt% at 298 K and 7.8 wt% at 77 K under the ambient pressure were obtained experimentally. However, at a pressure of 10 MPa, the theoretical prediction showed much higher values, which are 3.2 and 15 wt%, respectively. Gogotsi *et al.*⁹³ reported the hydrogen storage properties of the carbide derived carbon (CDC), which has a specific surface area of up to 2000m²/g and up to 80% open pore volume. A maximum hydrogen adsorption capacity of 3 wt% was obtained at 77 K and 1 bar. It was found that the small pores are responsible for the high sorption ability, which supports the theoretical prediction that the small pores with narrow size distribution are the key to high hydrogen uptake. Yang *et al.*⁹⁴ reported the hydrogen sorption properties of zeolite-like carbon materials with surface area up to 3200 m²/g. A maximum hydrogen adsorption of 6.9 wt% was achieved at 77 K and 20 bar. This capacity was among the highest values ever reported for carbon or any other porous materials such as metal organic frameworks (MOFs) or zeolites. Moreover, the hydrogen enthalpy of this sample was calculated to be 8.2 kJ/mol, which is also among the highest values reported for carbon materials suggesting a strong interaction between adsorbed hydrogen and the carbon surface. This high heat of adsorption and the “optimal pore” of size 0.6-0.8 nm of this material were attributed to the high hydrogen sorption ability. Terres *et al.*⁹⁵ reported the H₂ storage capacities of spherical nanoporous carbons with

surface areas ranging from 946 to 1646 m²/g. The maximum hydrogen uptake of 2.7 wt% was obtained at 77 K for the sample with a periodic array of channels and surface area of 1642 m²/g. The authors emphasized again the importance of surface area to the hydrogen storage capacity in carbonaceous materials.

1.1.2.7 Hydrogen Storage in Carbon Nanostructures by Spillover

Hydrogen spillover is defined as the dissociative chemisorption of hydrogen on the catalyst and the subsequent migration of atomic hydrogen onto the surface of the receptors such as activated carbon. This new technique will open a new direction of finding high performance hydrogen storage materials.

Yang *et al.*⁹⁶⁻¹⁰⁰ investigated the hydrogen storage properties in various carbon nanostructures by hydrogen spillover. The simple mixing of CNTs with supported palladium was found to increase the uptake of the hydrogen by a factor of three.⁹⁸ In another study, Mu *et al.*¹⁰¹ studied the hydrogen storage properties of modified CNTs and compared with those of original samples. It was found that hydrogen uptake improved 3 times for the treated samples, which can be up to 4.5 wt % at room temperature and 10 MPa. It is proposed that the wall defects or disordered structure brought by microwave plasma etching and Pd decoration can contribute to this increased hydrogen storage performance. The mechanism of hydrogen uptake included the dissociation of hydrogen molecules into atoms or protons on the surface of metallic Pd, diffusion into the hollow interiors of tubes, recombined to the hydrogen molecules. Zacharia *et al.*¹⁰² compared the hydrogen sorption capacity of platinum-MWNT with that of pristine one and found

hydrogen storage capacity of the platinum deposited nanotube was nearly 40 times larger than that of pristine sample, which can be up to 2.9 wt% at 298 K and 16 atm. The enhanced hydrogen sorption capacity was attributed to the spillover of physisorbed hydrogen from platinum particles. Lee *et al.*¹⁰³ reported the hydrogen storage properties of ACFs modified by Ni doping and fluorination. The hydrogen uptake increased due to the enhancement of hydrogen affinity by Ni doping and fluorination even though the specific surface areas of modified ACFs decreased after treatment. Thus, they concluded that the hydrogen storage capacity was not determined only by the factor of specific surface areas, it was also related to the micropore volumes, pore size distribution and surface properties of these ACFs.

The above results indicate that the early spectacular hydrogen storage capacities reported for carbon nanostructured materials at near-ambient temperature have not been independently verified by other groups. In fact, repeatable hydrogen adsorption of approximately ~ 5 wt% at 77 K and < 0.5 wt% at room temperature can be achieved under high pressure conditions for the carbon based nanostructured materials. The maximum hydrogen uptake correlates linearly with the specific surface area and pore volume of the adsorbent. This suggests that the best materials for practical storage application will be the one with the largest specific surface per unit volume. Since the physisorption of hydrogen on carbon nanostructures falls short of the DOE targets for the use of hydrogen as a transportation fuel, further efforts of designing materials with high surface areas and pore volumes are needed.

1.1.3 Hydrogen Storage of Metal Organic Frameworks

Recently, a new class of porous metal-organic frameworks (MOFs)¹⁰⁴⁻¹¹⁴ have attracted much attention for hydrogen storage because of their exceptionally high specific surface area and microporosity, uniform but tunable pore size, very low density and well-defined hydrogen occupation sites. Generally speaking, these materials are synthesized in a building block approach from metal or metal oxide vertexes interconnected by organic linkers. They have the potential to exhibit properties inherent to the building blocks, such as geometric rigidity, chemical functionality, or chirality. A variety of linker molecules can be used to create an entire family of materials having different pore sizes and containing different chemical functionalities within the linkers but all with the same basic framework topology. In addition, different metal corners and different linkage chemistries can yield a wide variety of other framework topologies.

Yaghi *et al.*¹¹⁵ first reported the hydrogen adsorption properties of MOF-5 (Zn_4O clusters linked by BDC; BDC=1,4-benzenedicarboxylates) at both 78 K and ambient temperature. Promising hydrogen storage capacities of 4.5 wt% at 78 K and ambient pressure and 1 wt% at room temperature and a pressure of 20 bar were obtained. Moreover, they showed that the amount of adsorbed hydrogen increased with increasing pressure at an almost linear fashion at both 77 and 298 K. The authors claimed that the observed sharp uptake of H_2 at lower pressure indicates favourable sorption interactions between the MOF-5 framework and H_2 and proposed the presence of two well-defined binding sites of hydrogen, which are zinc and the BDC linker, respectively by the measurement of inelastic neutron scattering. One year later, the same group¹¹⁶ examined

the hydrogen storage capacities of a variety of MOFs with surface areas ranging from 1466 to 4526 m²/g. The maximum hydrogen uptake in this research was 1.6 wt% at 77 K and 1 bar for IRMOF-11, which had a surface area of 1911 m²/g. Apparently, there is a lack of correlation between the measured surface area and the hydrogen uptake. Moreover, the isotherms for hydrogen adsorption in different MOF materials did not achieve the plateau therefore no saturation in the surface took place. They also found that the MOF-5 gave a hydrogen uptake of 1.3 wt% not 4.5 wt% in previous study¹¹⁵ at 77 K and 1 bar, which is consistent with the result of Panella and coworkers.¹¹⁷ In a more recent investigation,¹¹⁸ Yaghi and coworkers reported the hydrogen sorption properties for a variety of MOFs with surface areas ranging from 1070 to 5040 m²/g at 77 K and hydrogen pressures up to 90 bar. They found that H₂ saturation uptake took place between 25 and 80 bars for all the samples and more interestingly, the hydrogen saturation uptake in these samples correlated well with the surface area just as for zeolites¹¹⁹ and carbon materials.^{50, 58} The maximum hydrogen uptake was 7.5 wt% for IRMOF-177, which had the highest surface area in this study. The hydrogen adsorption data were also compared on a volumetric basis since this is of particular interest for hydrogen storage in transportation applications. Structures with high surface area and moderate density provided the highest storage density on a volumetric basis of 34 kg/m³. Pan *et al.*¹²⁰ reported the hydrogen sorption properties of a novel microporous metal coordination material (MMOM): [Cu(hfipbb)(H₂hfipbb)_{0.5}] [H₂hfipbb=4, 4'-(hexafluoroisopropylidene)bis(benzoic acid)] and found that adsorption capacity of this sample was close to 1 wt % at 48 atm and room temperature. They attributed this hydrogen sorption behavior to the small pore dimension of this new material. They also

pointed out that an optimal material would have pores that fit the size of the gas molecules well and have the largest possible pore volume. Kesanli *et al.*¹²¹ examined the hydrogen sorption capacities of two novel fourfold interpenetrated MOFs, $Zn_4O(L^1)_3$ and $Zn_4O(L^2)_3$ ($L^1=6,6'$ -dichloro-2,2'-diethoxy-1,1'-binaphthyl-4,4'-dibenzoate, $L^2=6,6'$ -dichloro-2,2'-dibenzoyloxy-1,1'-binaphthyl-4,4'-dibenzoate) and found hydrogen adsorption of 1.12 and 0.98 wt% at room temperature and 48 atm, respectively. The small pore size of less than 5 Å due to the interpenetration can attribute the high hydrogen uptake for these materials. Dybtsev *et al.*¹²² reported the hydrogen sorption behavior for the microporous manganese formate ($Mn(HCO_2)_2 \cdot 1/3$ dioxane) with a BET surface area of only 240 m²/g. The moderate hydrogen uptake of 0.9 wt% was achieved at 77 K and 1 atm. This material showed selective sorption of H₂ and CO₂ over Ar, N₂ and such selective sorption of H₂ in this material was rare for the microporous solids. The authors attributed this property to the small aperture of the channels of this MOF material. In a more recent investigation,¹²³ they studied the hydrogen sorption properties of a highly porous MOF, $Zn_2(bdc)_2(dabco)$ [$bdc=$ benzene-1,4-dicarboxylate, $dabco=1,4$ -diazabicyclo[2.2.2]octane] with a surface area of 1450m²/g at 78 K and 1 atm. The maximum hydrogen uptake of 2.0 wt% was attained at the test condition. Furthermore, a rare guest-dependent dynamic behavior, of which the framework shrinks upon inclusion of organic guest molecules and expands upon guest removal, was revealed in this material. The reason for this is not clear. Lee *et al.*¹²⁴ studied the hydrogen storage capacity of a robust porous metal-organic open framework, $Ni(cyclam)(bpydc)$ [$cyclam=1,4,8,11$ -tetraazacyclotetradecane, $bpydc=2,2'$ -bipyridyl-5,5'-dicarboxylate] with a surface area of 817 m²/g and pore volume of 0.37 cm³/g. It adsorbed H₂ gas up to

1.1 wt% at 77 K and 1 atm. Kubota *et al.*¹²⁵ reported the direct observation of H₂ adsorbed in the nanochannels of MOF, Cu₂(pzdc)₂(pyz) [pzdc=pyrazine-2,3-dicarboxylate, pyz=pyrazine] by in-situ synchrotron powder diffraction. A hydrogen sorption of only 0.2 wt% was obtained at 90 K and 1 atm. Chen *et al.*¹²⁶ reported the hydrogen adsorption behavior of a MOF with open metal sites, Cu₂(bptc) [bptc=biphenyl-3,3',5,5'-tetracarboxylate] at 77 K and 1 atm. The maximum sorption of 2.47 wt% was gained for the fully activated sample. This value represents the highest hydrogen uptake under the pressure of 1 bar. It was proposed that the open metal sites were responsible for this high adsorption capacity. Later, the same group¹²⁷ further investigated the hydrogen storage property for a new microporous dynamic MOF Zn(NDC)(4,4'-Biby)_{0.5}·2.25DMF·0.5H₂O [NDC=2,6-naphthalenedicarboxylate, 4,4'-Biby=4, 4'-trans-bis(4-pyridyl)-ethylene]. This new material showed a maximum adsorption of 2.0 wt% at 40 bar and 77 K. Considering its low surface area and pore volume, which are only 303 m²/g and 0.20 cm³/g, respectively, this hydrogen sorption amount was pretty surprising. The authors attributed this high hydrogen sorption capacity to the full usage of the pores in the MOF at higher pressure. This study also revealed the potential use of dynamic MOF materials for high-pressure hydrogen storage. Lee *et al.*¹²⁸ reported the hydrogen adsorption of two microporous MOFs, [Zn₃(bpdc)₃bpy]·4DMF·H₂O and [Co₃(bpdc)₃bpy]·4DMF·H₂O (bpdc=biphenyldicarboxylate; bpy=4,4'-bipyridine; DMF=N,N-dimethylformamide) at both 87 and 77 K. It was found that the Co structure adsorbed more hydrogen than the Zn structure at both temperatures and all pressure levels. The values were 1.48 and 1.32 wt% at 87 K and 1 atm, 1.98 and 1.74 wt% at 77 K and 1 atm, respectively. This difference was in agreement with the estimated total micropore

volumes obtained from Ar adsorption data, which were 0.38 and 0.33 ml/g for Co and Zn structure, respectively. Chun *et al.*¹²⁹ reported the hydrogen adsorption behavior of a series of isomorphous Zn MOFs with the surface areas ranging from 1450 to 2090 m²/g. The corresponding hydrogen sorption capacities of 1.7-2.1 wt% were obtained at 77 K and 1 atm. By detailed analysis of hydrogen sorption data in these MOFs, they also concluded that smaller pores actually take up hydrogen more effectively than very large ones, which agrees with previously reported result by Chen and coworkers.¹²⁶ In 2004, Zhao *et al.*¹³⁰ reported the hydrogen adsorption properties for Ni based porous MOFs, Ni₂(bipy)₃(NO₃)₄ (bipy = 4,4'-bipyridyl) and Ni₃(btc)₂(3-pic)₆(pd)₃ (btc = 1,3,5-benzene tricarboxylate, pic = 3-picoline, and pd = 1,2-propanediol). The maximum hydrogen sorption capacity of 2.1 wt% was achieved at 77 K and 1 atm. In the case of hydrogen adsorption on Ni₂(bipy)₃(NO₃)₄, a remarkable hysteresis of hydrogen desorption was observed due to the dynamic structure of the material. Hysteresis decreasing at higher temperature was explained by kinetic trapping of the hydrogen. This kinetic trapping effect is related to the flexibility of the porous framework materials. Kaye *et al.*¹³¹ reported the hydrogen adsorption properties for dehydrated Prussian blue analogues M₃[Co(CN)₆]₂ (M=Mn, Fe, Co, Ni, Cu, Zn). The hydrogen sorption capacities of 1.4 to 1.8 wt% were obtained at 77 K and 1 atm. The hydrogen binding enthalpies for this series of cyano-bridged frameworks were 5.9-7.4 kJ /mol, higher than that of MOF-5¹¹⁶ and AX-21.⁵⁷ These materials were expected to store hydrogen at higher temperatures and lower pressures. In the same time, Chapman *et al.*¹³² also examined the hydrogen sorption behaviours for a series of Prussian blue analogues M₃[Co(CN)₆]₂ (M=Mn, Fe, Co, Ni, Cu, Zn, Cd). The maximum hydrogen sorption of 1.2 wt% was achieved at 77 K and 1

atm, compared well with the results of Kaye and coworkers.¹³¹ The hydrogen sorption capacities were found to rely on the different coordinatively unsaturated divalent metal cations contained in the materials. Later on, Long's group¹³³ reported the hydrogen sorption properties of a Mg-based MOF, which had very small pores of about 3.5 Å in diameter. The hydrogen uptake ability for this sample was only 0.6 wt% at 77 K; however, the heat of adsorption was up to 9.5 kJ/mol, which is higher than that of previously reported Zn-based MOFs.¹¹⁶ This higher binding affinity can be attributed to the increased van der Waals contact, which are associated with the very small pore size. Most recently, they¹³⁴ reported the hydrogen storage properties of the dehydrated Prussian blue type solids $\text{Ga}[\text{Co}(\text{CN})_6]_2$, $\text{Fe}_4[\text{Fe}(\text{CN})_6]_3$, $\text{M}_2[\text{Fe}(\text{CN})_6]$ (M=Mn, Co, Ni, Cu) and $\text{Co}_3[\text{Co}(\text{CN})_5]_2$ and compared with those of $\text{M}_3[\text{Co}(\text{CN})_6]_2$ (M=Mn, Fe, Co, Ni, Cu, Zn). The maximum saturation hydrogen uptake of 2.3 wt% was predicted at 77 K for $\text{Cu}_2[\text{Fe}(\text{CN})_6]$. The hydrogen enthalpies for these samples were calculated to be 6-7 kJ/mol, which is consistent with the previous results for dehydrated Prussian blue analogues.¹³¹ Based on the fact that the hydrogen enthalpies was not substantially higher for the framework containing coordinatively-unsaturated metal centres, they drew a conclusion that the exposed metal coordination sites in these materials do not dominate the hydrogen binding interaction. In another work, however, Yang *et al.*¹³⁵ performed a systematic molecular simulation study on the adsorption and diffusion of hydrogen in MOFs. It was found that the metal-oxygen clusters are preferential adsorption sites for hydrogen in MOFs and the effect of organic linkers becomes evident with increasing pressure, which is consistent with preciously reported results.^{115, 125} It was also pointed out that IRMOFs are promising hydrogen storage materials at 77 K, but the hydrogen

storage capacity at room temperature and moderate pressure are still short of expectations. Later, this same group¹³⁶ explored a further theoretical investigation of the hydrogen adsorption in MOF-505, a MOF with open metal sites, by a combined GCMC simulation and DFT calculation. The metal-oxygen clusters are preferential adsorption sites for hydrogen, and the strongest adsorption of the hydrogen is found in the directions of coordinately unsaturated open metal sites, providing evidence that the open metal sites have a favorable impact on the hydrogen sorption capacity of MOFs. However, the storage capacity of MOF-505 at room temperature and moderate pressure was predicted to be low. Krawiec *et al.*¹³⁷ reported the hydrogen storage capacity for $\text{Cu}_3(\text{BTC})_2$ (BTC=1,3,5-benzene tricarboxylate). The maximum hydrogen uptake of 2.18 wt% was achieved at 77 K and 1 atm. This value is higher than the results by Lee and coworkers,¹³⁸ which showed a hydrogen storage capacity of 1.44 wt% at 77 K and 1 atm. The authors ascribed this improvement to the higher pore volume of the framework by employing the novel synthesis procedure. The hydrogen binding enthalpy was calculated to be 6.1 kJ/mol, which compares well with values determined by Kaye and coworkers¹³¹ for dehydrated Prussian blue analogues materials. Also, Panella *et al.*¹³⁹ studied the hydrogen adsorption in two different MOFs, MOF-5 and Cu-BTC at temperatures ranging from 77 K to room temperature. The heat of adsorption of 3.8 and 4.5 kJ/mol were obtained for MOF-5 and Cu-BTC, respectively. At room temperature both samples showed hydrogen storage capacities less than 0.4 wt% and at 77 K the saturation hydrogen uptake was 3.6 wt% for Cu-BTC and 5.1 wt% for MOF-5, which is in good agreement with Yaghi's result.¹¹⁸ The nearly linear relation between the maximum hydrogen uptake and surface area was found. They claimed that the low-pressure region of the adsorption isotherm is

strongly dependent on the strength of the interaction between hydrogen molecules and the adsorbent; therefore the difference in the storage capacity at low pressures for different materials is attributed to the difference in heats of adsorption. However, the saturation value is independent of the different heat of adsorption values and can be correlated to the specific surface area of the adsorbing materials. Moreover, Peterson *et al.*¹⁴⁰ investigated the hydrogen sorption properties of $\text{Cu}_3(\text{BTC})_2$. This material adsorbed up to 2 wt% at 77 K and 100 Pa, with saturation of over 3 wt% achieved at 9×10^6 Pa, which is consistent with the above result of Panella and coworkers.¹³⁹ By neutron powder diffraction experiments they found six distinct D_2 adsorption sites in the framework, with coordinatively unsaturated open sites at Cu^{2+} atoms occupied first, followed by nonmetal sites in smaller pores and then in larger pores. This location of the primary site at the coordinatively unsaturated Cu atoms provides direct structural evidence of the potential importance of such metal sites to hydrogen storage. Since 2003, Ferey and coworkers have reported the hydrogen sorption properties of several “MIL” series of MOFs.¹⁴¹⁻¹⁴⁴ In 2003, they first reported the hydrogen adsorption capacities for two nanoporous MIL-53, $\text{Al}(\text{OH})(\text{BDC})$ and $\text{Cr}(\text{OH})(\text{BDC})$ at 77 K.¹⁴¹ The chromium compound showed a maximum adsorption of 3.1 wt% under 16 bar, whereas the aluminum one exhibited 3.8 wt% at the same pressure. However, the obvious hysteresis in the adsorption and desorption was found, and adsorption capacities of 1.8 and 2.2 wt % were recoverable from the Cr- and the Al-based samples, respectively, by desorption down to 0.1 atm. The mechanism of this phenomenon was not clear. In a further report¹⁴² they synthesized a MOF MIL-101 with stoichiometry $\text{Cr}_3\text{F}(\text{H}_2\text{O})_2\text{O}[(\text{O}_2\text{C})\text{C}_6\text{H}_4(\text{CO}_2)]_3 \cdot n\text{H}_2\text{O}$. This material had a zeotype cubic structure with a very large cell volume ($\sim 702,000 \text{ \AA}^3$), and hierarchy

of very large pore sizes (approximately 30–34 Å) with a nitrogen pore volume of 2.0 cm³/g and Langmuir surface area of ~5900 m²/g. Hydrogen adsorption studies showed that the material adsorbed 4.5 wt% at 77 K and 3 MPa. Later on, hydrogen storage properties for two chromium carboxylates MIL-100 and MIL-101 were comprehensively investigated.¹⁴³ The maximum hydrogen adsorption capacity of 6.1 wt% was obtained for the MIL-101 with a surface area around 5500 m²/g at 77 K and 40 atm. The hydrogen enthalpy of this sample was calculated to be 10 kJ/mol. The authors suggested that the small pore size and large micropore volume, combined with the coordinately unsaturated Cr metal centers were attributed to this high hydrogen uptake behavior. More recently¹⁴⁴ they synthesized and investigated the hydrogen storage properties for a new three-dimensional chromium (III) naphthalene tetracarboxylate, Cr₃O(H₂O)₂F{C₁₀H₄(CO₂)₄}_{1.5}·6H₂O (MIL-102). This new porous chromium carboxylate material exhibited a hydrogen storage capacity of 1.0 wt % at 77 K and 35 bar. The small surface area, which is only 42 m²/g, coherent with the small free diameter of tunnels was attributed to this low hydrogen sorption value. In 2006, Sun *et al.*¹⁴⁵ prepared and examined the hydrogen sorption capacity of a novel MOF Cu₃(TATB)₂(H₂O)₃ (TATB=4,4'4''-s-triazine-2,4,6-triyltribenzoate) with a surface area of 3800 m²/g. The hydrogen uptake of 1.9 wt% was obtained at 77 K and 1 bar. The authors ascribed this hydrogen uptake to the specific design factors of this material, that is, the presence of accessible unsaturated metal centers and the existence of pores and channels in a size range well-suited to the H₂ molecule. Later, the same group¹⁴⁶ reported the hydrogen sorption properties of a MOF with entatic metal center PCN-9. This material exhibited a 1.53 wt% hydrogen uptake at 77 K and 1 atm. The heat of adsorption of 10.1 kJ/mol was calculated. This strong

affinity was attributed to the existence of entatic metal center in this sample. Dinca *et al.*¹⁴⁷ reported hydrogen storage properties for a series of microporous MOFs constructed by the 1, 4-benzeneditetrazolate ligand. It was found that the maximum adsorption capacity of 1.46 wt% was achieved at 77 K and 1 atm for $Zn_3(BDT)_3$ [BDT²⁻=1,4-benzeneditetrazolate] with a surface area of 640 m²/g, which is highest in this study. Furthermore, the enthalpies of adsorption in the range 6.0-8.8 kJ/mol were calculated for these materials, which are higher than previously reported results for MOF-5¹¹⁶ and dehydrated Prussian Blue analogues.¹³¹ More recently, the same group¹⁴⁸ reported hydrogen storage capacity of microporous MOFs with exposed Mn²⁺ coordination sites. The total hydrogen storage capacity of 6.9 wt% was obtained at 77 K and 90 bar, together with the volumetric storage capacity of 60 kg/m³. In addition, a maximum enthalpy of adsorption of 10.1 kJ/mol was achieved, which is among the highest yet observed for MOF materials. The H₂ binding at coordinately unsaturated Mn²⁺ centers was attributed to the high hydrogen storage capacity and enthalpy. This ability of H₂ to bind to metal atoms allows the H₂ molecules to pack more closely together and is expected to provide a major boost in storage capacity over simple H₂ adsorption at nonmetal sites in previously prepared materials. Foster *et al.*¹⁴⁹ studied hydrogen adsorption on nanoporous nickel (II) phosphates VSB-1 and VSB-5. It was found that VSB-5 adsorbed substantially more hydrogen at low pressure. TPD studies showed that hydrogen had a strong interaction with VSB-5 with the main desorption peak at 109 K and a small shoulder at 149 K. The strong interaction was confirmed by inelastic neutron scattering studies. Whereas, VSB-1 did not show a similar interaction. It was proposed that coordinatively unsaturated Ni²⁺ sites accessible to H₂ molecules existed in VSB-5 gave this unique surface chemistry. Later

on, they¹⁵⁰ prepared a nickel sulfoisophthalate MOF $\text{NaNi}_3(\text{OH})(\text{SIP})_2$ [SIP=5-sulfoisophthalate], of which the hydrogen sorption properties were investigated at 77 K. The hydrogen uptake of this material was 0.94 wt%. The strongest hydrogen binding site was found to be the coordinately unsaturated metal sites by neutron scattering spectroscopy. A high hydrogen enthalpy of 9.4-10.4 kJ/mol was estimated by a variant of the Clausius-Clapeyron equation. These results underscored again the potential importance of such metal sites to hydrogen storage. Dailly *et al.*¹⁵¹ investigated the hydrogen sorption capacity of IRMOF-1 and IRMOF-8 at 77 K and high pressure. These two samples show saturation adsorption capacity of 4.3 wt% and 3.6 wt%, respectively and the hydrogen sorption enthalpies for these two samples were calculated to be 6.1 and 4.1 kJ/mol. These values are consistent with previous results.^{131, 139} Lin *et al.*¹⁵² synthesized and investigated the hydrogen storage properties for three copper co-ordination framework materials based on biphenyl, terphenyl and quaterphenyl tetracarboxylic acids with formulas, $[\text{Cu}_2((\text{OOC})_2\text{C}_6\text{H}_3\cdot\text{C}_6\text{H}_3(\text{COO})_2(\text{H}_2\text{O})_2)]$, $[\text{Cu}_2((\text{OOC})_2\text{C}_6\text{H}_3\cdot\text{C}_6\text{H}_4\cdot\text{C}_6\text{H}_3(\text{COO})_2(\text{H}_2\text{O})_2)]$ and $[\text{Cu}_2((\text{OOC})_2\text{C}_6\text{H}_3\cdot\text{C}_6\text{H}_4\cdot\text{C}_6\text{H}_4\text{C}_6\text{H}_3(\text{COO})_2)(\text{H}_2\text{O})_2]$. They found that H_2 adsorption is controlled by the available pore volume, with a proportional decrease in adsorbate density with increasing pore size. The maximum gravimetric uptake of 7 wt% was obtained for $[\text{Cu}_2((\text{OOC})_2\text{C}_6\text{H}_3\cdot\text{C}_6\text{H}_4\cdot\text{C}_6\text{H}_4\text{C}_6\text{H}_3(\text{COO})_2)(\text{H}_2\text{O})_2]$ with a surface area of 2932 m^2/g due to its maximum pore volume of 1.284 cm^3/g in this study. The maximum volumetric capacity of 43.6 kg/m^3 was achieved for $[\text{Cu}_2((\text{OOC})_2\text{C}_6\text{H}_3\cdot\text{C}_6\text{H}_4\cdot\text{C}_6\text{H}_3(\text{COO})_2)(\text{H}_2\text{O})_2]$ with a surface area of 2247 m^2/g because of a combination of substantial H_2 uptake and the moderate density. Jhung *et al.*¹⁵³ investigated the hydrogen storage properties for several nanoporous aluminophosphates (AlPOs) to analyze the effect of pore diameter on

hydrogen adsorption characteristics. They found that the heat of adsorption and adsorption capacity per unit micropore volume increased with decreasing pore size. They suggested that the idealized porous material for efficient hydrogen storage is one with narrow pores and large micropore volume, or large surface area. Dietzel *et al.*¹⁵⁴ synthesized, characterized and investigated the hydrogen storage property of a novel three-dimensional coordination polymer Ni(dhtp)(H₂O)₂·8H₂O [dhtp=dihydroxyterephthalate]. This novel sample contained the channels with a diameter of ~11 Å and possessed a Langmuir surface area of 1083 m²/g and a pore volume of 0.41 cm³/g. The maximum hydrogen adsorption for this sample was 1.8 wt% at 77 K. The adsorbed hydrogen per Langmuir specific surface area corresponds to a value of 1.7×10⁻³ wt% m⁻²g, which is similar to the value reported recently for the MOF Cu-BTC.¹³⁹ The unsaturated metal sites within the coordination polymer can be attributed to this adsorption capacity. Frost *et al.*¹⁵⁵ performed the GCMC simulations in a series of ten IRMOFs to predict the hydrogen adsorption isotherms. The results revealed the existence of three adsorption regimes: at low pressure (loading), hydrogen uptake correlates with the heat of adsorption; at intermediate pressure, uptake correlates with surface area; and at the highest pressure, uptake correlates with the free volume. The simulations also revealed that the 2015 DOE volumetric target of 81 Kg/m³ may be difficult to meet using MOF materials, although there are a few materials that are either close or even exceed the 2010 target of 45 Kg/m³.^{118, 147, 152} Besides the above physisorption hydrogen on the MOFs, hydrogen storage by spillover has been proposed as a mechanism to enhance the hydrogen storage density of MOF nanostructures. Yang *et al.*¹⁵⁶ studied the hydrogen storage properties of physical mixture of a catalyst containing 5 wt% Pt supported in

active carbon and IRMOF-1 or IRMOF-8 by employing the secondary hydrogen spillover technique. It was found that the spillover enhancement factors for IRMOF-1 and IRMOF-8 were 3.3 and 3.1, respectively and the highest measured reversible H₂ uptake was 1.8 wt % at 298 K and 10 MPa on a Pt/AC and IRMOF-8 physical mixture. In a further investigation¹⁵⁷ they reported the hydrogen storage capacities of IRMOF-1 and IRMOF-8 by hydrogen spillover with carbon bridges. This bridge-building technique was effective for hydrogen uptake in MOF materials. The maximum hydrogen sorption capacity of 4 wt% was obtained for the bridged IRMOF-8 at 298 K and 10 MPa, which was enhanced by a factor of 8 compared with the pure MOF materials.

From above results, MOFs are very promising materials for H₂ storage at cryogenic temperature and moderate pressure (<100 bar). The building-block approach offers the capability of preparing frameworks with new topologies and fine-tuning both local and extended framework structure. A maximum adsorption of ~7.5 wt% of hydrogen has been observed for MOFs materials because of their high specific surface areas and small pore sizes. However, due to its relatively low density, the volumetric storage density of MOF is usually very low. To achieve the DOE 2015 goal, new strategies of design MOF nanostructures having high surface areas with pores of appropriate dimension, open metal sites, large free volumes, suitable crystal density and large heats of adsorption are required.

1.1.4 Hydrogen Storage of Zeolites

Besides the carbon nanostructures and MOFs, the well-known microporous zeolites were also believed to be promising candidates for the hydrogen storage. They are of interest because of the controllable diameter of the cages and channels, high stability and low cost. One attractive feature of these microporous materials is their containing isolated and exposed cations, which could be acted as the hydrogen binding sites.

Weitkamp *et al.*¹⁵⁸ reported the hydrogen storage properties for a series of zeolites with different pore structures and compositions at temperatures from 293 to 573 K and pressures from 2.5 to 10 MPa. The maximum adsorption capacity of 0.082 wt% was obtained for the zeolite with the highest concentration of sodalites cages at 573 K and 10 MPa. The authors implied that storage capacity was higher for the zeolites having a high number of small cavities in the structures. At cryogenic temperature, hydrogen uptake values have been reported to be much higher. Kazansky *et al.*¹⁵⁹ investigated the hydrogen sorption properties on sodium forms of faujasite at 77 K and found a hydrogen adsorption capacity of 1.2 wt% at 77 K and 60 KPa. Takagi *et al.*¹⁶⁰ measured hydrogen sorption properties of two zeolites: H-YZ and H-ZSM-5 together with several carboneous materials at 77 and 303 K over the hydrogen pressure up to 3.5 MPa. The maximum hydrogen uptake of 0.6 wt% was obtained by the H-YZ with a surface area of 710 m²/g at 77 K and 1 atm. It was also found that the amount of adsorbed hydrogen by weight depended on the micropore volume of the sample. Furthermore, Langmi *et al.*¹¹⁹ reported the hydrogen storage behaviors for zeolites A, X, Y, and RHO at temperatures ranging from 77 to 593 K and pressures up to 15 bar. A maximum hydrogen adsorption capacity

of 1.81 wt% was achieved for the zeolite NaY at 77 K and 15 bar. The authors proposed that the hydrogen storage capacity correlates with the BET surface areas of zeolites in a near linear fashion. Later on, the same group¹⁶¹ investigated the hydrogen storage properties of zeolites X, Y, A and Rho containing exchangeable cations. The maximum hydrogen sorption capacity of 2.19 wt% was reported for the CaX at 77 K and 1 atm. The authors claimed that the available void space of the frameworks was the major factor influencing the hydrogen uptake and suggested that the cations may act as the binding sites for the hydrogen molecules. In another work, Vitillo *et al.*¹⁶² conducted the theoretical studies for a total of 12 zeotypes by classic atomic simulations. The maximal amount of hydrogen sorption capacities, ranging between 2.86-2.65 mass % were found. The predicted maximal storage capacities correlate well with experimental results obtained at low temperature. The same group¹⁶³ further studied the hydrogen adsorption for a series of Chabazite zeolite frameworks, H-SSZ-13, H-ZMS-5 and H-SAPO-34. The maximum hydrogen sorption capacity of 1.28 wt% was found in H-SSZ-13 at 77 K and 0.92 bar. The adsorption energy of 10 kJ/mol was obtained for this framework, which was higher than that of activated carbon⁵⁷ and MOFs.^{131, 137} The authors suggested that the balance between hydrogen accessible space, high contact surface, and strong interaction with polarizing centers is important for hydrogen storage in this class of frameworks and this viewpoint was further proved by another investigation.¹⁶⁴ In 2005, Areat *et al.*¹⁶⁵ studied the thermodynamic properties on hydrogen adsorption on the zeolites Na-ZSM-5 and K-ZMS-5 by means of variable-temperature infrared spectroscopy. It was found that the adsorption enthalpies are 10 kJ/mol for H₂/Na-ZSM-5 and 9.1 kJ/mol for H₂/K-ZSM-5 system, which was consistent with the results of

Zecchina and co-workers.¹⁶³ Recently, Li *et al.*¹⁶⁶ investigated the hydrogen sorption properties of low silica type X zeolite LSX, which is fully exchanged by alkali-metal cations (Li^+ , Na^+ , and K^+). The hydrogen adsorption capacity of LSX zeolite depended strongly on the cationic radius and the density of the cations that are located on the exposed sites. The maximum hydrogen sorption capacity of 1.5 and 0.6 wt% were obtained by a Li-LSX sample at 77 and 298 K respectively. The hydrogen capacity in LSX zeolite by bridged hydrogen spillover was also investigated and the hydrogen storage capacity was enhanced to 1.6 wt % (by a factor of 2.6) at 298 K and 10 MPa. This represents the highest value for zeolite materials at room temperature, although it is not as large as that of the AX-21⁹⁶ and MOFs^{156, 157} reported previously.

The factor limiting the storage capacity of such system is the relative large mass of zeolite frameworks, which contained Si, Al, O and heavy cations. Furthermore, many materials seem to have unnecessary large diameters of their voids.

1.1.5 Hydrogen Storage of Clathrates

Trapping or encapsulation of hydrogen into the microporous media was another strategy for the hydrogen storage. The idea is to force hydrogen into the cavities of the nanostructured host. Upon cooling, hydrogen is trapped inside the cavities. It can be released again by raising the temperature. Thus, trapping may be a solution to overcoming the low binding energies of the physisorption process. The clathrate hydrogen hydrates were recently reported as the potential hydrogen storage media by capturing the hydrogen into the H_2O cages.¹⁶⁷ Clathrate hydrates are crystalline inclusion

compounds composed of a hydrogen-bonded water host lattice and guest molecules. There are three common types of gas hydrates structures: sI hydrate, which consists of two 5^{12} cages and six $5^{12}6^2$ cages in a unit cell; sII hydrate, which consists of sixteen 5^{12} cages and eight $5^{12}6^4$ cages in a unit cell; sH hydrate, which consists of three 5^{12} , two $4^35^66^3$, and one $5^{12}6^8$ cages in a unit cell. The type of crystalline structure depends on the size of the guest molecule. Small gas usually generated sI and sII hydrates and larger guest molecule resulted in the sH hydrate.¹⁶⁷

Mao *et al.*¹⁶⁸ reported a new type sII clathrate hydrate with a molar ratio of H_2 to H_2O of approximately 1:2. This mixture was crystallized at a pressure of 220 MPa and 250 K. The clathrate cages formed were multiply occupied, with a cluster of two H_2 molecules in the small cages and four in the large cages, which means that the hydrogen hydrate can reversibly store up to 5.3 wt% hydrogen.¹⁶⁹ The quenched clathrate is stable up to 145 K at ambient pressure. Raman spectroscopy study showed the hydrogen molecules in the clathrate cages were still in free rotational states. However, a substantial softening and splitting of the vibron peaks of hydrogen indicated increased intermolecular interaction between hydrogen and water molecules in the cage.¹⁶⁸ In another work, Patchkovskii *et al.*¹⁷⁰ performed a theoretical study on the thermodynamic stability of the type sII hydrogen hydrate by employing a statistical mechanical model in conjunction with first-principle quantum chemistry calculations. The theoretical analysis confirmed the experimental results and suggested that the stability of the clathrate was mainly caused by dispersive interactions between H_2 molecules and the water forming the cage walls. According to the calculation, it was found that the clathrate is thermodynamically stable at 2.5 MPa and 150 K. The main limitation of the hydrogen clathrate was that the

hydrogen cluster can only be stabilized in the cages at extremely high pressure. To store H₂ at low pressure, Florusse *et al.*¹⁷¹ showed that the presence of tetrahydrofuran (THF) as a guest component may indeed stabilize the clathrate at 280 K and 5 MPa. The powder X-ray diffraction (PXRD) measurements also conformed that the same sII binary clathrate hydrate has formed as that reported by Mao and co-workers.¹⁶⁸ Raman spectroscopy measurements suggested that all or most of the large cages of the binary clathrate hydrate are filled with THF. In contrast, the H₂ molecules most likely occupy to a large extent only the small cages. Although the inclusion of THF molecules can considerably decrease the synthetic pressure, their presence also leads to a significant decrease in the capacity of hydrogen storage. To solve this problem, Lee *et al.*¹⁷² reported that hydrogen storage capacities in THF-containing binary-clathrate hydrates can be increased up to 4 wt% at modest pressures by tuning their composition to allow the hydrogen guests to enter both the larger and the smaller cages, while retaining the low-pressure stability. The authors carried out a number of experiments at a H₂ pressure of 12 MPa and temperature of 277.3 K and found when the THF concentration was in the range of 2.0 to 5.56 mol%, H₂ and THF molecules occupied the smaller and larger cages, respectively, leading to a storage capacity of 2.09 wt% H₂. However, a maximum storage capacity of about 4 wt% H₂ can be obtained when the concentration of THF was decreased to 0.15 mol%. In this case, H₂ occupied not only all the small cages but also some of the larger ones. Further lowering the concentration of THF resulted in a failed formation of hydrogen hydrate under the condition used (12 MPa H₂ and 277.3 K). Furthermore, Strobel *et al.*¹⁷³ reported the hydrogen sorption properties of the binary THF-H₂ clathrate hydrate. The maximum hydrogen storage capacity of this binary sII

hydrate was found to be around 1 wt% at moderate pressure (< 60 MPa). This result corresponds to the storage capacity for the stoichiometric binary hydrate with one hydrogen molecule per small cavity. Contrary to previous reports,¹⁷² hydrogen storage was not increased upon decreasing the THF concentration below the stoichiometric 5.6 mol % solution to 0.5 mol %, at constant pressure. These findings indicate that THF remains the favorable guest for the large cage, and that multiple hydrogen occupancies in this system cannot be achieved at moderate pressures. More recently, Chapoy *et al.*¹⁷⁴ have investigated the hydrogen storage in semi-clathrate hydrates of quaternary ammonium compounds. The formed binary H₂-TBAB (TBAB=(C₄H₉)₄N⁺Br⁻) and H₂-TBAF (TBAF=(C₄H₉)₄N⁺F⁻) semi hydrates are stable at ambient temperature and pressure. In addition of this favorable stability, the hydrogen adsorption capacities of these hydrates are an order of magnitude greater than that of previously reported binary H₂-THF clathrates¹⁷³ at the same pressure.

Obviously, this system is strongly sensitive to promoters, so it has room for further development by optimization of the promoter system. Whereas, the slow kinetic of current synthetic approach of the hydrogen clathrate also creates the difficulties of the practical application. Thus, further investigation is needed to achieve the hydrogen clathrate system with high storage capacity and fast kinetics properties.

1.2 Chemisorption of Hydrogen

Chemisorption is a type of adsorption whereby a molecule adheres to a surface through the formation of a chemical bond. This process is characterized by high

temperatures, strong interaction and high enthalpies. Chemisorption materials may provide high volumetric and gravimetric storage capacities. However, due to the strong interaction between the adsorbate and surface, the reversibility can only be observed at high temperature.

1.2.1 Hydrogen Storage of Metal Hydrides

Metal hydrides form a wide range of stoichiometric and non-stoichiometric compounds by direct interaction of hydrogen with metals. Metal hydrides containing only one metal have limited practical applications in hydrogen storage because of their high thermodynamic stabilities. For this reason, the metallic hydrides of intermetallic compounds have been investigated over the past several decades in order to find a material that meets the practical requirements. Some of the metallic hydrides of interest for the hydrogen storage purpose are listed in Table 1.¹⁷⁵ The prototype intermetallic hydrides are composed of two elements. The A element is usually a rare earth or an alkaline earth metal and tends to form a stable hydride. The B element is often a transition metal and forms only unstable hydrides, such as Pt and Ru, which can absorb considerable quantities of hydrogen, together with Pd and Ni, which are excellent hydrogenation catalysts although they do not form hydrides.²

Table 1. The most important families of hydride-forming intermetallic compounds.

Intermetallic compound	Prototype	Hydrides	Structure
AB ₅	LaNi ₅	LaNi ₅ H ₆	Haucke phases, hexagonal
AB ₂	ZrV ₂ , ZrMn ₂ , TiMn ₂	ZrV ₂ H _{5.5}	Laves phase, hexagonal or cubic
AB ₃	CeNi ₃ , YFe ₃	CeNi ₄ H ₄	Hexagonal, PuNi ₃ -type
A ₂ B ₇	Y ₂ Ni ₇ , Th ₂ Fe ₇	Y ₂ Ni ₇ H ₃	Hexagonal, Ce ₂ Ni ₇ -type
A ₆ B ₂₃	Y ₆ Fe ₂₃	Ho ₆ Fe ₂₃ H ₁₂	Cubic, Th ₆ Mn ₂₃ -type
AB	TiFe	TiFeH ₂	Cubic, CsCl- or Ti ₂ Ni-type
A ₂ B	Mg ₂ Ni, Ti ₂ Ni	Mg ₂ NiH ₄	Cubic, MoSi ₂ - or Ti ₂ Ni-type

The formation of metal hydrides is an exothermic reaction. Significant heat is released during absorbing hydrogen and the same heat has to be provided to the metal hydride to desorb the hydrogen (endothermic reaction). If the hydrogen desorbs below RT, this heat can be delivered by the environment. However, if the desorption is carried out above RT, the necessary heat has to be delivered from an external source, such as the combustion of hydrogen.² One of the most interesting features of metallic hydrides is their extremely high volumetric density. A volumetric density of 115 kg/m³ was reached in LaNi₅H₆.¹⁷⁵ However, all the reversible hydrides working around ambient temperature and pressure consist of the heavy transition metals; therefore, the gravimetric density of hydrogen is limited to less than 3 wt%. For example, the gravimetric density of hydrogen in LaNi₅H₆ is only 1.5 wt%. Light metal hydrides such as Mg and Ca appear to be promising candidates for hydrogen storage. In fact, MgH₂ which containing 7.6 mass% hydrogen have already been reported. But its formation from bulk Mg and gaseous hydrogen is extremely slow. To increase the sorption kinetics, the nanocrystalline Mg hydrides can be prepared by mechanochemical process such as high-energy ball-milling.^{176, 177} Once ball-milled, the adsorption and desorption kinetics can be enhanced.¹⁷⁸ To further improve the

H exchange kinetics, composite materials were prepared by ball milling of Mg with a series of transition metals e.g. V^{179,180}, Nb¹⁸¹, Pd, Pt, Ni,^{182,183} Ru,¹⁸⁴ Fe, Cu, Co.¹⁸⁵

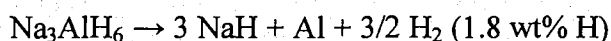
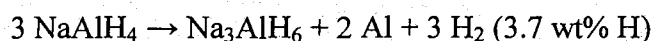
The main disadvantages of metal hydrides are their low gravimetric densities, high desorption temperature and slow hydriding and dehydriding rates. The new catalysts and proper preparation methods are needed to overcome these problems and obtain practical materials.

1.2.2 Hydrogen Storage of Complex Hydrides

Group I, II, and III elements, e.g. Li, Mg, B, Al, build a large variety of metal-hydrogen complexes. All hydrides with hydrogen to metal ratio of more than two are ionic or covalent compounds and belong to this complex hydride group. The main difference between complex and metallic hydrides is the transition to an ionic or covalent compound upon hydrogen absorption. The hydrogen in the complex hydrides is often located in the corners of a tetrahedron with B or Al in the center. The negative charge of the anion, $[\text{BH}_4]^-$ and $[\text{AlH}_4]^-$, is compensated for by a cation, e.g. Li or Na. The hydride complexes of boron, the tetrahydroborates $\text{M}(\text{BH}_4)$, and of the aluminum, the tetrahydroaluminates $\text{M}(\text{AlH}_4)$ are interesting hydrogen storage materials. They are known to be stable and decompose only at elevated temperatures, often above the melting point of the complex.¹⁷⁵ However, the decomposition temperature can be reduced and the hydrogen adsorption efficiency improved by using various dopants or reducing the grain size. Aluminum and boron hydrides of light alkali metals show the highest volumetric density, 150 kg/m^3 , in $\text{Al}(\text{BH}_4)_3$, and the highest gravimetric density at room temperature

known today in LiBH₄ (18 wt%). Of these materials, NaAlH₄ can reversibly absorb/desorb hydrogen at moderate temperatures, which received more attention recently.

Bogdanovic *et al.*¹⁸⁶ showed, for the first time, the reversible hydrogen storage system of NaAlH₄ doping with small amount of Ti compound. A maximum hydrogen storage capacity of 4.2 wt% was obtained at 210°C. In a further study,¹⁸⁷ they found that through variation of NaAlH₄ particle sizes, catalysts (dopants) and doping procedures, kinetics as well as the de- and rehydrogenation stabilities within different cycles can be substantially improved. Thermal decomposition of NaAlH₄ at higher temperatures took place in two steps to give NaH, Al and H₂. In principle the first step can give 3.7 wt% H₂ and up to 5.5 wt% can be achieved for the total two steps:



The enthalpies of the dissociation reactions were determined to be 37 and 47 kJ/mol for the first and second dissociation steps of Ti-doped NaAlH₄, respectively. These enthalpies can be translated to equilibrium pressure of about 1 bar for the first step at 30°C and 1 bar for the second step at about 100°C. More recently, Bogdanovic *et al.*¹⁸⁸ reported the hydrogen storage properties of Na alanate doped with titanium nanoparticles and found when using TiN as a doping agent, the 4.9-5.1 wt % close to the theoretical limit of 5.5 wt% were obtained at 104 or 170 °C in the pressure range of 140-115 bar. In the case of Ti colloidal doped NaAlH₄, hydrogenation times of 10-15 mins approaching those required for practical applications combined with high capacities 4.5 wt% have been realized in cycle tests. In another study, Zidan *et al.*¹⁸⁹ found that the dehydrating

kinetics of NaAlH₄ are significantly enhanced through zirconium doping and cyclable hydrogen capacity of 4.5 wt% was obtained. Anton¹⁹⁰ reported the effect of a wide range of different dopants on the hydrogen sorption capacity and kinetics of Na alanates. The amount and type of dopant had a substantial effect on these parameters, however, only metal cations of the catalysis play a role in the dehydrogenation kinetics, and the most active cation additions were found to be Ti⁴⁺. Moreover, Jensen *et al.*¹⁹¹ reported the hydrogen sorption properties of catalyzed NaAlH₄, in which Ti was introduced by a novel dry doping method. It was found that the dehydrogenation of this material occurred about 30°C lower than that found previously.¹⁸⁶ This kinetic enhancement was undiminished over several dehydriding / hydriding cycles. The results also indicated that the catalytic effect in the Ti doped material is due to only a fraction amount of titanium introduced into the host hydride. Zaluska *et al.*¹⁹² investigated the hydrogen sorption properties of both NaAlH₄ and Na₃AlH₆ by mechanical grinding and chemical modification. They found that milled NaAlH₄ or Na₃AlH₆ exhibited greater enhancement of the adsorption and desorption and the mixtures of NaAlH₄ with carbon were capable of reversible dehydrogenation/ hydrogenation at much lower pressures and with much faster kinetics than conventional compounds. Furthermore, hydrogen absorption and desorption of NaAlH₄ doped with TiCl₃ were studied by dynamic in situ X-ray diffraction (XRD) under conditions similar to those found in fuel cell operations.¹⁹³ Catalyst doping was found to dramatically improve kinetics under these conditions. XRD measurements showed that TiCl₃ reacted with NaAlH₄ to form NaCl during the doping process. Thomas *et al.*¹⁹⁴ observed significant changes in the particle morphology and elemental distribution during the hydrogen desorption and cycling process of catalyzed NaAlH₄ by employing

scanning electron microscopy (SEM) and energy dispersive spectroscopy (EDS). However the mechanism of action of the catalyst was still ambiguous.

Borohydride complexes with suitable alkali or alkaline earth metals are promising classes of compounds for hydrogen storage. The hydrogen content can reach value of up to 18 wt% in gravimetric and 121 kg/m³ in volumetric for LiBH₄. However, this compound is rather stable and often desorbs the hydrogen only above their melting point temperature 280°C. The decomposition reaction of the catalyzed LiBH₄ by SiO₂-powder can be schematically describes as follows:¹⁹⁵

1. $\text{LiBH}_4 \rightarrow \text{LiBH}_{4-\varepsilon} + \varepsilon/2 \text{H}_2 \quad T=108^\circ\text{C}$
2. $\text{LiBH}_{4-\varepsilon} \rightarrow \text{'LiBH}_2\text{' + (1-\varepsilon/2)\cdot H}_2 \quad T=200^\circ\text{C}$
3. $\text{'LiBH}_2\text{' } \rightarrow \text{LiH + B + 1/2 H}_2 \quad T=453^\circ\text{C}$

This process can liberate up to 13.5 wt% at the temperature around 500°C, compared with 9 wt% at the temperature of 600°C for pure LiBH₄ sample. However, there is still total 4.5 wt% of hydrogen remaining as LiH in the decomposition product.

From the above discussion, enormous success has been achieved over the last few years in reversible hydrogen storage in complex metal hydrides. However, further efforts are still needed to lower the hydrogen desorption temperature and increase the sorption kinetics.

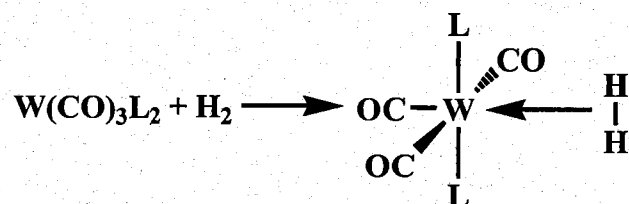
1.3 Hydrogen Storage in Microporous and Mesoporous Ti Oxides

From the above literature review, we can see some materials have shown promising hydrogen uptake,^{36, 118, 188} however there is yet no report of any material meeting or

surpassing the 2015 DOE target values, since the U.S. DOE had defined 9 wt% as a 2015 system target for gravimetric hydrogen storage. Recent advances within our group indicated that micro- and mesoporous Ti oxides could serve as hosts for hydrogen storage.¹⁹⁶ Micro- and mesoporous Ti oxides are in many ways ideal candidates for hydrogen storage because they contain ordered channels that allow hydrogen to effectively access the interior space. The synthesis is simple, highly reproducible, and cost-effective. Furthermore, the pore size, surface areas and wall thickness can be systemically modified to improve hydrogen uptake.¹⁹⁷ A unique property of this material is its ability of acting as the electron acceptor, which is due to the capacity for variable oxidation states in the walls of the micro- and mesoporous structure,¹⁹⁸ a feature not present in MOFs, zeolites or porous carbon. This exceptional property combined with the coordinative unsaturation Ti centers is likely to interact with adsorbed hydrogen more strongly than other sorbents, because binding of H₂ to transition metals is strongly dependent on the electron density at the metal center and its ability to back-bond through a π -interaction into the antibonding H-H orbital.¹⁹⁹ On this theme, two groups have recently shown that metal atoms such as Sc and Ti coated on carbon fullerenes and nanotubes can bind hydrogen in molecular forms with a binding energy of the order of 20-30 kJ/mol and with gravimetric density of up to 9 wt%.^{200, 201} In these systems it was proposed that a Kubas-type binding of H-H σ -bond to an electron rich coordinatively unsaturated metal center played an important role for both the high hydrogen sorption capacities and the ideal hydrogen binding enthalpies.

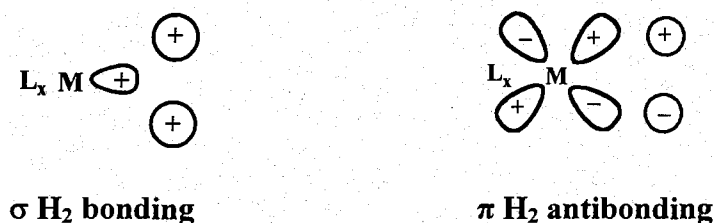
Actually, Kubas-type interactions have been known for a long time. Since the 1980s, many hydrogen molecular complexes of transition metals have been isolated and

characterized at low temperature. The Scheme 1 represents an example of a molecular hydrogen complex.²⁰²



Scheme 1. Schematic illustration of a molecular hydrogen complex.

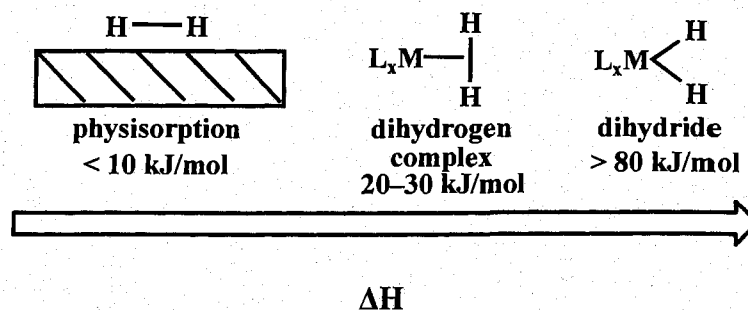
In the dihydrogen complex, the chemical bond in the hydrogen molecule interacts with the metal center through σ bonding and a subsequent π back-donation from the partially filled d-orbitals of the metal into the hydrogen antibonding orbital, as illustrated in Scheme 2. This Kubas-type interaction leads to a relatively strong binding of molecular hydrogen without cleaving the H-H bond to form a dihydride.



Scheme 2. Schematic representation of $\sigma \text{ H}_2$ bonding and $\pi \text{ H}_2$ antibonding in a Kubas-type interaction.

From the preceding literature review, it is clearly shown that the hydrogen binding enthalpy in chemisorption hydrogen storage system such as metal hydrides is too high (>80 kJ/mol), which caused high hydrogen desorption temperature, slow kinetics and heat management issues. On the other hand, the very small (<10 kJ/mol) hydrogen

enthalpies in physisorption results in the need for cryogenic conditions to achieve high storage capacities. The formation of dihydrogen complex by the Kubas-type interaction represents a middle stage of these two interactions. Scheme 3 demonstrates the change in trend of hydrogen enthalpies for these three types of hydrogen binding.



Scheme 3: Schematic illustration of the change in trend of hydrogen enthalpies from physisorption to chemisorption.

For porous materials, it has been proposed that the hydrogen enthalpies between 20-30 kJ/mol are ideal values to operate under ambient temperature. Such values could be reached by formation of the dihydrogen complex with the Kubas-type interaction. Although some theoretical calculations have already predicted promising results,^{200,201} to date, there is no experimental study demonstrating the feasibility of this approach. With this goal in mind, in this thesis, mesoporous and microporous titanium oxides were reduced and/or impregnated by a variety of reducing agents, such as alkali metals, organometallic sandwich compounds of Ti, V, and Cr, as well as alkali fullerides. The hydrogen sorption properties of both the pristine materials and new reduced composite materials will be comprehensively investigated in order to achieve practical hydrogen storage materials.

Chapter 2. Hydrogen Storage in Chemically Reducible Mesoporous and Microporous Ti Oxides

Previous study in our group have shown that the mesoporous transitional metal oxides can be reduced with up to one equivalent of alkali metal to lead to new reduced transitional metal oxide mesostructures with potential application as electron storage materials and fast ion conduction channels.^{203, 204} In other works^{205, 206}, bis(toluene) Ti was found to effectively reduce the transitional metal mesostructures leaving a low valent coat of Ti on the surface. The reduced surface and the new introduced active site may be beneficial to the hydrogen storage capacity for these materials. In order to verify this, in this chapter we report a comprehensive study of hydrogen storage at 77 K of pristine and chemically modified meso- and microporous Ti oxides, which take advantage of the reducible nature of the surface to tune the binding enthalpies and hydrogen storage capacity.

2.1. Experimental Section

2.1.1. Materials and Equipment

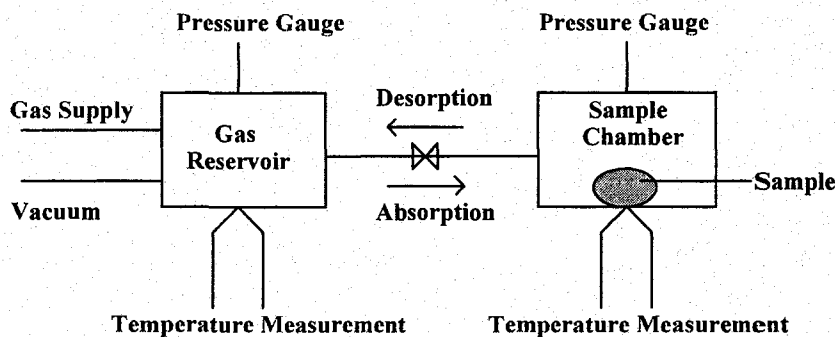
All chemicals unless otherwise stated were obtained from Aldrich. Bis(toluene) titanium was synthesized by F. G. N. Cloke at the University of Sussex by metal vapor synthesis. Trimethylsilyl chloride was obtained from Alfa and distilled over calcium hydride. In order to remove an excess of moisture and cap OH groups on the internal surface of the titanium oxide mesostructure, which can interfere with the intercalation

process by forming metal hydroxide on the internal surface, micro- and mesoporous Ti oxides samples were dried at 150°C overnight under vacuum and then stirred with excess trimethylsilyl chloride in dry ether for 12 h under nitrogen. Nitrogen adsorption and desorption data were collected on a Micromeritics ASAP 2010. X-ray diffraction (XRD) patterns (Cu K α) were recorded in a sealed glass capillary on a Siemens D-500 θ -2 θ diffractometer. TEM images were obtained by using a H9000 HR-TEM operated at 300 kV. The skeletal densities of the samples were measured by a Quantachrome Micro-Ultracycrometer 1000 using helium gas. Determination of apparent density of the material is a common practice and is readily accomplished by dividing the mass of the packed powders by the volumes they occupied.

2.1.2. H₂ Sorption Measurements

The reason of big discrepancy in hydrogen storage abilities for the carbon nanostructured materials can be due to the inaccurate measurement. The high accuracy and reproducibility of the hydrogen adsorption apparatus become very important. In this study, the hydrogen adsorption/desorption isotherms have been measured by a computer-controlled commercial 'Gas Reaction Controller' manufactured by the Advanced Materials Corporation of Pittsburgh, PA. Ultra-high purity hydrogen gas (99.9995% purity) was used as the adsorbate. Typically, the mass needed for the hydrogen sorption measurement is 500-1000 mg. All the reduced materials were loaded into the sample test holder under the N₂ atmosphere within the glove box to prevent exposing to oxygen and moisture during weighting and transfers. The size of the sample chamber is 2.5 cm³.

Lightly packed powder materials were used for all measurements. Before all measurements the materials were degassed at 200°C under a high vacuum at 10^{-3} Torr for at least 1 day to remove any physisorbed water or volatile impurities. A simplified sketch of this apparatus is shown as follows:



Scheme 4: Schematic drawing of Gas Reaction Controller system manufactured by Advanced Materials Corporation.

The temperature of the gas reservoir is measured by two AD590 IC thermometers that are calibrated against a standard mercury thermometer within 0.1 °C at room temperature. The sample temperature is measured with a type K thermocouple by converting voltage reading to temperature according to ITS-90 (The International Temperature Scale of 1990). The limits of error are 2 °C or 0.75 % above 0 °C and 2 °C or 2 % below 0 °C. The pressure of both gas reservoir and sample chamber is measured by Heise model HP0 pressure transducer, which has a full scale range of 1500 psi (about 100 atm). The accuracy of this transducer is rated to be 0.05 % of the full scale including nonlinearity, drift, and hysteresis. The GRC operates by admitting an appropriate amount of gas to the reservoir and determines its molar amount from its pressure and temperature. The system then manipulates the valves between the reservoir and the

reaction chamber and transfers a desired amount of the gas from the reservoir to the gas reaction chamber. After equilibrium is attained, the system recalculates the number of hydrogen molecules. The number missing from the gas phase corresponds to the number of molecules absorbed by the sample. The system employs a modified Benedict-Webb-Rubin equation of state in calculating the amount of absorbed hydrogen from the pressure, temperature, and volume. The apparatus gradually increases the hydrogen pressure to the maximum specified value, while summing the adsorbed hydrogen. The amount of hydrogen released from the sample is then determined by pumping out the gas reservoir and gradually bleeding hydrogen from the sample chamber into the gas reservoir. During the cryogenic test process, the sample chamber is immersed in liquid nitrogen, and the liquid level is maintained constant throughout the experiment.

The apparatus was tested for accuracy through calibration with well known LaNi_5 at room temperature and AX-21 at 77 K. Figure 1 shows the hydrogen adsorption isotherm of LaNi_5 at room temperature. The hydrogen adsorption capacity of 1.5 wt% agrees well with previous measurement.⁴¹

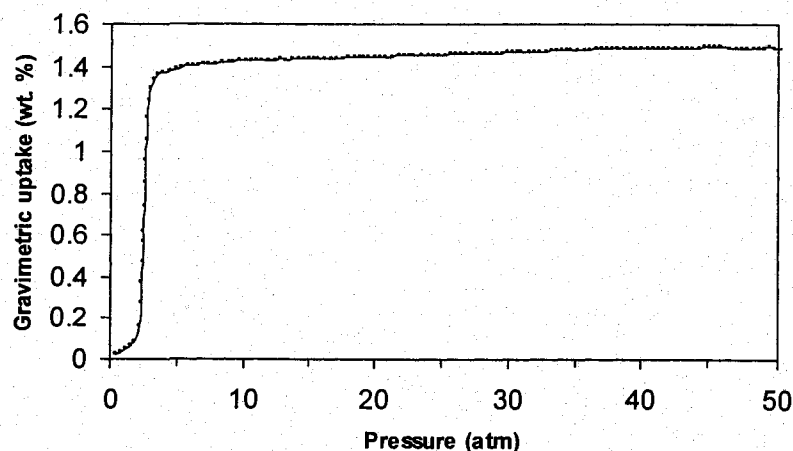


Figure 1. Hydrogen adsorption isotherm for LiNi_5 at room temperature.

Figure 2 shows the hydrogen adsorption isotherm for AX-21 at 77 K. The hydrogen uptake of 4.2 wt% is consistent with previous studies.^{58, 59} From above results, the apparatus and our measurement procedures have been proven highly accurate and reproducible.

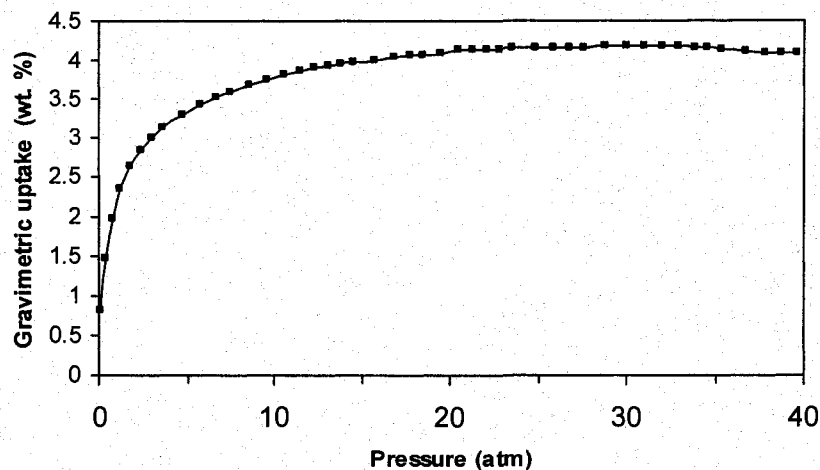


Figure 2. Hydrogen adsorption isotherm for AX-21 at 77 K.

This apparatus effectively measures the pressure of the hydrogen in the sample chamber and then calculates the number of moles on the basis of this pressure, the temperature and the volume, which is arrived at by subtracting the sample volume (obtained by direct input of the sample weight and density) from the empty chamber volume. If the density used is the skeletal density measured by a pycnometer, the compressed hydrogen within the pores is treated as part of the sample chamber volume, but if the apparent density of the sample is used instead, the compressed gas in the pores is treated as having been absorbed by the sample along with the hydrogen physisorbed to the walls of the skeletal structure. The advantage of this system is that you do not have to make assumptions on the void space volume of the material to obtain the total amount of

H₂ in the system (including the compressed gas in the void space), which is crucial in determining the amount of useful fuel stored in the material. Most other Sieverts apparatuses work by automatically subtracting out the compressed gas in the pores, obviating the use of the pycnometer, but making determination of the compressed gas in the pores more ambiguous. Gravimetric adsorption (equivalent to what is often called “excess storage”) and total storage are measured directly, whereas volumetric densities for both values are calculated using the apparent densities. Many groups choose not to quote total storage because this value is not directly related to the surface properties of the material, but only represents a sum of all hydrogen present within the volume occupied by the material at any given pressure.

Enthalpies of adsorption were calculated using a variant of the Clausius-Clapeyron equation taking both the 77 and 87 K hydrogen adsorption data.

$$\ln\left(\frac{P_1}{P_2}\right) = \Delta H_{ads} * \frac{T_2 - T_1}{R * T_1 * T_2} \quad (1)$$

Where P_n= pressure for isotherm n, T_n=temperature for the isotherm n, and R=gas constant.

Pressure as a function of the amount adsorbed was determined by using exponential fit for each isotherm. This exponential equation gives an accurate fit over the pressure up to 10 atm and with the goodness of fit (R²) above 0.99. The corresponding P₁ and P₂ values at a certain amount of H₂ adsorbed at both temperatures can be obtained by the simulated exponential equation. Inputting these numbers into the eq 1, we then calculated the enthalpies of the adsorption.

2.1.3. Synthesis

Synthesis of Microporous Titanium Oxide Materials: In a typical preparation, titanium (IV) isopropoxide (15 g, 52.77 mmol) was warmed with hexylamine (2.67 g, 26.39 mmol) until a homogeneous colorless solution was obtained. To this solution was added 75 mL water with stirring. Precipitation occurred immediately. 37% HCl (0.2603 g, 2.639 mmol) was then added to the mixture. The mixture was allowed to sit at room temperature overnight without agitation before being transferred to an oven for aging at 40 °C for 2 days, 60 °C for 2 days, and 80 °C for 4 days. The suspension was then filtered by suction filtration, and the white solid was placed into a sealed tube and put into an oven at 100 °C for 2 days, 120 °C for 2 days, and 140 °C for 2 days. The product was collected by suction filtration and washed once with a mixture of methanol (375 ml) and diethyl ether (125 ml), and four times with 500 ml methanol. The resulting materials were put into an oven at 150°C for 2 days.

Synthesis of Li and Na Reduced Microporous Titanium Oxide Materials: To a suspension of the alkali metal (caution) in THF in an inert atmosphere glovebox was added 1.0 equivalent of naphthalene. The mixture was stirred until the solid was completely consumed. On the basis of 38% Ti as determined from elemental analysis data, 1.0 equivalent of the trimethylsilated microporous titanium was added to the THF solution. After additional stirring overnight, the reduced material was collected by suction filtration and washed several times with THF. The materials were then dried in vacuo at 10^{-3} Torr on a Schlenk line until all condensable volatiles had been removed.

Synthesis of Bis(toluene) Titanium Reduced Microporous Titanium Oxide

Materials: Excess bis(toluene) titanium, as calculated on the basis of 38% Ti in the porous oxide, was added to a suspension of trimethylsilated microporous titanium oxide in dry toluene under nitrogen. After 1 day of stirring to ensure complete absorption of the organometallic, the reduced material was collected by suction filtration under nitrogen and washed several times with toluene. The resulting blue black material was dried in vacuo at 10^{-3} Torr on a Schlenk line until all condensable volatiles had been removed.

2.2 Results

2.2.1. X-ray Powder Diffraction (XRD) Pattern, Nitrogen Adsorption Study of Unreduced Mesoporous and Microporous Ti Oxides

A series of five pristine micro- and mesoporous Ti oxide materials were synthesized as described above from C₆, C₈, C₁₀, C₁₂, and C₁₄ amine templates (C₆-C₁₄ Ti). Figure 3 shows the XRD patterns for these pristine materials. All the patterns display a broad peak at low angle and the absence of any other peaks in higher angle indicates that these materials possess wormhole micro- or mesoporous structure. A synthesis of mesoporous Nb oxide was previously extended down to the micropore region by Sun and Ying²⁰⁷ using templates as small as butylamine, however there are no reports of microporous Ti oxide being synthesized by this route using amine templates with chain lengths smaller than C₁₂. The XRD pattern (Figure 3) for the material synthesized with hexylamine as a template (C₆-Ti) revealed single peak centered at $d = 25$ Å. Figure 4 shows the nitrogen

adsorption/desorption isotherms for all the unreduced materials, of which, C6-Ti revealed a type I isotherm consistent with a microporous system and surface area of 942 m²/g. The pore volume of this material was 0.673 cm³/g, while the pore size could only be estimated from this technique at 12 Å from the XRD data and previous work on the Nb system,²⁰⁷ since nitrogen adsorption is not useful for determining pore sizes below ca. 20 Å. However, TEM of this material (Figure 5) revealed a pore diameter of around 12 Å, fully consistent with this estimate. The pore sizes of these pristine materials decreased monotonically from 26 Å to 12 Å as described previously for a similar series of porous Nb oxides.²⁰⁷ All the XRD and nitrogen adsorption data for both these unreduced materials and reduced materials in this study are summarized in Table 2.

Table 2. Nitrogen adsorption and XRD results of Ti oxide materials.

Sample	BET surface area (m ² /g)	BJH pore volume (cm ³ /g)	d-space of XRD (Å)
C6-Ti	942	0.673	25
C8-Ti	1063	0.595	26
C10-Ti	706	0.378	28
C12- Ti	737	0.407	30
C14- Ti	643	0.534	32
Li C6-Ti	499	0.504	25
Na C6-Ti	480	0.460	25
BTTi C6-Ti	208	0.084	25

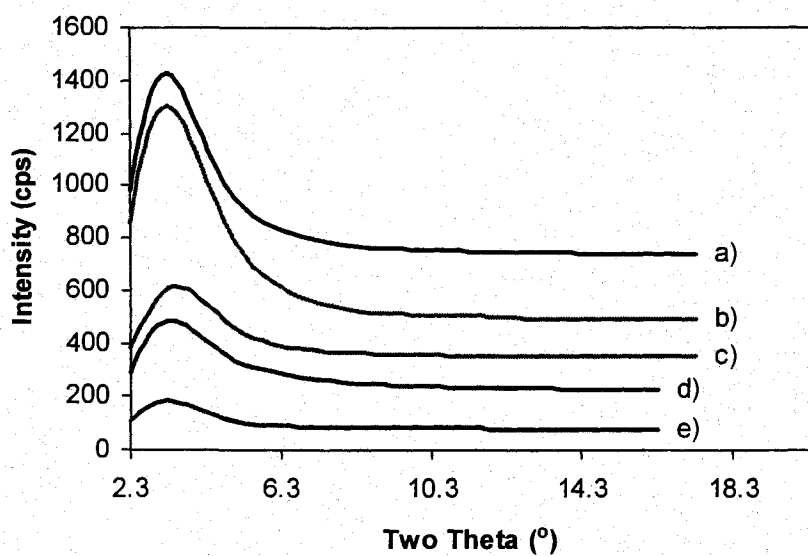


Figure 3. XRD spectra of a) C6-Ti, b) C8-Ti, c) C10-Ti, d) C12-Ti, e) C14-Ti.

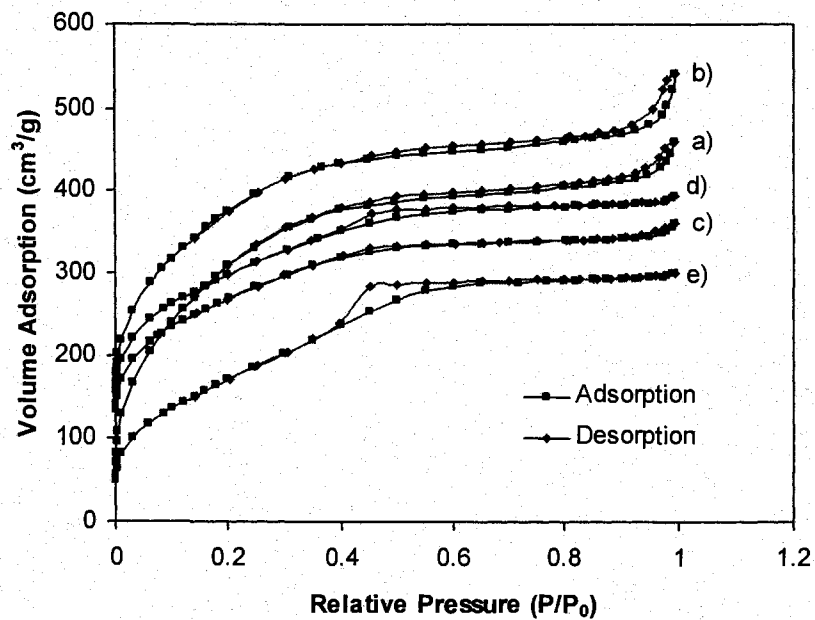


Figure 4. Nitrogen adsorption/desorption isotherms of a) C6-Ti, b) C8-Ti, c) C10-Ti, d) C12-Ti, e) C14-Ti.

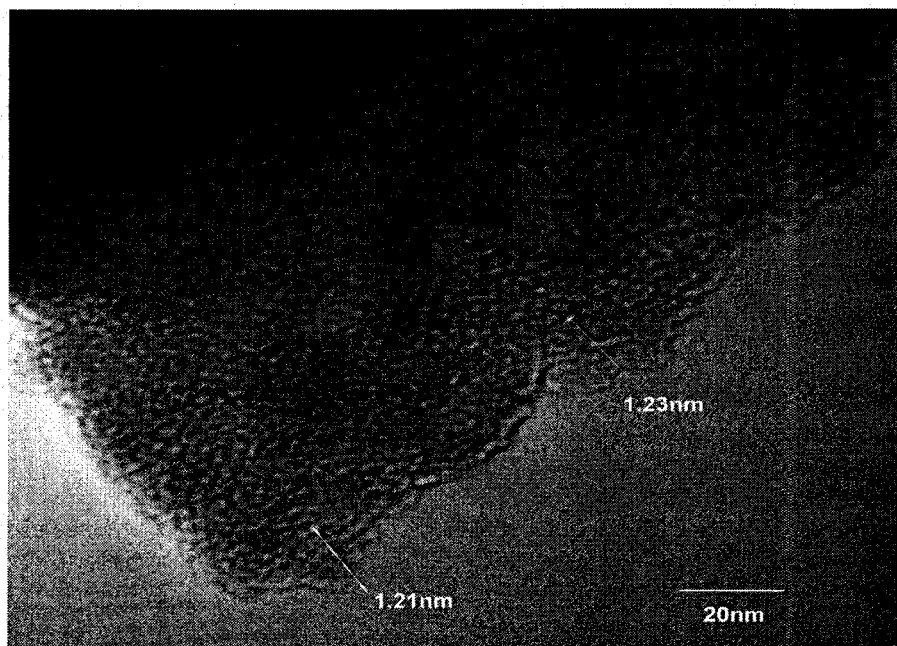


Figure 5. TEM image of C6-Ti.

2.2.2. Hydrogen Sorption Properties of Unreduced Mesoporous and Microporous Ti Oxides

Hydrogen pressure-composition isotherms were recorded at 77 K for all the pristine microporous and mesoporous Ti oxides. Hydrogen storage isotherms and adsorption isotherms are shown in Figure 6a and Figure 6b, respectively.

The adsorption values reflect the amount of hydrogen bound to the surface of the porous framework, while the storage is a measure of the total H₂ available as fuel in any system (i.e. the sum of the adsorption and the compressed gas in the pores). The former value is useful in studying surface binding, while the latter is a measure of the total H₂

available as fuel in any system. These results and all other hydrogen sorption results in this study are summarized in Table 3, complete with extrapolation to 100 atm.

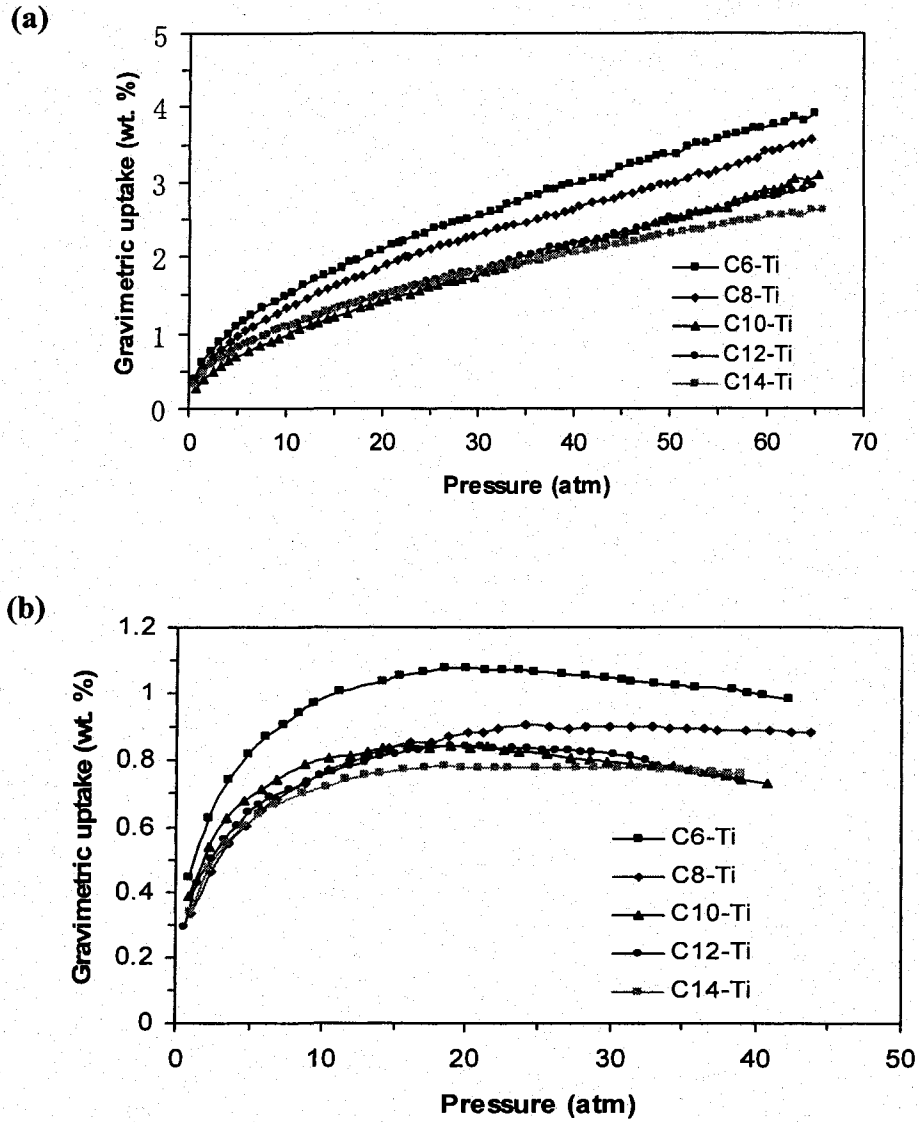


Figure 6. (a) Hydrogen storage isotherms, (b) Hydrogen adsorption isotherms for all the unreduced Ti materials.

The storage isotherms (Figure 6a) for all materials rise sharply at low pressure and continue to rise in a linear fashion from 10 atm onwards to 65 atm. Reversibility was evaluated by measuring the desorption branch down to near zero atm. The desorption branches follow the adsorption branches without significant hysteresis. The adsorption/desorption process was fast and thermodynamic equilibrium was reached within a few seconds, indicating a very low activation barrier for this process. For the adsorption isotherms (Figure 6b), the hydrogen capacity increases with increasing pressure until saturation is achieved, after which the hydrogen capacity begins to drop, a typical feature of supercritical adsorption.²⁰⁸ Extrapolation to 100 atm, a feasible pressure for cryogenic storage tanks, yields a total storage values as high as 5.36 wt% and 29.37 kg/m³ for the C₆ sample. Storage measurements of a compressed pellet of this material showed gravimetric and volumetric densities of 2.63 wt% and 30.45 kg/m³ at 77 K and 100 atm, demonstrating that densification of this material gives only a slight increase in volumetric density with a large penalty in gravimetric density. The lowest storage value of these pristine materials was found to be 3.51 wt% and 25.20 kg/m³ in C14-Ti. The adsorption shows a decrease from 1.08 wt% and 5.918 kg/m³ in C6-Ti to 0.79 wt% in C14- Ti and 5.396 kg/m³ in C8- Ti. From the results of Table 3, the general trend in this series of titanias appears to be one of increasing surface area and decreasing pore size leading to more effective hydrogen storage. Both of these factors have been implicated in hydrogen physisorption to amorphous carbons and nanotubes. In MOF materials, it has been proposed that H₂ can bind to the metal linker and that this feature is just as important as the surface area and pore size in determining storage capacity.¹¹² It is therefore possible that such σ binding of H₂ to Ti can occur in our system, where the Oh MX₄L₂ Ti

centers¹⁹⁸ present at the surface and in the walls are nominally electron deficient 12 electron species possessing vacant t_{2g} orbitals. A schematic representation of a monolayer portion of the wall is shown in Figure 7, in which H_2 molecules can potentially bind to the Ti centers via a side-on interaction to the d^0 center through the Ti t_{2g} set,^{199, 200} or can exist as a compressed gas phase within the pore structure of the material. While anatase and rutile are poor hydrogen storage materials, the low-density amorphous structure of the walls in our materials preserves a degree of coordinative unsaturation while also allowing easy access of the H_2 to the Ti centers.

Table 3. Hydrogen sorption capacities of pristine and reduced Ti oxide materials and AX-21.

Sample name	Surface area (m ² /g)	Apparent Density (g/ml)	Skeletal Density (g/ml)	Gravimetric Adsorption (wt %)	Gravimetric H ₂ storage (wt %) ^a	Volumetric Adsorption (kg/m ³)	Volumetric H ₂ storage (kg/m ³) ^a
C6-Ti	942	0.548	2.698	1.08	5.36	5.918	29.37
C8-Ti	1063	0.593	2.730	0.91	4.82	5.396	28.58
C10-Ti	706	0.645	2.531	0.89	4.30	5.741	27.74
C12-Ti	737	0.656	2.708	0.85	4.07	5.576	26.70
C14-Ti	643	0.718	2.815	0.79	3.51	5.672	25.20
Li C6-Ti	499	0.556	2.508	0.71	5.63	3.948	31.30
Na C6-Ti	480	0.565	2.741	0.92	5.58	5.198	31.58
BTTi C6-Ti	208	0.819	2.835	1.14	4.94	9.337	40.46
AX-21	3225	0.328	2.103	4.19	11.96	13.75	39.23

^a Hydrogen measurement is at the temperature of 77 K and 65 atm extrapolated to 100 atm with goodness of fit (R^2)= 0.9963~0.9995.

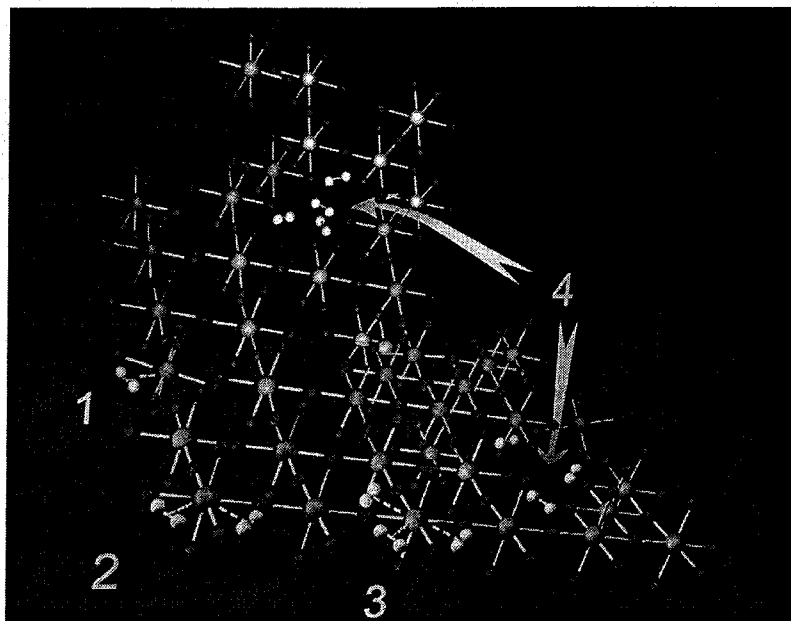


Figure 7. Schematic representation of H_2 binding sites in the monolayer wall of micro- and mesoporous titanium materials, where 1, 2, and 3 refer to mono, bis, and tris dihydrogen complexes, respectively, and 4 represents the compressed gas phase in the porous voids in the solid. Reduction of the 12-electron MX_4L_2 Ti octahedra leads to population of the t_{2g} set and more effective π back bonding to the H_2 molecules.

The binding enthalpies of unreduced materials were calculated by a variant of the Clausius-Clapyron equation²⁰⁹ from hydrogen adsorption data at 77 and 87 K (see Figure 8). The plots show a decrease in ΔH with H_2 capacity, which is typical for physisorption. The maximum ΔH was 5.32 kJ/mol for C14-Ti, similar to the value calculated for amorphous carbon.⁵⁷

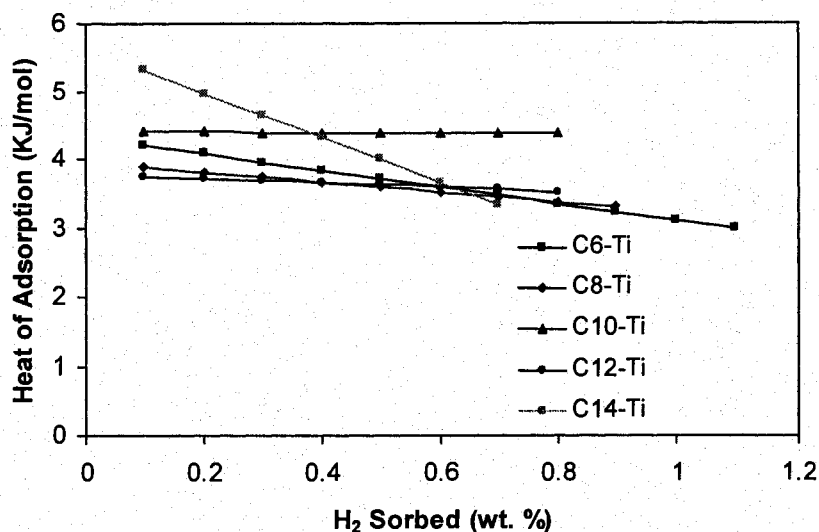


Figure 8. Enthalpies of H₂ adsorption for pristine Ti oxide materials.

2.2.3. X-ray Powder Diffraction (XRD) Pattern, Nitrogen Adsorption Study of Li, Na and Bis(toluene) Titanium Reduced Microporous Titanium Oxide Materials

In order to explore the role of Ti oxidation state in H₂ storage capacity, C6-Ti was reduced with a variety of organometallic species. Figure 9 shows the XRD patterns for C6-Ti, C6-Ti reduced with 1.0 mol equivalent of Li naphthalene (Li C6-Ti), C6-Ti treated with 1.0 mol equivalent of Na naphthalene (Na C6-Ti), and C6-Ti reduced with excess bis(toluene) Ti (BTi C6-Ti). Figure 10 shows the nitrogen adsorption/desorption isotherms for all these C6-Ti materials. The XRD and nitrogen adsorption data shown in Table 2 indicate that the wormhole pore structures of these reduced materials were retained.

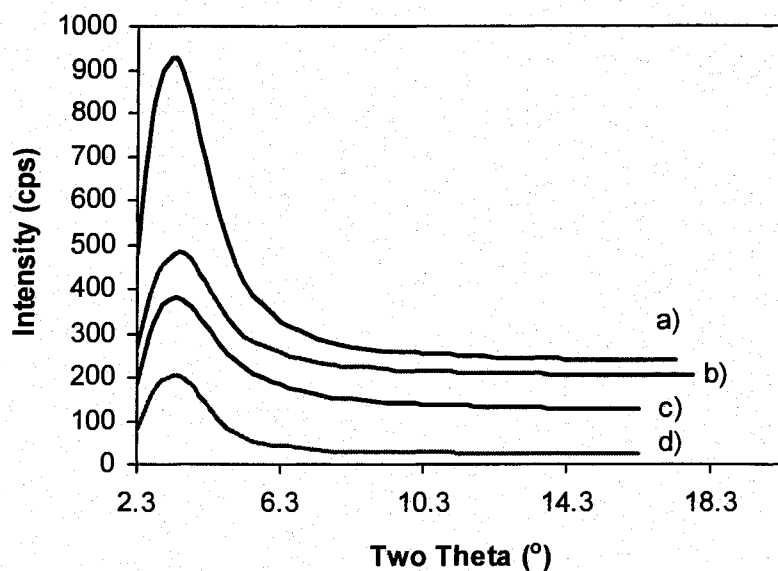


Figure 9. XRD spectra of a) C6-Ti, b) Li C6-Ti, c) Na C6-Ti, d) BTTi C6-Ti.

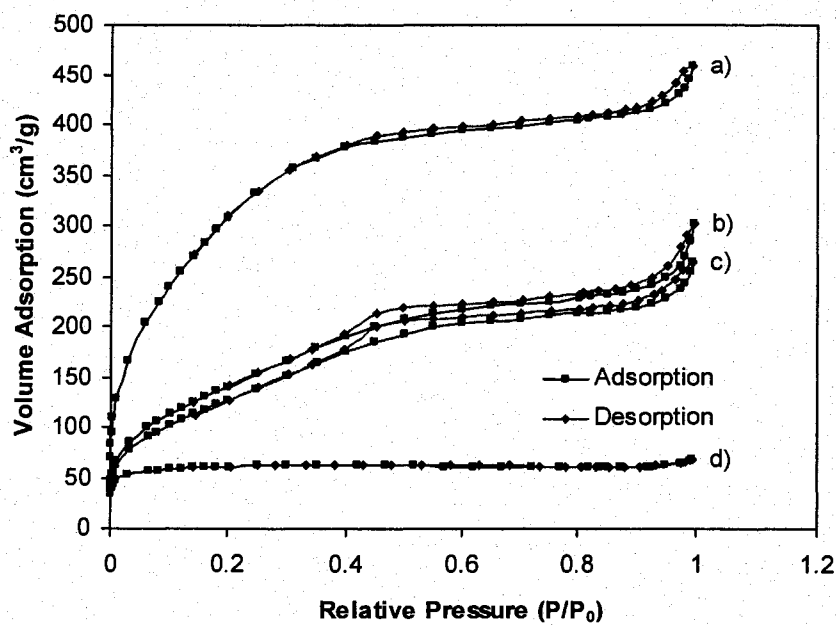


Figure 10. Nitrogen adsorption/desorption isotherms of a) C6-Ti, b) Li C6-Ti, c) Na C6-Ti, d) BTTi C6-Ti.

2.2.4. Hydrogen Sorption Properties of Li, Na and Bis(toluene) Titanium Reduced Microporous Titanium Oxide Materials

Figure 11 shows the H₂ sorption isotherms at 77 K for pristine and reduced C6-Ti materials. The results are summarized in Table 3, complete with extrapolations to 100 atm. Direct measurements of AX-21 are shown for comparison. From all these data, we can see that reduction of C6-Ti with Li leads to an increase in gravimetric storage capacity from 5.36 wt% to 5.63 wt% and an increase in the volumetric storage capacity from 29.37 kg/m³ to 31.30 kg/m³ at 77 K and 100 atm. The Na-reduced material exhibits a slight decrease in gravimetric storage over the Li-reduced material, but possesses a higher volumetric storage capacity of 31.58 kg/m³. The slight decrease in gravimetric storage density is due to the greater molecular weight of Na with respect to Li, while the overall increased storage efficiency reflected in the volumetric capacity can be attributed to the greater ability of Na to donate electron density to the Ti center and thus facilitate a π back bonding interaction with H₂. Treatment of C6-Ti with bis(toluene) Ti leads to a decrease in the gravimetric storage to 4.94 wt% and an increase of the volumetric storage to 40.46 kg/m³, higher than that measured for AX-21. The adsorption data show a decrease from 1.08 wt % and 5.918 kg/m³ in C6-Ti to 0.71 wt% and 3.948 kg/m³ in Li C6-Ti and 0.92% and 5.198 kg/m³ in Na C6-Ti, and an increase to 1.14 wt% and 9.337 kg/m³ in BTTi C6-Ti. Equilibration for all reduced materials is immediate and there is no hysteresis between the adsorption and desorption cycles. An increase in temperature is not required for full discharge. At room temperature, BTTi C6-Ti has a hydrogen gravimetric storage capacity of 1.3 wt% at 100 atm.

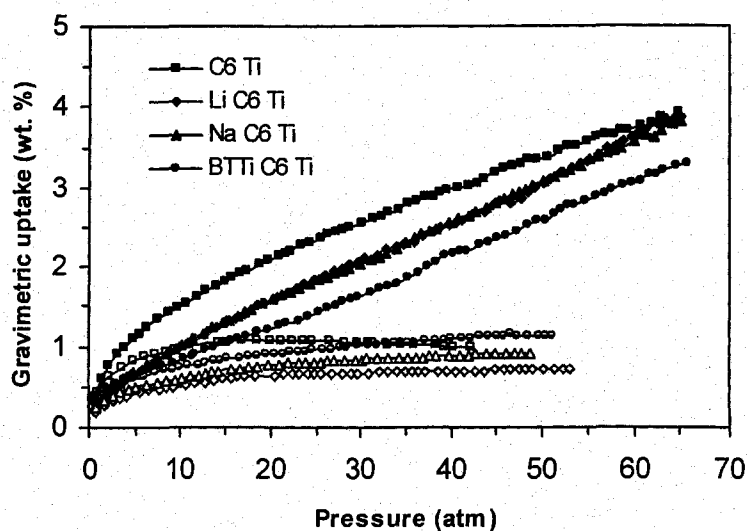


Figure 11. High-pressure H₂ isotherms for pristine and reduced C6-Ti materials at 77 K in gravimetric uptake. Filled markers represent storage capacity and open markers denote adsorption capacity.

Cycling studies of BTTi C6-Ti conducted at 77 K and 65 atm demonstrate that the material does not lose any of its storage capacity after 10 cycles (Figure 12). The binding enthalpies were calculated by a variant of the Clausius-Clapyron equation²⁰⁹ from hydrogen adsorption data at 77 and 87 K (see Figure 13). Compared with the plot for C6-Ti, which decreases with increasing capacity, however, the plots for all reduced materials show an increase in ΔH with H₂ capacity, a behavior which is highly unusual and may reflect a different mechanism of surface binding than simple physisorption, possibly involving a Kubas-type interaction. Li C6-Ti possesses a ΔH of 5.79 KJ/mol, while Na C6-Ti has a ΔH of 5.87 KJ/mol. BTTi C6-Ti has a ΔH of 8.08 KJ/mol, which compares well with values determined by Kaye *et al.*¹³¹ for MOFs materials, in which transition

metals are thought to act as H₂ binding sites, but falls far short of the 20 kJ/mol value proposed for porous materials to function effectively at ambient temperature.¹¹²

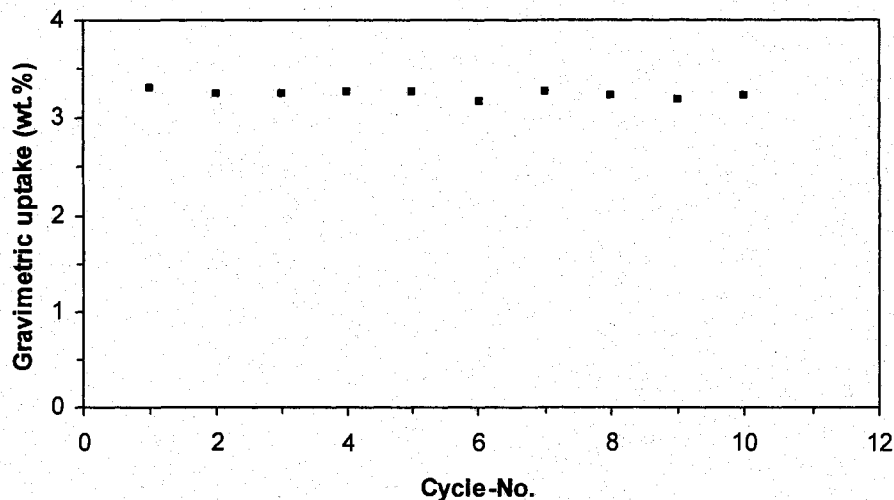


Figure 12. Hydrogen storage capacity in a 10 cycle test of BTTi C6-Ti at 77 K and 65 atm.

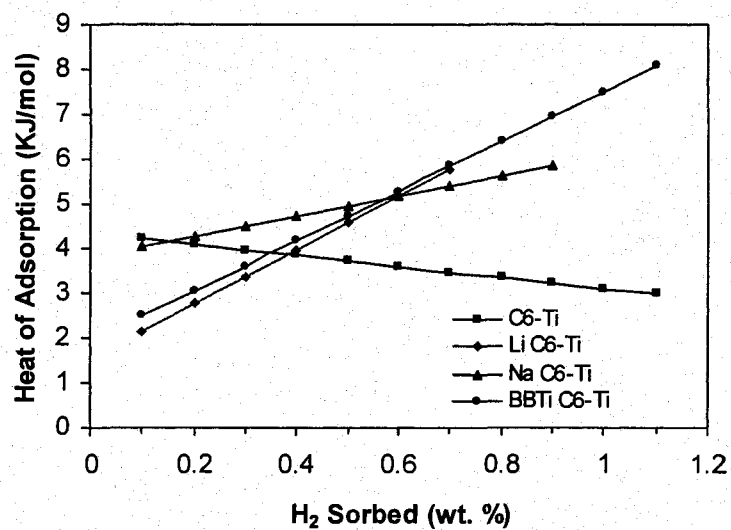


Figure 13. Enthalpies of H₂ adsorption for pristine and Li, Na and bis(toluen) titanium reduced microporous titanium oxides.

2.3. Discussion

The improved performance of this series of composite materials relative to the untreated sample was attributed to the increased reduction level of the metal centers in the framework of the structure, which allows for more facile π -back donation to the antibonding H-H orbital. Unlike MOFs and porous carbons, the hydrogen sorption performance of these new reduced composites does not depend greatly on surface area. For example, the material reduced with bis(toluene) Ti possesses a surface area of less than 300 m²/g, but absorbs up to 4.94 wt% and 40.46 kg/m³ of H₂ reversibly at 77 K and 100 atm. This volumetric storage capacity is higher than that of AX-21, which has a much higher surface area. In other work we showed that this reagent reduces the Ti centers in the mesostructure, while also depositing a thin coat of low valent Ti on the surface of the material.²⁰⁶ While the exact oxidation state of the Ti in the material is difficult to define due to the non-stoichiometry, the high level of reduction of this material is reflected in its metallic properties, usually only seen in Ti oxides for Ti(II)O. The low-coordinate, low-valent nature of the surface Ti species is further illustrated by its ability to cleave dinitrogen,²⁰⁶ a process which is known to require a high degree of coordinative unsaturation and a strongly reducing metal center, both factors which also contribute to more effective H₂ binding. Previous XPS studies^{203, 204, 206} showed that for alkali metal reduced mesoporous Ti oxides, the Ti 3p 3/2, 1/2 emissions decreased by roughly 0.4 eV for every step down the group and a progressive reduction in the surface Ti species from Li to Na to bis(toluene) Ti (Table 4), however establishment of a uniform trend relating Ti oxidation state to H₂ capacity is difficult due to the differing densities,

surface areas, and void space volumes of these materials. In spite of this uncertainty, it is clear from the data that treatment with bis(toluene) Ti leads to the most dramatic overall increase in performance, possibly due to its greater degree of reduction and additional Ti binding sites (C6-Ti is 38% Ti; BTTi C6-Ti is 51% Ti).²⁰⁶ Another surprising feature in these reduced materials is the unusual trend in enthalpies, which show an unprecedented increase in binding strength as the surface coverage increase. This is the opposite of all other cryogenic hydrogen storage materials, which show a small decrease with increasing surface coverage. As the surface becomes more crowded with hydrogen molecules, the effect of intermolecular repulsion becomes more important and begins to offset the Van der Waals forces between the molecule and surface. An increase in binding enthalpy on surface coverage can only be explained in terms of the hydrogen molecules chemically or electronically modifying the surface, such that the surface interactions with subsequent hydrogen molecules are strengthened. Because hydrogen binding to transition metals normally increases with increased electron density at the metal, it is fair to suggest that increased surface coverage leads to an increased electron richness at the metal center due to σ donation of the electrons in the H-H bonding orbital to the Ti centers. The increased electron density at the metal then leads to more effective π -back donation to the antibonding H-H orbital and hence higher binding enthalpies. Although this is still speculative and other effects may be at play, it is difficult to verify any mechanism without *in situ* spectroscopic studies at low temperature, which are experimentally challenging due to the requirement of high hydrogen pressures and cryogenic temperatures in the sample cell. Since our materials shows potential for even further

reduction by chemical reagents, the achievement of higher enthalpies and storage densities appears promising at this stage.

Table 4. XPS results for pristine and reduced amine-templated materials.

Materials	Binding Energy of Ti 3p 1/2 (eV)
Unreduced Ti	37.9 ^a
Li reduced Ti	36.8 ^a
Na reduced Ti	36.4 ^b
BTTi reduced Ti	35.1 ^a

^a From ref. 206. ^b From ref. 204.

2.4. Conclusion

In summary, micro- and mesoporous Ti oxide materials with a range of pore sizes from ca. 12 to 26 Å and surface areas from 643 to 1063 m²/g were prepared and screened for H₂ storage capacity. While surface area and pore size had some effect on storage, surface Ti reduction provided an even greater increase in performance, possibly due to a Kubas-type interaction. These results suggest that reduction by the appropriate organometallic reagent may lead to even greater storage densities at temperatures higher than 77 K with more precise control over the enthalpies of adsorption.

Chapter 3. Hydrogen Storage in Microporous Titanium Oxides Reduced by Early Transition Metal Organometallic Sandwich Compounds

In Chapter 2, it has been shown that the reduction in surface Ti provides a greater increase in hydrogen sorption performance than surface area and pore size.²¹⁰ For example, the microporous Ti material reduced with bis(toluene) Ti possesses a surface area of 208 m²/g, but exhibits an overall volumetric storage capacity of 40.46 kg/m³ at 77 K and 100 atm. This volumetric storage capacity is higher than that of pristine material which has a surface area of 942 m²/g. Another surprising feature in these reduced materials is that reduction of the microporous Ti oxide surface also leads to a dramatic change in the enthalpy properties, resulting in higher enthalpies of adsorption, which increase on hydrogen loading, suggesting a different mechanism than simple physisorption, possibly involving a Kubas-type interaction. However, in order to verify this, more experimentation is necessary. In previous reports, our group showed that mesoporous Nb oxide can act as a potent stoichiometric electron acceptor.²⁰³ Although alkali metals are capable of reducing the framework by a total of one oxidation state without loss of the mesostructure,²⁰³ organometallic reductants such as bis(benzene) chromium, bis(cyclopentadienyl) chromium, bis(benzene) vanadium and bis(cyclopentadienyl) vanadium, deposit transition metal atoms on the surface or leave mixed-oxidation-state phases within the pores of the structure, depending on the compound.²¹¹⁻²¹³ Since these compounds act as reducing agents and leave low-valent transition metal residues behind, which themselves may serve as binding sites for H₂, it

stands to reason that they may function as useful dopants to improve the hydrogen storage performance of microporous Ti oxides. Herein we synthesize and investigate the hydrogen-sorption properties of bis-arene and bis-cyclopentadienyl transition-metal-reduced microporous titanium oxide composites in order to exploit the reducible nature of the surface to tune the binding enthalpies and hydrogen storage capacities.

3.1. Experimental Section

3.1.1. Materials and Equipment

All chemicals unless otherwise stated were obtained from Aldrich. All other materials and equipments unless otherwise stated here were the same as those shown in Chapter 2. Bis(benzene) chromium, bis(cyclopentadienyl) chromium and bis(cyclopentadienyl) vanadium were obtained from Strem Chemicals. Bis(benzene) vanadium was prepared according to the literature.²¹⁴ All X-ray photoelectron spectroscopy (XPS) peaks were referenced to the carbon C-(C, H) peak at 284.8 eV, and the data were obtained using a Physical Electronics PHI-5500 spectrometer using charge neutralization.

All elemental analysis data (conducted under an inert atmosphere) were obtained from Galbraith Laboratories, Knoxville, TN.

3.1.2. Synthesis

Synthesis of Bis(benzene) and Bis(cyclopentadienyl) Transition-Metal-Reduced Microporous Titanium Oxides: Excess organometallic, as calculated on the basis of metal percent derived from the elemental analysis data (ca. 38% Ti), was added to a

suspension of microporous titanium oxide in dry benzene under nitrogen. The microporous solid immediately went from a light fawn color to a dark color. After 2 days of stirring to ensure complete absorption of the organometallic, the reduced material was collected by suction filtration under nitrogen and washed with successive 20-mL aliquots of benzene. The resulting materials were dried in vacuo at 10^{-3} Torr on a Schlenk line until all volatiles had been removed.

3.2. Results

3.2.1. X-ray Powder Diffraction (XRD) Pattern, Nitrogen Adsorption Study and Elemental Analysis of Bis(benzene) Chromium Reduced Microporous Titanium Oxide Composite

When a sample of microporous titanium oxide, giving an X-ray powder diffraction peak centered at $d=25$ Å, a BET surface area of 942 m²/g, and a cumulative pore volume of 0.673 cm³/g, was treated with excess bis(benzene) chromium with respect to Ti in dry benzene over several days under nitrogen, a new black material was formed. This new material is collected by suction filtration under nitrogen and washed with excess benzene until the filtrate is colorless. Figure 14 shows the XRD spectra of the material before and after treatment with bis(benzene) chromium. The broad reflection centered at $d=25$ Å in the product material demonstrates that this material retains its wormhole microstructure on reaction with the organometallic complex, although the reduction in intensity with respect to the starting material suggests some loss of long range order on reduction.

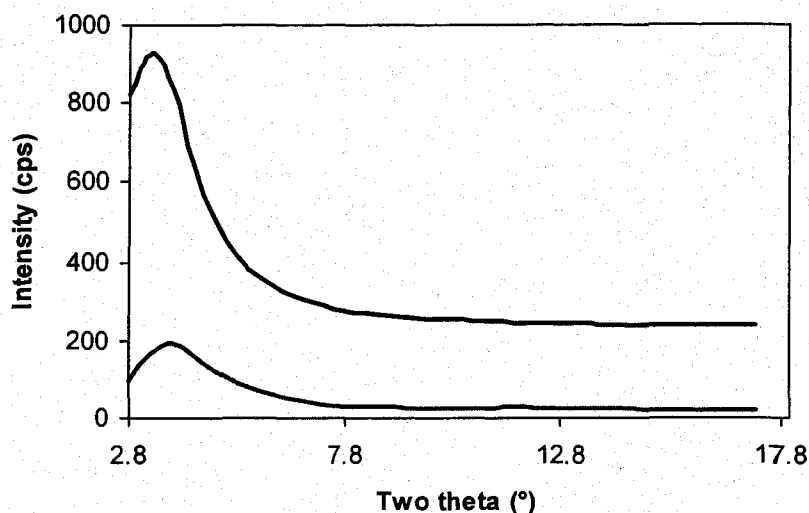


Figure 14. XRD of microporous titanium oxide before (upper) and after (lower) treatment with excess bis(benzene) chromium.

The nitrogen adsorption and desorption isotherms of the material before and after treatment with bis(benzene) chromium are shown in Figure 15. The BET surface area of the treated sample dropped to 404 m²/g, while the cumulative pore volume decreased to 0.192 cm³/g. These data are consistent with partial filling of the micropores by the encapsulated organometallic. The elemental analysis of this material showed an increase from 3.12% C and 1.36% H in the starting material to 13.56% C and 1.83% H in the product, with 5.4% Cr, as determined by inductively coupled plasma (ICP) spectrometry. The increasing percentage of C is consistent with retention of the structural integrity of the bis(benzene) Cr complex without loss of the benzene rings.

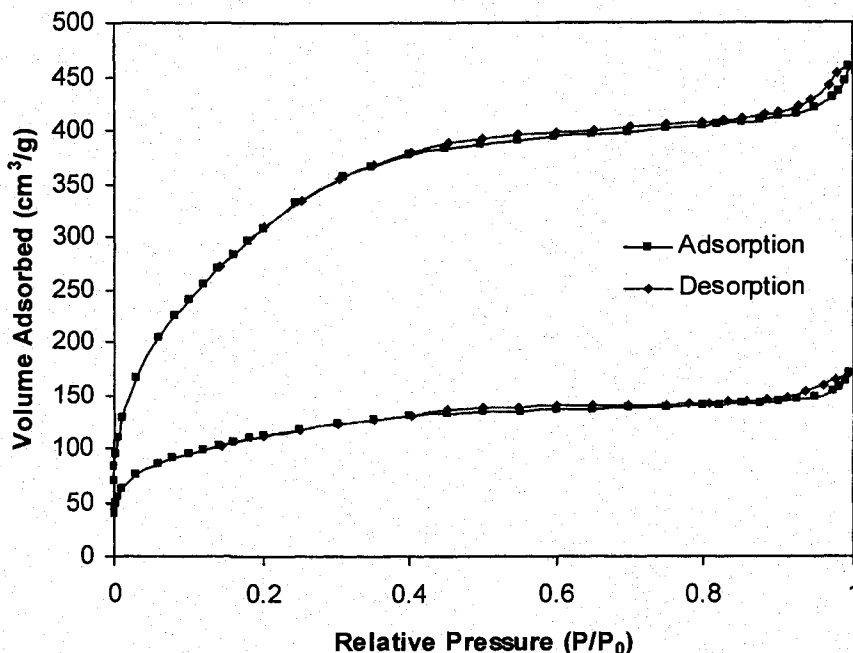


Figure 15. Nitrogen adsorption/desorption isotherms of microporous Ti oxide before (upper) and after (lower) treatment with bis(benzene) chromium.

3.2.2. X-ray Photoelectron Spectroscopy (XPS) Studies of Bis(benzene) Chromium Reduced Microporous Titanium Oxide Composite

To further probe into the nature of the surface species present, X-ray photoelectron spectroscopy (XPS) studies were conducted. This is an effective technique to elucidate the different species present in the sample and the degree of reduction of the transition metal oxide framework.²⁰³ Figure 16a shows the Ti 3p 1/2, 3/2 region of the XPS spectrum of the sample prepared with excess bis(benzene) chromium. The position of the Ti 3p 1/2 at 37.4 eV as compared to 37.9 eV in the unreduced material, is consistent with reduction of the Ti center by bis(benzene) chromium. This gradual shift to lower binding

energy on reduction of the framework has been commented on before.^{211, 212} These emissions are also broader than those in the starting material, as is the O 1s peak, providing further evidence for reduction of the Ti framework by bis(benzene) chromium. The Cr 2p 1/2, 3/2 region of the spectrum is shown in Figure 16b and shows a major peak at 577 and 586.8 eV, these emissions fall between those for the neutral $(C_6H_6)_2Cr$ at 575.7 and 584.8 eV and the cationic species $[(C_6H_6)_2Cr]^+$ with emissions at 577.7 and 586.7 eV.²¹⁵ These data are consistent with the existence of mixed-oxidation-state phases within the pores of the structure. The exact ratio between Cr^0/Cr^I is difficult to determine due to the low loading level of Cr and the sensitivity of the XPS technique.

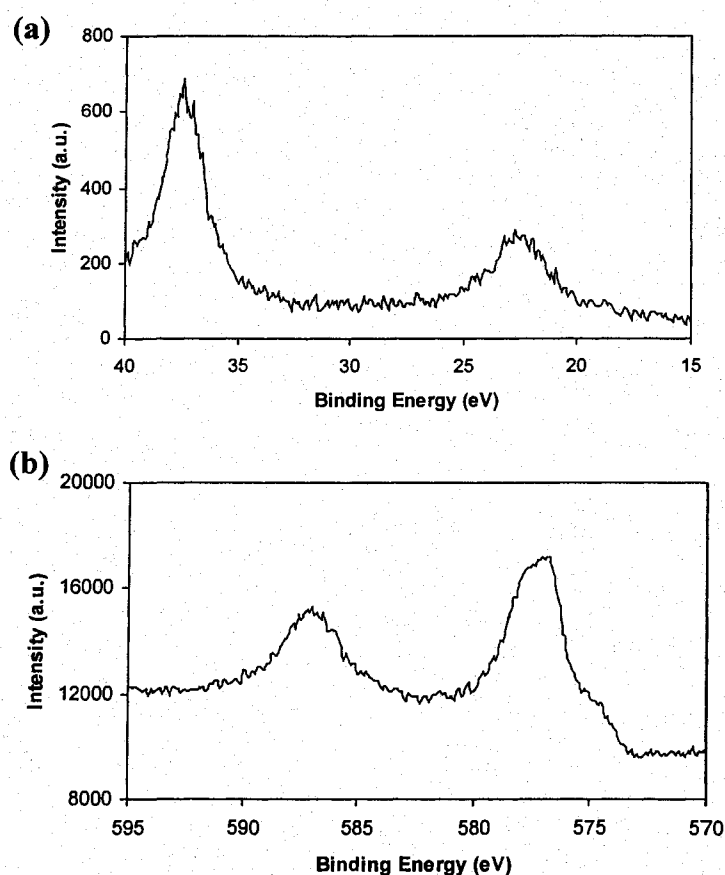


Figure 16. XPS spectra of microporous titanium oxide treated with excess bis(benzene) chromium showing the (a) Ti 3p 1/2, 3/2 regions, (b) Cr 2p 1/2, 3/2 regions.

3.2.3. Hydrogen Sorption Properties of Bis(benzene) Chromium Reduced Microporous Titanium Oxide Composite

Hydrogen pressure-composition isotherms were recorded at 77 K for pristine microporous Ti oxide (C6-Ti) and C6-Ti reduced with excess bis(benzene) chromium (Bisben Cr-Ti). Both H₂ storage and adsorption isotherms are shown in Figure 17. The adsorption values reflect the amount of hydrogen bound to the surface of the porous framework, whereas the storage is a measure of the total H₂ available as fuel in any system (i.e. the sum of the adsorption and the compressed gas in the pores). These results and all other hydrogen sorption results in this study are summarized in Table 5, complete with extrapolation to 100 atm. Previous results for excess bis(toluene) titanium reduced C6-Ti (BTTi C6-Ti), Li-naphthalene reduced (Li C6-Ti) and Na-naphthalene reduced (Na C6-Ti), as well as carbon AX-21, are also shown for comparison.²¹⁰ From Figure 17 we can see that all the storage isotherms gently rise sharply at low pressure and continue rise in a linear fashion from 10 atm onwards to 65 atm. Reversibility was evaluated by measuring the desorption branch down to near zero atm. The desorption branches follow the adsorption branches without significant hysteresis. The adsorption/desorption process is fast and thermodynamic equilibrium was reached within a few seconds, indicating a very low activation barrier for this processes. For the adsorption isotherms, the hydrogen capacity increases with increasing pressure until saturation is achieved, after which the hydrogen capacity begins to drop, a typical feature of supercritical adsorption.²⁰⁸ Extrapolation to 100 atm, a feasible pressure for a cryogenic storage tank, Bisben Cr-Ti yields a total storage capacity of 4.76 wt% and 31.61 kg/m³, compared with 5.36 wt%

and 29.37 kg/m³ for C6-Ti. The adsorption shows a decrease from 1.08 wt% and 5.918 kg/m³ in C6-Ti to 0.81 wt% and 5.378 kg/m³. The increased volumetric storage capacity is possibly due to the reduced Ti centers in the framework, which are better able to π -back bond to the H₂ ligands and thus increase the strength of binding to the surface.²¹⁰ However, compared to the BTTi C6-Ti, the improvement of performance on reduction is somewhat less dramatic. This can be explained by a number of factors. Bis(benzene) chromium is weaker reducing agent than bis(toluene) titanium, which can be verified from the XPS binding energy of Ti 3p 1/2 of Bisben Cr-Ti and BTTi C6-Ti.²⁰⁶ Also, whereas bis(toluene) titanium completely loses its ligands to leave a thin layer of low valence, low coordinate Ti species on the surface of the pore channels,²⁰⁶ bis(benzene) chromium leaves behind a mixture of the bis(benzene) chromium cation and the neutral species in the pores. Because of the coordinative saturation of these two Cr species, they are unable to contribute to hydrogen binding in the system. The decreased gravimetric storage capacity in Bisben Cr-Ti can be explained by the increased mass of the framework without a corresponding change of volume after treatment with the organometallic compound. From a gravimetric standpoint, it is clear that the increased framework will result in decreased gravimetric capacity. For some materials having very low density (such as activated carbon and MOFs materials), the high gravimetric density capacity can be obtained; however, the corresponding volumetric density will be low. For other materials, such as metal hydrides, the volumetric density can be very high because of the density of the material itself, but this comes with a tradeoff of a very low gravimetric density. These factors can thus account for the lower hydrogen sorption ability of Bisben Cr-Ti relative to that of BTTi C6-Ti.

Table 5. Hydrogen sorption capacities of pristine and reduced C6-Ti materials and AX-21.

Sample name	Surface area (m ² /g)	Apparent Density (g/ml)	Skeletal Density (g/ml)	Gravimetric Adsorption (wt %)	Gravimetric H ₂ storage (wt %) ^a	Volumetric Adsorption (kg/m ³)	Volumetric H ₂ storage (kg/m ³) ^a
C6-Ti	942	0.548	2.698	1.08	5.36	5.918	29.37
Li C6-Ti	499	0.556	2.508	0.71	5.63	3.948	31.30
Na C6-Ti	480	0.565	2.741	0.92	5.58	5.198	31.58
BTTi C6-Ti	208	0.819	2.835	1.14	4.94	9.337	40.46
AX-21	3225	0.328	2.103	4.19	11.96	13.75	39.23
Bisben Cr-Ti	404	0.664	2.793	0.81	4.76	5.378	31.61
Bisben V-Ti	248	0.711	2.846	0.74	4.70	5.261	33.42
Biscp Cr-Ti	461	0.635	2.632	1.01	4.80	6.413	30.49
Biscp V-Ti	513	0.612	2.510	0.93	4.95	5.692	30.30

^a Hydrogen storage measurement is at the temperature of 77 K and 65 atm extrapolated to 100 atm with goodness of fit (R^2)= 0.9963-0.9992.

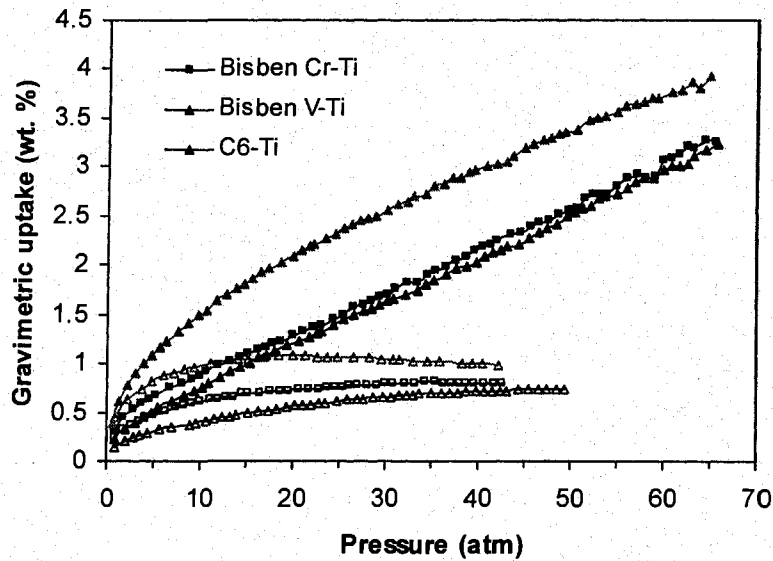


Figure 17. Gravimetric high-pressure H₂ isotherms for C6-Ti, Bisben Cr-Ti and Bisben V-Ti at 77 K. Filled markers represent storage capacity and open markers denote adsorption capacity.

The binding enthalpy of this material was calculated by a variant of Clausius-Clapyron equation²⁰⁹ from hydrogen adsorption data at 77 and 87 K (see Figure 18). Because this is complex solid with Ti d_{xy} , d_{xz} , d_{yz} t_{2g} binding sites at and below the surface of the pore channels, the enthalpies likely represent an average of many sites. The plot for this sample show an increase in ΔH with H_2 capacity, which is consistent with our previous results on reduced microporous titanias.²¹⁰ This highly unusual behavior may reflect a different mechanism of surface binding than simple physisorption, possibly involving a Kubas-type interaction. The maximum ΔH for Bisben Cr-Ti is 6.248 kJ/mol, somewhat lower than that for BTTi C6-Ti, reflecting the lower degree of surface reduction afforded by the weaker reducing agent.

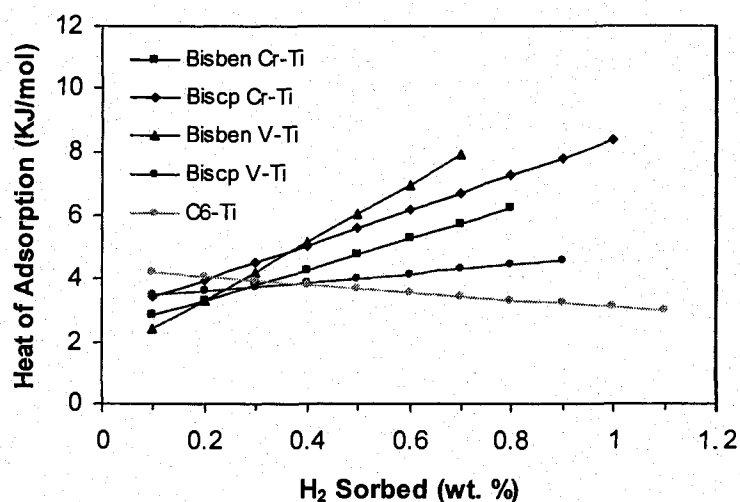


Figure 18. Enthalpies of H_2 adsorption for pristine and bis-arene and bis-cyclopentadienyl transition-metal-reduced microporous titanium oxides.

3.2.4. X-ray Powder Diffraction (XRD) Pattern, Nitrogen Adsorption Study and Elemental Analysis of Bis(benzene) Vanadium Reduced Microporous Titanium Oxide Composite

When C6-Ti was treated with excess bis(benzene) vanadium²¹⁴ in benzene over several days, a new black material was formed, collected by suction filtration, and dried in vacuo for 24 h to ensure complete removal of free solvent from the structure. Figure 19 shows the XRD peaks of the materials before and after treatment with bis(benzene) vanadium. The symmetric peak centered at 25 Å in the product demonstrates that this material fully retained its microstructure on intercalation of the organometallic compound.

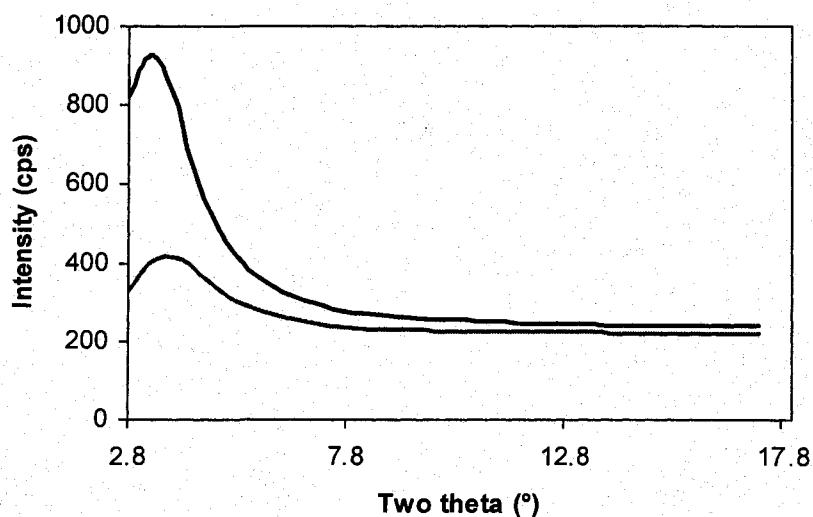


Figure 19. XRD of microporous titanium oxide before (upper) and after (lower) treatment with excess bis(benzene) vanadium.

Figure 20 shows the nitrogen adsorption and desorption isotherms of the materials from Figure 19. The BET surface area of the treated sample dropped to 243 m²/g while the

cumulative pore volume decreased to $0.143 \text{ cm}^3/\text{g}$. The retention of the XRD pattern and the same type of nitrogen adsorption/desorption isotherms with a decrease in cumulative pore volume and surface area as compared to the starting materials are all consistent with occlusion of the pores of the microstructure by the encapsulated organometallic compound. The elemental analysis of this new material showed an increase in carbon from 3.12% in the starting material to 3.72% with 3.51% V as determined by ICP spectrometry. The virtually unchanged C content in concert with the appearance of V indicates that the bis(benzene) vanadium loses its benzene ligands and deposits a small amount of an unsaturated vanadium species on the surface of the microstructure. This is similar to the action of bis(toluene) titanium, however the addition of Ti to the composite and concomitant decomposition of the organometallic is autocatalytic at $60 \text{ }^\circ\text{C}$ and continues until the pores of the microstructure are completely blocked by low-valent Ti.

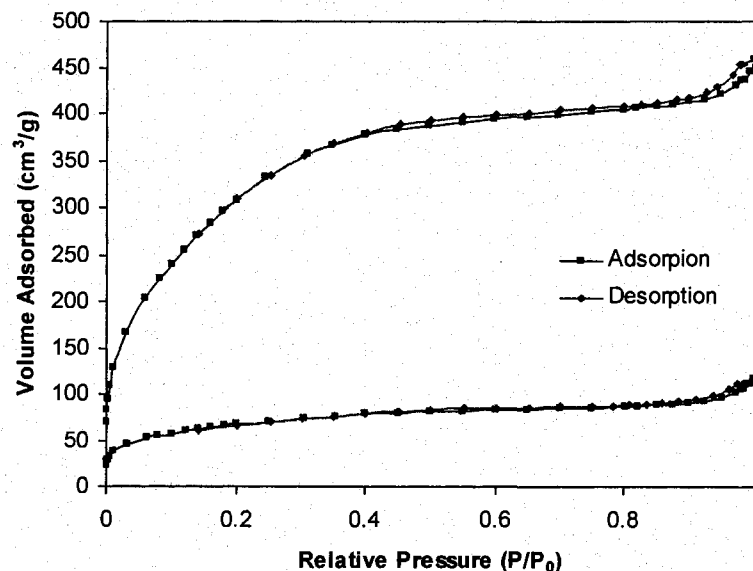


Figure 20. Nitrogen adsorption/desorption isotherms of microporous Ti oxide before (upper) and after (lower) treatment with bis(benzene) vanadium.

3.2.5. X-ray Photoelectron Spectroscopy (XPS) Studies of Bis(benzene) Vanadium Reduced Microporous Titanium Oxide Composite

XPS studies were conducted for this new composite. Figure 21a shows the Ti 3p region with the 1/2, 3/2 peaks in clear evidence. The position of the 3p 1/2 falls at 37.2 eV as compared to 37.4 eV in the materials reduced with excess bis(benzene) chromium and 37.9 eV in the unreduced material. This is fully consistent with reduction of the Ti center by bis(benzene) vanadium. In this case the emission at 37.2 eV demonstrates reduction of the framework to a level of about Ti 3.3⁺. These emissions are also much broader than those in the starting material and bis(benzene) chromium reduced material, providing further evidence for reduction of the Ti framework by bis(benzene) vanadium. Figure 21b shows the V 2p 3/2, 1/2 region, displaying two emissions at 515.3 and 523.3 eV, which can be assigned as V(II) species (515.6 and 523.2 eV).

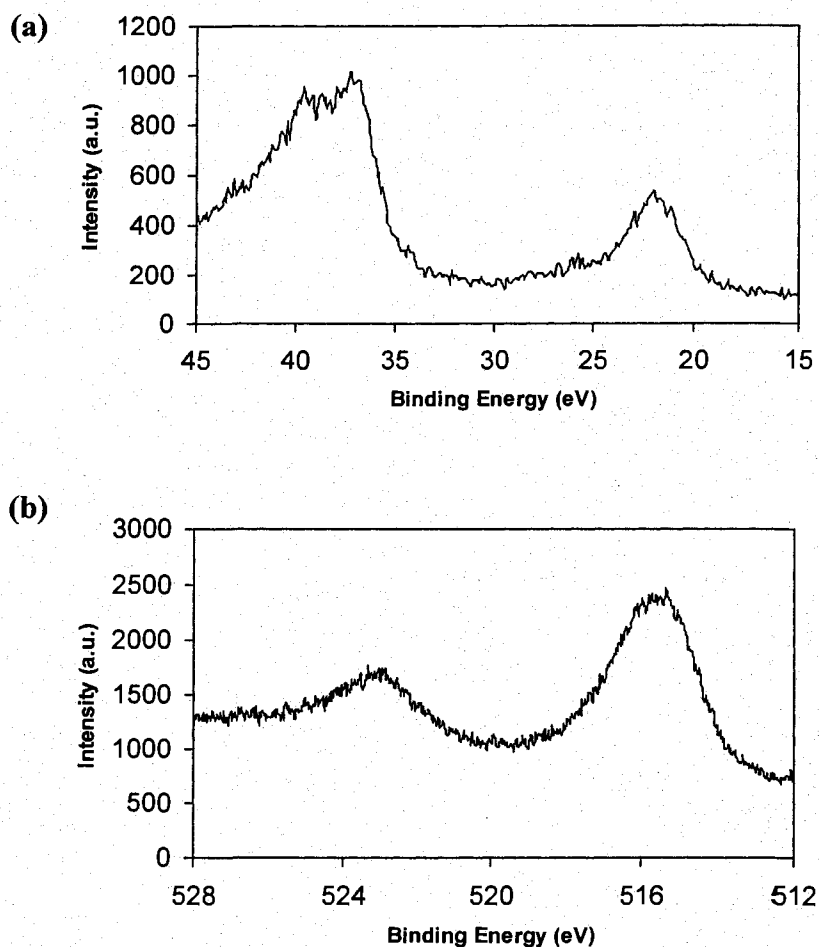


Figure 21. XPS spectra of microporous titanium oxide treated with excess bis(benzene) vanadium showing the (a) Ti 3p 1/2, 3/2 regions, (b) V 2p 1/2, 3/2 regions.

3.2.6. Hydrogen Sorption Properties of Bis(benzene) Vanadium Reduced Microporous Titanium Oxide Composite

Hydrogen pressure-composition isotherms at 77 K of both adsorption and storage for excess bis(benzene) vanadium reduced C6-Ti (Bisben V-Ti) is shown in Figure 17. This material yielded total storage values of 4.7 wt% and 33.42 kg/m³ in gravimetric and

volumetric capacities respectively. The overall increase in volumetric storage compared with Bisben Cr-Ti can be attributed to the stronger reducing ability of bis(benzene) vanadium than that of bis(benzene) chromium. Although the drop in gravimetric capacity is possibly due to the increased framework mass and lower surface area of Bisben V-Ti compared with Bisben Cr-Ti, many factors, including framework density, surface properties, and pore volume are expected to be at play. The gravimetric and volumetric adsorption data for this material were 0.74 wt% and 5.261 kg/m³, respectively. The binding enthalpy of this material as a function of surface coverage is shown in Figure 18. As with other reduced microporous Ti oxides in this study, the enthalpy increases with the H₂ capacity. The maximum ΔH for Bisben V-Ti is 7.885 kJ/mol.

3.2.7. X-ray Powder Diffraction (XRD) Pattern, Nitrogen Adsorption Study and Elemental Analysis of Bis(cyclopentadienyl) Chromium Reduced Microporous Titanium Oxide Composite

Treatment of C6-Ti with excess bis(cyclopentadienyl) Cr with respect to Ti in dry benzene over 2 days gave a new black material which was collected by suction filtration under nitrogen and washed with excess benzene until the filtrate is colorless, following by drying in vacuo at 10⁻³ Torr. Figure 22 shows the XRD spectra of the material before and after treatment with bis(cyclopentadienyl) Cr. The broad reflection centered at d=25 Å in the product material demonstrates that this material has fully retained its microstructure on the intercalation of organometallic complex.

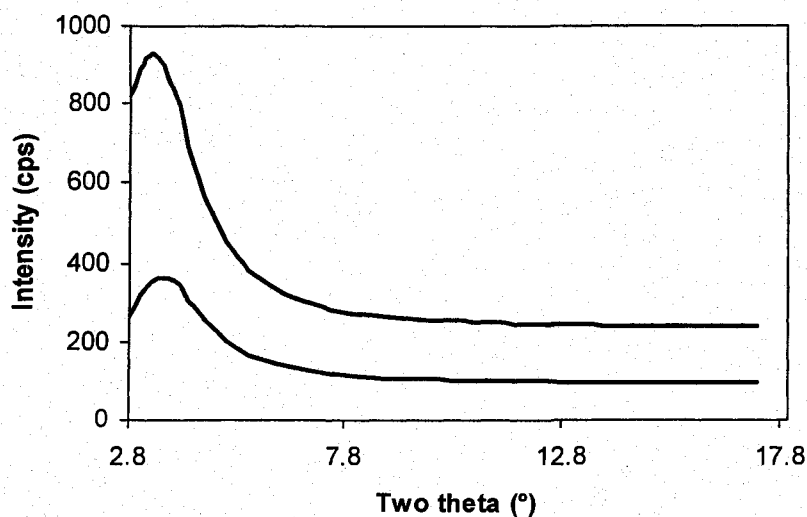


Figure 22. XRD of microporous titanium oxide before (upper) and after (lower) treatment with excess bis(cyclopentadienyl) chromium.

The nitrogen adsorption and desorption isotherms of the material before and after treatment with bis(cyclopentadienyl) chromium are shown in Figure 23. The BET surface area of the treated sample dropped to 461 m²/g, while the cumulative pore volume decreased to 0.299 cm³/g. The elemental analysis of this material showed an increase from 3.12% C and 1.36% H in the starting material to 13.68% C and 1.61% H in the product, with 5.81% Cr, as determined by ICP spectrometry. The increasing percentage of C is consistent with retention of the structural integrity of the organometallic without decomposition to chromium metal or chromium oxide.

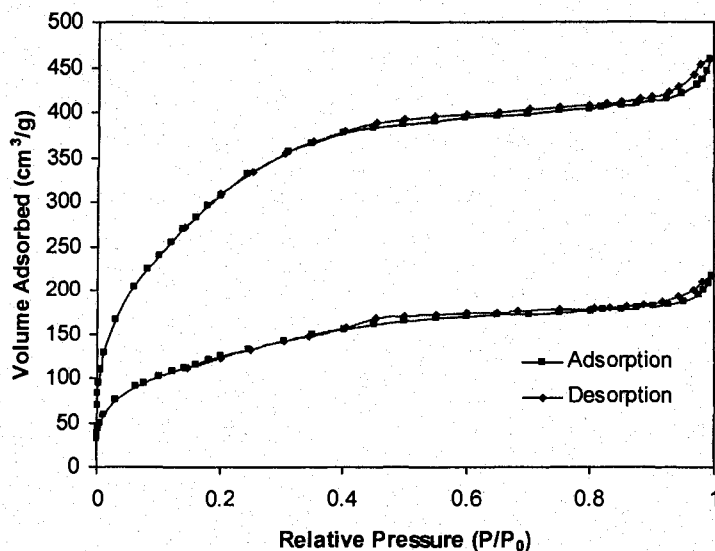


Figure 23. Nitrogen adsorption/desorption isotherms of microporous Ti oxide before (upper) and after (lower) treatment with bis(cyclopentadienyl) chromium.

3.2.8. X-ray Photoelectron Spectroscopy (XPS) Studies of Bis(cyclopentadienyl) Chromium Reduced Microporous Titanium Oxide Composite

The Ti 3p 3/2, 1/2 regions of the X-ray photoelectron spectrum (XPS) of the microporous composite are shown in the Figure 24a. This spectrum exhibits a peak at 37.0 eV for Ti 3p 1/2 region. This gradual shift to lower binding energy, as compared to 37.9 eV in the unreduced material, is fully consistent with reduction of the Ti center by bis(cyclopentadienyl) chromium. The Cr 2p 1/2, 3/2 regions of the XPS (Figure 24b) show emissions at 586.5 and 577.1 eV, respectively. These numbers fall between the neutral bis(cyclopentadienyl) Cr with peaks at 584.5 and 574.8 eV, a Cr (II) species having emissions at 585.5 and 575.7 eV and a higher oxidation state Cr (IV) species with

peaks at 587.1 and 577.4 eV, consistent with our previous results with the analogous Nb composites.²¹³

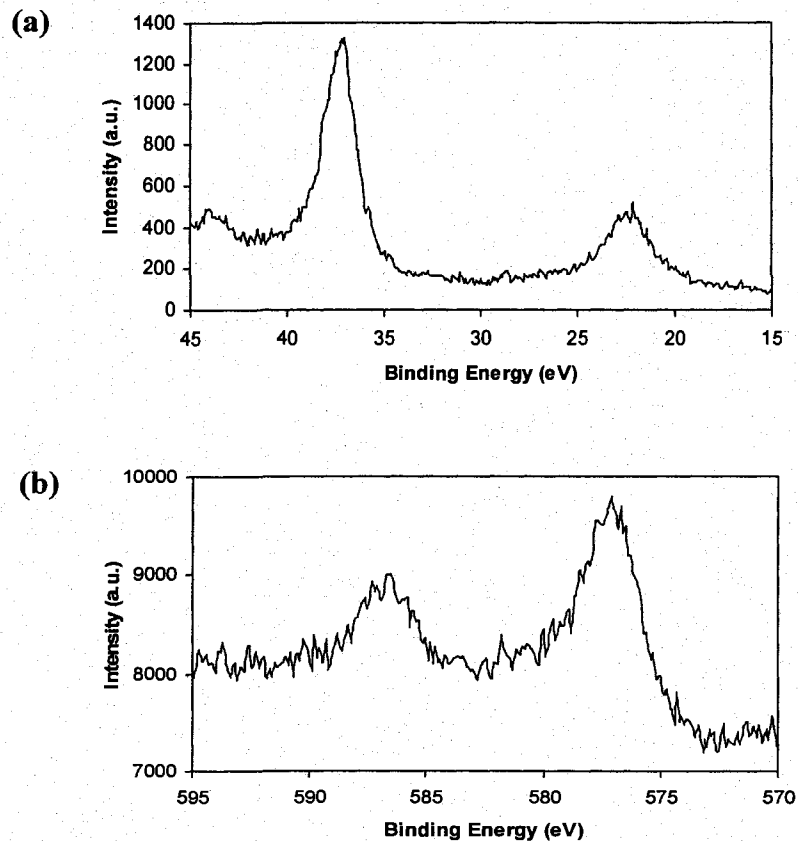


Figure 24. XPS spectra of microporous titanium oxide treated with excess bis(cyclopentadienyl) chromium showing the (a) Ti 3p 1/2, 3/2 regions, (b) Cr 2p 1/2, 3/2 regions.

3.2.9. Hydrogen Sorption Properties of Bis(cyclopentadienyl) Chromium Reduced Microporous Titanium Oxide Composite

The hydrogen storage and adsorption isotherms of this excess bis(cyclopentadienyl) chromium reduced C6-Ti (Biscp Cr-Ti) are recorded in Figure 25, together with C6-Ti.

From Figure 25 we can see the isotherms for this sample have the same trend with those of unreduced materials and the Ti and V bis(arene) transition metal reduced materials discussed above. The gravimetric and volumetric storage capacity for this sample is 4.80 wt% and 30.49 kg/m³, respectively. These results are similar to those recorded for Bisben Cr-Ti. However, Biscp Cr-Ti possesses a gravimetric adsorption of 1.01 wt% and a volumetric adsorption capacity of 6.413 kg/m³, which is higher than those of Bisben Cr-Ti. The reason for this could be the higher surface area as compared to that of Bisben Cr-Ti. As with Bisben Cr-Ti and Bisben V-Ti, an increase of binding enthalpy with surface coverage was observed for this sample (Figure 18), with a maximum ΔH of 8.353 kJ/mol.

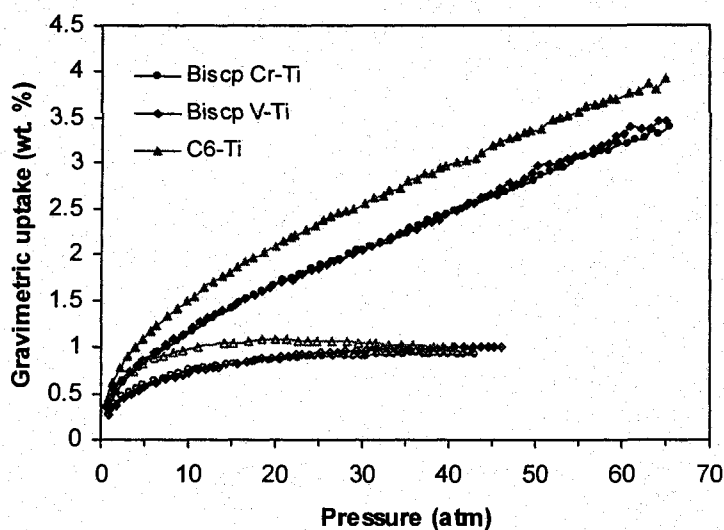


Figure 25. Gravimetric high-pressure H₂ isotherms for C6-Ti, Biscp Cr-Ti and Biscp V-Ti at 77 K. Filled markers represent storage capacity and open markers denote adsorption capacity.

3.2.10. X-ray Powder Diffraction (XRD) Pattern, Nitrogen Adsorption Study and Elemental Analysis of Bis(cyclopentadienyl) Vanadium Reduced Microporous Titanium Oxide Composite

When C6-Ti was treated with excess bis(cyclopentadienyl) V with respect to Ti in dry benzene over several days, a new black material was formed. This new material is collected by suction filtration under nitrogen and washed with excess benzene until the filtrate is colorless. Figure 26 shows the XRD spectra of the material before and after treatment with bis(cyclopentadienyl) V. The broad reflection centered at $d=25 \text{ \AA}$ in the product material demonstrates that this material has fully retained its microstructure on the intercalation of organometallic complex.

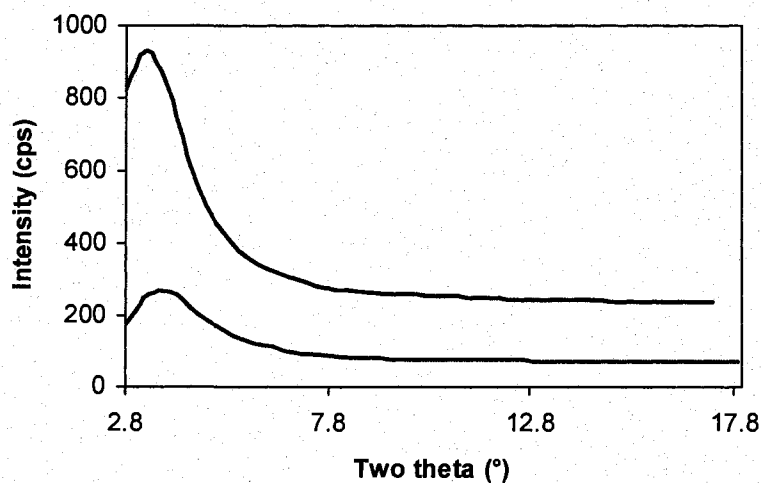


Figure 26. XRD of microporous titanium oxide before (upper) and after (lower) treatment with excess bis(cyclopentadienyl) vanadium.

The nitrogen adsorption and desorption isotherms of the material before and after treatment with bis(cyclopentadienyl) vanadium are shown in Figure 27. The BET surface

area of the treated sample dropped to 513 m²/g, while the cumulative pore volume decreased to 0.337 cm³/g. The elemental analysis of this new composite showed an increase in carbon from 3.12% and 1.36% H in the starting material to 11.26% C and 1.56% H with 3.53% V, as determined by ICP spectrometry. The increase in carbon is fully consistent with retention of the structure of the bis(cyclopentadienyl) complex without loss of the organic rings.

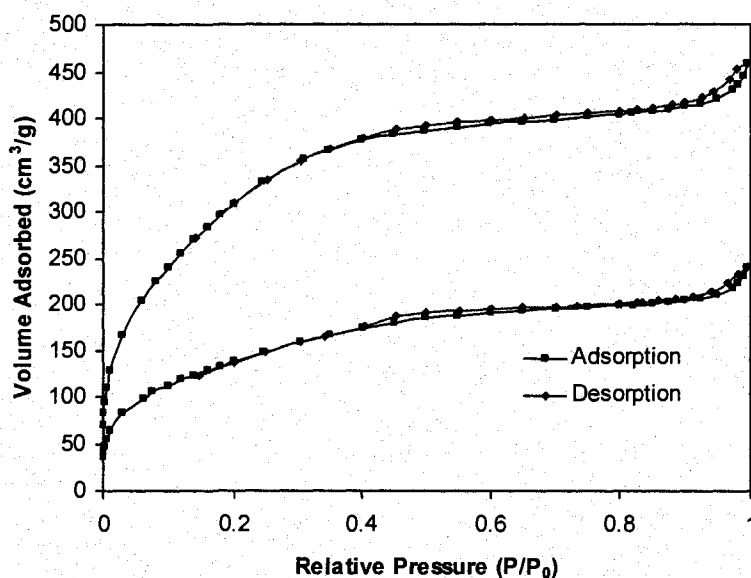


Figure 27. Nitrogen adsorption/desorption isotherms of microporous Ti oxide before (upper) and after (lower) treatment with bis(cyclopentadienyl) vanadium.

3.2.11. X-ray Photoelectron Spectroscopy (XPS) Studies of Bis(cyclopentadienyl) Vanadium Reduced Microporous Titanium Oxide Composite

Figure 28a shows the XPS Ti 3p regions, with the 3/2 and 1/2 emissions in clear evidence. The position of Ti 3p 1/2 emission is 37.5 eV is consistent with reduction of Ti framework as compared described above. The slightly higher position of Ti 3p 1/2

emission as compared to the analogous bis(benzene) vanadium composite confirmed that bis(cyclopentadienyl) vanadium is a less effective reducing agent than the bis(benzene) vanadium. The V 2p 3/2 and 1/2 regions of the XPS (Figure 28b) show emissions at 515.6 and 524.3 eV, respectively. This can be assigned a mixture of the neutral bis(cyclopentadienyl) V species (513.0 and 520.2 eV), a vanadium (IV) species (514.9 and 522.4 eV), and a vanadium (V) species (516.4 and 524.5 eV).^{213, 216}

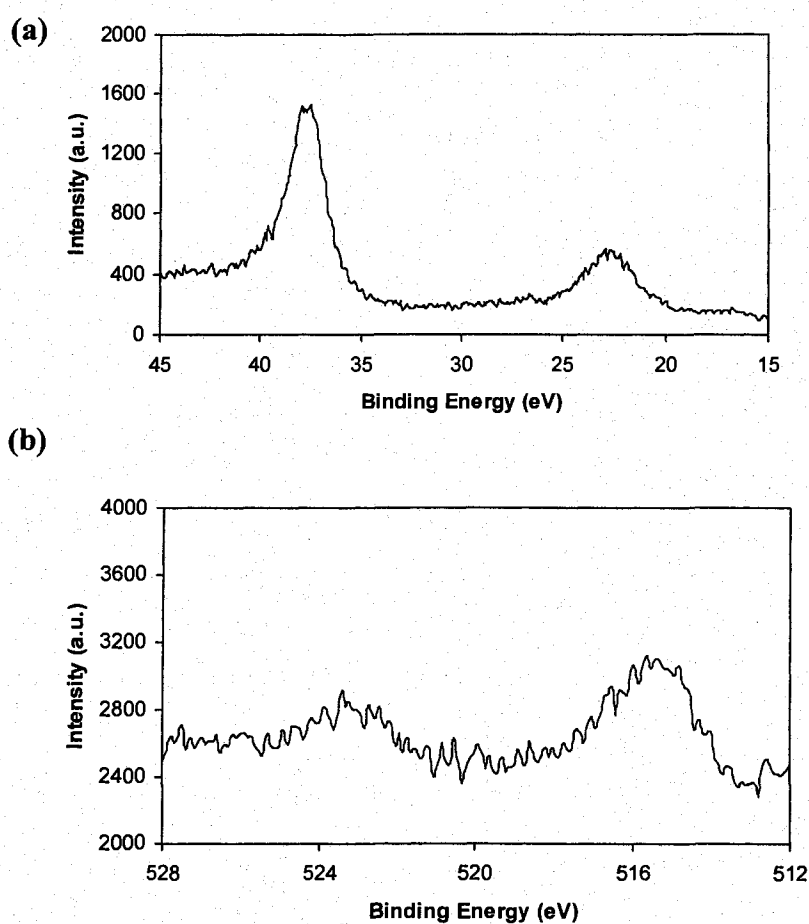


Figure 28. XPS spectra of microporous titanium oxide treated with excess bis(cyclopentadienyl) vanadium showing the (a) Ti 3p 1/2, 3/2 regions, (b) V 2p 1/2, 3/2 regions.

3.2.12. Hydrogen Sorption Properties of Bis(cyclopentadienyl) Vanadium Reduced Microporous Titanium Oxide Composite

Hydrogen storage and adsorption isotherms for this excess bis(cyclopentadienyl) vanadium reduced C6-Ti (Biscp V-Ti) were recorded at 77 K and are shown at Figure 25. A gravimetric storage capacity of 4.95wt% and volumetric storage capacity of 30.30 kg/m³ were obtained respectively. The highest surface area of Biscp V-Ti in all these reduced materials in this study can attribute to the highest gravimetric storage capacity of reduced materials in this study, whereas the smallest apparent and skeletal density combined with the less reduced framework can explain its lowest volumetric storage capacity. The adsorption data showed a gravimetric capacity of 0.93 wt% and a volumetric capacity of 5.692 kg/m³. The H₂ binding enthalpy of Biscp V-Ti was shown at Figure 18. The plot still showed an increase in ΔH with H₂ capacity, which is typical for all the reduced samples in this and our previous study.²¹⁰ The maximum ΔH of Biscp V-Ti was 4.574 kJ/mol, which is the lowest of all reduced materials in this study.

3.3 Discussion

The most surprising trend in this series of materials is the seemingly small dependence on surface area of the gravimetric and volumetric adsorption or storage values. In general, cryogenic hydrogen storage values depend almost exclusively on surface area and pore structure in porous carbons and MOFs. In these materials, greater surface area and lower skeletal density usually leads to higher gravimetric storage values, while lower

densities also lead to lower volumetric storage values. The fact that the best-performing material in our series has the lowest surface area (BTTi C6-Ti) clearly indicates that other factors are at play. Long *et al.* have demonstrated the effect of transition metal linker on the adsorption values, in particular an anomalous adsorption trend involving a possible Kubas-type interaction with a Mn center.¹⁴⁷ In our materials, the evidence suggests that surface reduction has a greater effect on the performance than surface area or pore size. There is also an unusual trend in enthalpies, which show an increase in binding strength as the surface coverage increases, which is consistent with our previous results.²¹⁰ This is the opposite of all other cryogenic hydrogen storage materials, which show a small decrease with increasing surface coverage. The reason of this has been commented in Chapter 2.

In terms of increased storage values, it is clear from our data that surface reduction leads to an increase in density, with a concomitant increase in volumetric storage capacity. The gravimetric capacities are relatively unaffected, because any increase in hydrogen binding is offset by an increase in density. A plot of XPS Ti 3p 1/2 binding energy versus hydrogen volumetric storage of all the C6-Ti samples in this study and our previous study²¹⁰ is shown in Figure 29. This XPS emission has been used in previous work by our group to establish the oxidation state of the Ti centers in meso- and microporous Ti oxides. This figure shows a roughly linear, albeit *empirical*, relationship between the volumetric storage capacity and the degree of reduction of the micro-framework. Ascribing a precise meaning to this trend is difficult due to the complex interplay of often offsetting parameters including a) different skeletal densities which increase according to amount of reductant, b) different surface areas c) different void

space volumes which change with surface area as well as volume occupied by the counterion (ie Na, Li, (benzene)₂ chromium, etc.) and its respective solvation sphere, d) different binding capacities as determined by degree of surface reduction of these materials, e) different degrees of accessible coordinative unsaturation at the surface Ti or dopant sites, and f) different capacities of Ti, V, or Cr to back donate to H₂ depending on reduction level and Z_{eff} . Calculations by Zhao *et al.* indicate that zero-valent Sc should be the most effective at achieving an optimal binding interaction, with a trend towards decreased efficiency going to the right of the periodic table.²⁰⁰ There is also the fact that some of the counterions (i.e., Na) are unable to bind hydrogen, but that the unsaturated Ti or V phase left by bis(toluene) titanium or bis(benzene) vanadium is able to coordinate hydrogen. On top of this, the enthalpies quoted in this work are clearly an average of many sites on the surface and beneath the surface of the walls of the amorphous microstructure (the walls are typically 15-20 Å thick and are probably easily penetrated by the small hydrogen molecule). These facts aside, it is still clear that surface reduction has a dramatic effect on the volumetric storage capacities of these materials, even with the offsetting decrease in surface areas. Following the trend in Figure 29, it seems that even higher volumetric storage capacities are possible with more effective reducing agents which are better able to leave a low-valence surface, with a maximum degree of available coordinative unsaturation and lowest possible skeletal density.

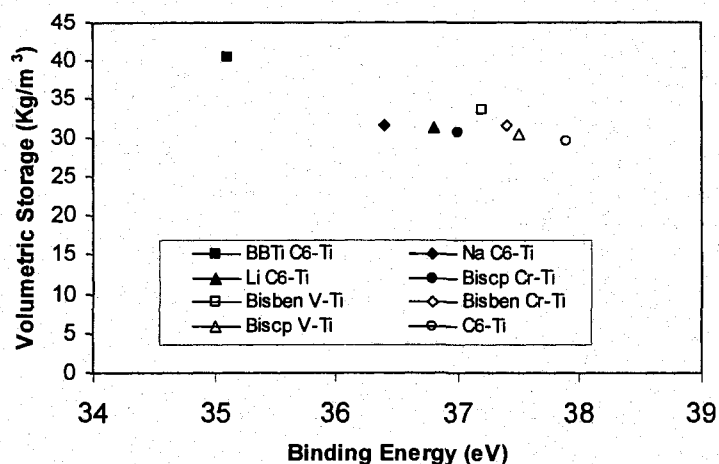


Figure 29. Plot of XPS Ti 3p 1/2 binding energy vs. the hydrogen volumetric storage capacity for all the C6-Ti samples.

3.4 Conclusion

In summary, in this study, a series of bis(benzene) and bis(cyclopentadienyl) transition metal reduced microporous titanium oxide composite materials were synthesized and characterized by nitrogen adsorption, XRD, XPS and elemental analysis. The hydrogen sorption study at 77 K found that the gravimetric sorption capacities of these new reduced composites decreased compared that of unreduced pristine samples while the overall volumetric storage capacity increased. The unusual behavior of hydrogen binding enthalpies increasing with hydrogen sorption capacity were found for all the reduced samples, which indicating a different sorption mechanism than simple physisorption possibly involving Kubas-type interaction. The maximum hydrogen binding enthalpies for these new composites ranged from 4.57 to 8.35 kJ/mol, but still fell short of the 20 kJ/mol value proposed for porous materials to function effectively at ambient

temperature. Further investigation is needed to find the suitable reducing agents that can lead to greater storage capacity to meet goals set by US DOE and to achieve more precise control of the enthalpies to operate at more practical temperatures.

Chapter 4. Hydrogen Storage in Mesoporous Titanium Oxide Alkali Fullerides Composites

In Chapter 2 and 3, it was shown that various chemically-reduced microporous Ti oxides are more effective hydrogen storage materials than the parent unreduced material.^{210, 217} For example, microporous Ti oxide treated with bis(toluene) titanium, demonstrated a gravimetric storage capacity of 4.94 wt % with a volumetric storage capacity of over 40 kg/m³ at 77 K and 100 atm, and microporous Ti oxide reduced with Na or Li showed the gravimetric storage capacities of 5.58 wt% and 5.63 wt%, respectively, with volumetric storage values of 31.58 kg/m³ and 31.30 kg/m³,²¹⁰ compared with 5.36 wt% and 29.37 kg/m³ in gravimetric and volumetric storage density, respectively, for the unreduced Ti oxide material. For all reduced materials, reduction of the surface leads to a dramatic change in surface properties, resulting in higher ΔH of adsorption as well as the first example of enthalpies which increase on hydrogen loading, suggesting a different mechanism than simple physisorption.

Preliminary work conducted by our group in collaboration with General Motors¹⁹⁶ suggested that mesoporous Ti oxides reduced with alkali fullerides may possess a maximum gravimetric uptake of 8 wt% at 200°C and 100 atm. This family of composites is related to mesoporous Ta and Nb oxide alkali fulleride intercalates previously studied by our group.²¹⁸⁻²²⁴ These materials possess reduced transition metal oxide walls and 1-d chains of alkali fullerides filling the porous channels. They can also be readily tuned by addition of more alkali metal reductant, sometimes resulting in dramatically different conductivity properties. For these alkali fullerides Ti oxide composites, we reasoned that

the reduced fulleride units may act as additional sites for cryogenic hydrogen binding in a mesoporous Ti oxide framework, while also creating microporous cavities within the mesoporous gallery, possibly enhancing absorption of hydrogen through capillary effects. The pseudo-graphitic nature of the C_{60} surface is directly analogous to the walls of many carbon-based hydrogen storage materials, and could thus provide additional carbon-based hydrogen binding sites within the mesoporous channels, which would otherwise be filled with compressed gas. In order to more fully explore the hydrogen storage properties of these new composites, we synthesized a series of Na and Li fulleride impregnated mesoporous titanium oxide composites and screened them at a variety of temperatures and pressures.

4.1. Experimental Section

4.1.1. Materials and Equipment

All chemicals unless otherwise stated were obtained from Aldrich. All other materials and equipment unless otherwise stated here were the same as those shown in Chapter 2 and 3. Fullerene was obtained from Alfa. The Raman spectra were recorded on a Renishaw Ramascope using a Renishaw 514 nm Diode Laser System.

All elemental analysis data (conducted under an inert atmosphere) were obtained from Galbraith Laboratories, Knoxville, TN.

4.1.2. Synthesis

Synthesis of Na Fulleride Composites: To a suspension of the trimethylsilylated sample of mesoporous titanium oxide in dry THF was added excess Na_3C_{60} (synthesized by heating C_{60} and Na together in a sealed tube at 200-400 °C and characterized by XRD), as calculated on the basis of 38% Ti determined from the elemental analysis data. The mesoporous Ti solid immediately changed from a light tan color to a deep gray-black. After one week and additional stirring to ensure complete absorption of the fulleride, the reduced material was collected by suction filtration and washed several times with THF. Once synthesized, the material was dried in vacuo at 1×10^{-3} Torr on a Schlenk line until all condensable volatiles had been removed. This procedure is normally sufficient to remove any solvent molecules from the fulleride phase. Further reduction of this material was accomplished by addition of a predetermined quantity (calculated on the basis of the percentage of C_{60} in the material) of a stock solution of sodium naphthalene in THF to a stirred solution of the composite in THF. After stirring overnight, the material was collected by suction filtration and washed several times with benzene until the washings were colorless. The material was then dried in vacuo at 1×10^{-3} Torr on a Schlenk line until all condensable volatiles had been removed. All materials were characterized by XRD, nitrogen adsorption and desorption, Raman spectroscopy and elemental analysis to ensure sample quality before proceeding with hydrogen sorption measurement.

Synthesis of Li Fulleride Composite: Because of the intractable nature of Li fullerides, the mesoporous precursors were first reduced by Li naphthalene and then impregnated with pure C_{60} . This route was used previously by our group to synthesize

mesoporous Ta oxide Li fulleride composites.²¹⁸ To a benzene suspension of trimethylsilylated sample of mesoporous titanium oxide previously reduced with 1.0 molar equiv. of lithium naphthalene with respect to Ti was added excess C₆₀. After several days of stirring to ensure complete absorption of the fullerene, the material was collected by suction filtration and washed several times with benzene. The material was dried in vacuo at 1×10^{-3} Torr on a Schlenk line until all condensable volatiles had been removed. All materials were characterized by XRD, nitrogen adsorption and desorption, Raman spectroscopy and elemental analysis to ensure sample quality before proceeding with hydrogen sorption measurement. This route has the advantage that materials of different Li and C₆₀ ratios can readily be made by varying the quantities of these two dopants. In previous work we found that materials treated with lower levels of Li were less effective at reducing C₆₀ and therefore led to lower levels of fulleride intercalation, because the intercalation of C₆₀ is a process driven by electron transfer.^{218, 219}

4.2. Results

4.2.1. X-ray Powder Diffraction (XRD) Pattern, Nitrogen Adsorption Study, Raman Spectroscopy and Elemental Analysis of Na Fulleride Composites

A trimethylsilylated sample of mesoporous titanium oxide having a Barret-Joyner-Halenda (BJH) pore size of 21 Å, a BET surface area of 465 m²/g, and an XRD peak centered at $d = 30$ Å was treated with excess Na₃C₆₀ in THF over 1 week until maximum absorption is achieved. The new black sample (Na₃C₆₀ Ti) exhibited a strong XRD peak centered at $d = 30$ Å (Figure 30a), virtually the same as that obtained from the starting

material. There were no other peaks at higher angles, suggesting that there is no long-range order in the fulleride phase of the material, as observed for other 1-d fulleride composites studied by our group.²¹⁸⁻²²⁴ The BET surface area of this new material dropped from 465 to 116 m²/g (Figure 31a), while the BJH pore size fell from 21 to 20 Å.

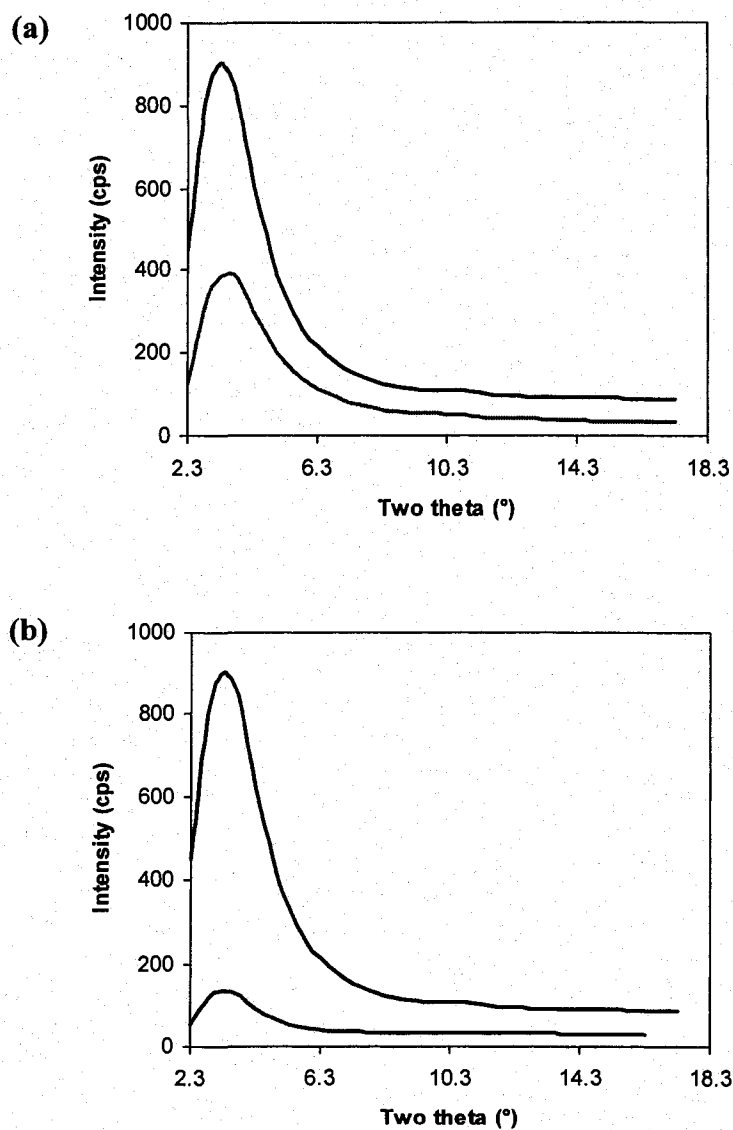


Figure 30. (a) XRD of mesoporous titanium oxide before (upper) and after (lower) treatment with excess Na₃C₆₀, (b) XRD of mesoporous titanium oxide before (upper) and after (lower) intercalated with excess Na₃C₆₀ and further reduction by 4 eqv. of Na - naphthalene.

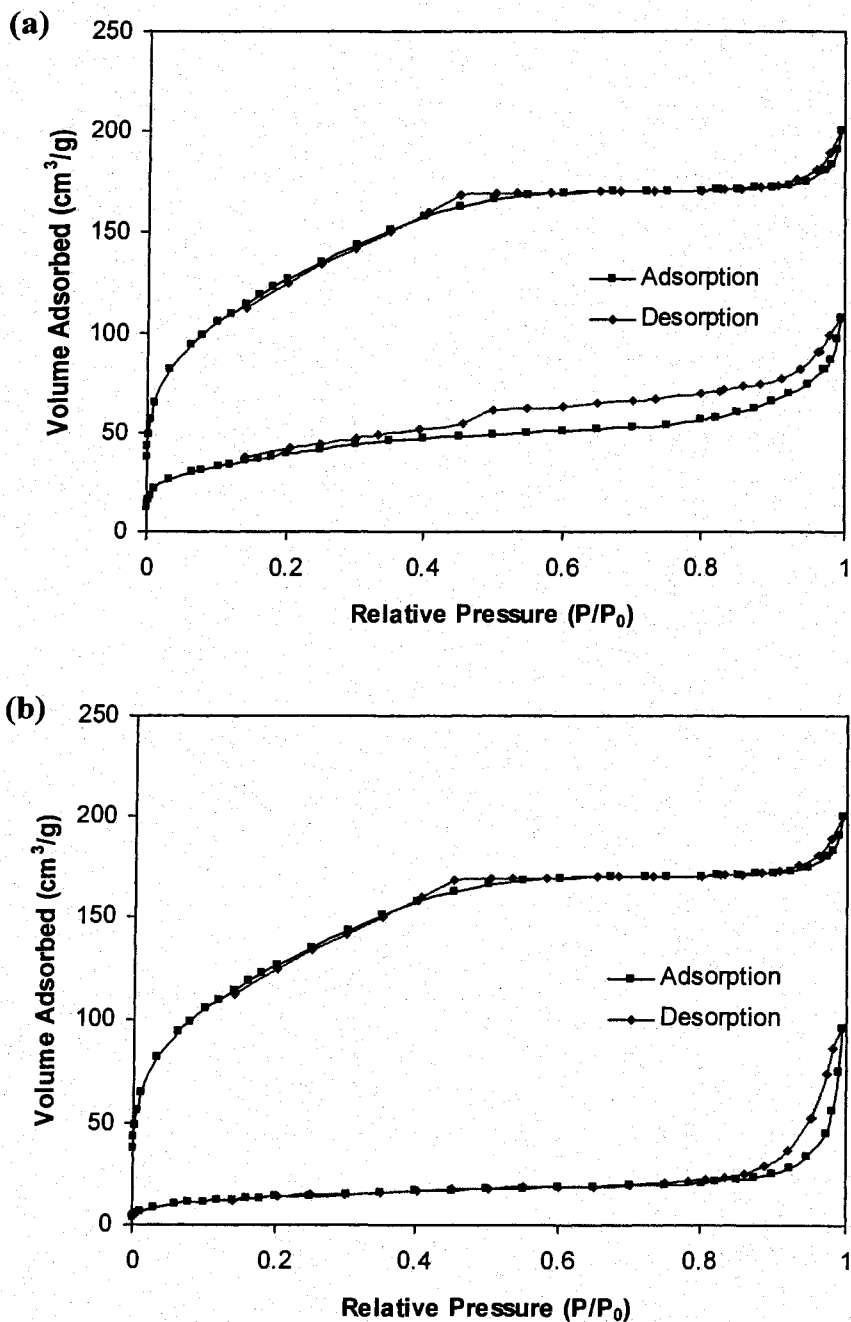


Figure 31. (a) Nitrogen adsorption/desorption isotherms of mesoporous titanium oxide before (upper) and after (lower) treatment with excess Na_3C_{60} and (b) Nitrogen adsorption/desorption isotherms of mesoporous titanium oxide before (upper) and after (lower) intercalated with excess Na_3C_{60} and further reduction by 4 eqv. of Na - naphthalene.

The cumulative desorption pore volume of this sample also showed a decrease to 0.152 cm³/g from 0.268 cm³/g in the starting material. These data are consistent with adsorption of a large amount of the fulleride salts into the mesopores of the material. Raman spectroscopy (Figure 32a) conducted on this new composite showed an A_g band at 1462 cm⁻¹, consistent with a C₆₀ oxidation state of 0.5⁻. It is well known that the A_g mode of pure C₆₀ was 1464 cm⁻¹ and for fulleride salts of the type A_nC₆₀ (A=K, Rb, Cs), the A_g mode shifts roughly 6 cm⁻¹ for every increment in the value of n.²²⁵ Elemental analysis (Table 6) gave values of 48.63% C and 4.57% Na with a Na: C₆₀ ratio of 2.94:1.0. In order to test the effect of further reduction on the hydrogen storage performance of this material, the parent composite was treated with 4 eqv. of Na-naphthalene with respect to C₆₀ (calculated on the basis of the elemental analysis results with a assumption that all the C in this material in excess of the residual 3.12% (see Table 6) was due to the absorbed fulleride). This provided a new blown black sample (Na-Na₃C₆₀ Ti) with an X-ray powder diffraction peak centered at d=30 Å (Figure 30b), a BJH pore size of 19 Å, a BET surface area of only 50 m²/g (Figure 31b), and a cumulative pore volume of 0.147 cm³/g. The Raman spectrum (Figure 32b) of this new composite showed an A_g band at 1444 cm⁻¹, which indicates a fulleride oxidation state of 3.5⁻. Elemental analysis (Table 6) gave values of 45.45% C and 8.45% Na, the corresponding Na: C₆₀ ratio was 6.25:1. The lack of substantial fulleride leaching from this material with Na-naphthalene reduction was observed for other sodium fulleride materials studied by our group and attributed to the possible formation of a polymeric fulleride chain.²²³

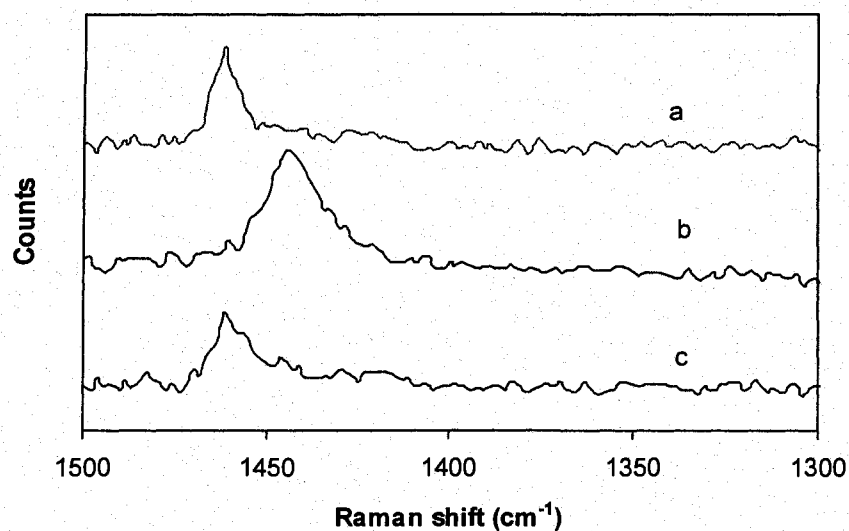


Figure 32. Raman spectra of (a) Na_3C_{60} Ti, (b) $\text{Na-Na}_3\text{C}_{60}$ Ti and (c) Li-C_{60} Ti.

Table 6. Elemental analysis values for samples of mesoporous titanium oxides before and after intercalation with alkali fullerides.

Sample	Carbon%	Sodium%	Lithium%	Molar ratio ($\text{C}_{60} : \text{Na}$)	Molar ratio ($\text{C}_{60} : \text{Li}$)
C12-Ti	3.12	NA	NA	NA	NA
Na_3C_{60} Ti	48.63	4.57	NA	1:2.94	NA
$\text{Na-Na}_3\text{C}_{60}$ Ti	45.45	8.45	NA	1:6.25	NA
Li-C_{60} Ti	38.78	NA	2.77	NA	1:8.06

4.2.2. Hydrogen Sorption Properties of Na Fulleride Composites

Hydrogen pressure-composition isotherms were recorded at 77 K for the pristine material synthesized with dodecylamine (C12-Ti), C12-Ti reduced with excess Na_3C_{60} (Na_3C_{60} Ti) and Na_3C_{60} Ti further reduced with 4 eqv. of Na-naphthalene with respect to

the C_{60} in the material (Na- Na_3C_{60} Ti). Both H_2 storage and adsorption isotherms are illustrated in Figure 33a.

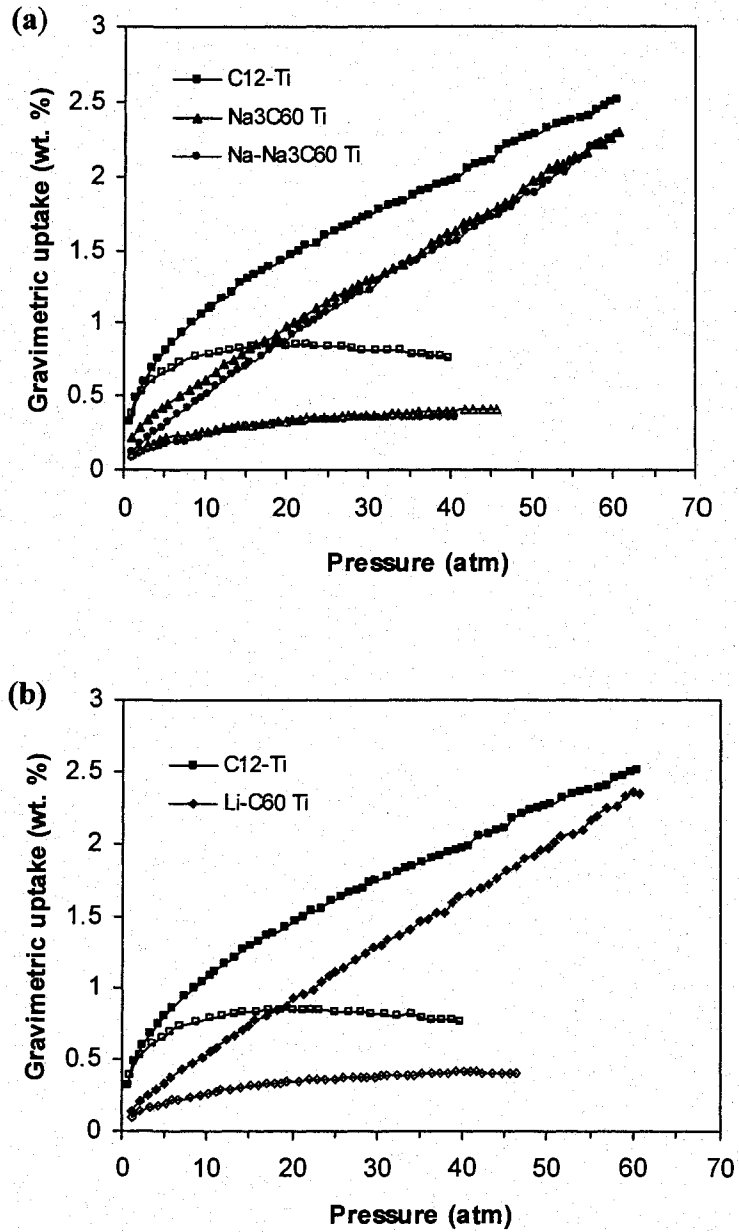


Figure 33. High-pressure H_2 isotherms for (a) C12-Ti, Na_3C_{60} Ti and Na- Na_3C_{60} Ti and (b) C12-Ti and Li- C_{60} Ti at 77 K in gravimetric uptake. Filled markers represent storage capacity and open markers denote adsorption capacity.

All the hydrogen sorption results in this study at cryogenic temperature are summarized in Table 7, complete with extrapolation to 100 atm, a plausible pressure for on-board operating conditions. Results for Li (Li C12-Ti) and Na (Na C12-Ti) reduced C12-Ti materials are also included for comparison. The adsorption values (commonly referred to as excess storage) reflect the amount of hydrogen bound to the surface of the porous framework, while total storage is the sum of the adsorption and the compressed hydrogen gas in the pores. From Figure 33a, we can see that all the storage isotherms rise sharply at low pressure and continue rise in a linear fashion from 10 atm onwards to 60 atm. Reversibility was evaluated by measuring the desorption branch down to near zero atm. The desorption branches nearly followed the adsorption branches without significant hysteresis. The adsorption/desorption process was very fast and thermodynamic equilibrium was reached within a few seconds, indicating a very low activation barrier of these processes. For the adsorption isotherms, the capacity increases with increasing pressure until saturation is reached after which a further increase in pressure led to a drop in the capacity. This feature is characteristic of excess storage isotherms,²⁰⁸ which measure the amount of gas adsorbed in excess of the bulk gas which would normally occupy the dead volume of the adsorbent at that temperature and pressure. The maximum occurs when the bulk density increases at a higher rate than the adsorbed density. Extrapolation to 100 atm yields a total storage capacity of 3.58 wt% and 26.57 kg/m³ for Na₃C₆₀ Ti, 3.61 wt% and 26.54 kg/m³ for Na-Na₃C₆₀ Ti, 3.51 wt% and 25.48 kg/m³ for C12-Ti, and 3.82 wt% and 28.19 kg/m³ for Na C12-Ti. The adsorption values were 0.40 wt%, 0.36 wt%, 0.85 wt%, and 0.80 wt% for Na₃C₆₀, Na-Na₃C₆₀, C12-Ti and Na C12-Ti, respectively. Intercalation with Na₃C₆₀, even when followed by further reduction by Na,

clearly has little effect on the volumetric storage, while reduction with Na only provides a more substantial increase in this value. The gravimetric storage values for these materials range from 3.51 wt% to 3.82 wt%, again with the material reduced only by Na displaying the highest value. The adsorption values drop by 0.45 wt% on intercalation of fulleride, but only 0.05 wt% on reduction by Na only. The apparent densities of the materials all fall between 7.24 g/ml and 7.42 g/ml with no clear trend, while the skeletal densities clearly drop on fulleride inclusion by ca. 0.5 g/ml, which is expected on the basis of an averaging out of the densities of amorphous Ti oxide and carbon. From our previous reports, we found that the introduction of new sites and reduced framework of the porous structure are beneficial to hydrogen storage.^{210, 217} On the other hand, intercalation reactions often cause a loss of surface areas and pore volume, which is harmful to hydrogen uptake. The observed hydrogen storage results are determined by both factors. In this case, the reduction of the framework and concomitant inclusion of new sites on the fulleride surface can not compensate the loss of the hydrogen uptake from the decreased surface area and pore volume, so there is no obvious improvement in the overall performance. It was hoped that addition of fulleride would create a vast internal surface on the free fulleride sites, which would further enhance binding of hydrogen. Based on the decreased hydrogen storage capacity for the Na fulleride reduced composite compared with that of fulleride-free Na reduced counterpart, there is a possibility that the inclusion of fulleride units may block access to the active Ti binding sites. This assumption can be further proved by the apparent decrease in adsorption capacity for the Na fulleride reduced composites compared with the unreduced and Na reduced samples, since the amount of the adsorption is more dependent on the binding sites available in the

materials than is the overall storage capacity. From Table 7, we can see that the adsorption values of 0.85 wt% and 6.154 kg/m³ in C12-Ti and 0.80 wt% and 5.904 kg/m³ in Na C12-Ti, compared with 0.40 wt% and 2.968 kg/m³ in Na₃C₆₀ Ti and 0.36 wt% and 2.646 kg/m³ in Na-Na₃C₆₀ Ti.

Table 7. Hydrogen sorption capacities of pristine C12-Ti and corresponding reduced materials at 77 K.

Sample name	Surface area (m ² /g)	Apparent Density (g/ml)	Skeletal Density (g/ml)	Gravimetric Adsorption (wt %)	Gravimetric H ₂ storage at 100atm (wt %) ^a	Volumetric Adsorption (kg/m ³)	Volumetric H ₂ storage at 100atm (kg/m ³) ^a
C12-Ti	531	0.724	2.678	0.85	3.51	6.154	25.48
Li-C ₆₀ Ti	143	0.731	2.235	0.41	3.74	2.997	27.35
Na ₃ C ₆₀ Ti	116	0.742	2.130	0.40	3.58	2.968	26.57
Na-Na ₃ C ₆₀ Ti	50	0.735	2.055	0.36	3.61	2.646	26.54
Li C12-Ti	313	0.726	2.671	0.69	3.87	5.009	28.10
Na C12-Ti	299	0.738	2.714	0.80	3.82	5.904	28.19

^a Hydrogen measurement is at the temperature of 77 K and 60 atm extrapolated to 100 atm with goodness of fit (R²)= 0.9954~0.9992.

In order to replicate the initial experiments with General Motor, the hydrogen adsorption and storage capacities of these new fulleride composites were also conducted at both room temperature and 200°C. At elevated temperatures adsorption in this system would likely proceed chiefly via formation of hydrides, rather than by physisorption. Figure 34a and 34b showed the gravimetric storage uptake for all fulleride composites in this study at room temperature and 200°C, respectively. The results are summarized at Table 8, also complete with extrapolation to 100 atm for comparison. At room temperature, a maximum gravimetric adsorption and storage capacity of 0.11 wt% and 0.99 wt% were achieved for Na₃C₆₀ Ti, respectively. Whereas at 200°C, both of these

numbers were decreased to 0.06 wt% for C12-Ti and 0.62 wt% for Na₃C₆₀ Ti, respectively. These results indicate that these materials work less efficiently at higher temperature and that the reversible formation of hydrides is not favorable.

The binding enthalpies of both unreduced and fulleride reduced materials were calculated by a variant of Clausius-Clapyron equation²⁰⁹ from hydrogen adsorption data at 77 and 87 K. The results are shown in Figure 35. The plot for Na₃C₆₀ Ti and Na-Na₃C₆₀ Ti show an increase in ΔH with H₂ capacity, which is consistent with our previous results involving reduced microporous Ti oxide materials.^{210, 217} The maximum ΔH for Na₃C₆₀ Ti and Na-Na₃C₆₀ Ti are 2.74 and 6.55 kJ/mol, respectively, compared to 5.42 kJ/mol for Na C12-Ti. This follows a trend in increasing reduction of the Ti oxide framework, demonstrating once again the positive effect of reduction on binding enthalpies in this system.

Table 8. Hydrogen sorption capacities of pristine and corresponding reduced C12-Ti materials at RT and 200°C.

Sample	Gravimetric Adsorption at RT (wt %)	Gravimetric Adsorption at 200°C (wt %)	Gravimetric Storage at RT and 100 atm (wt %) ^a	Gravimetric Storage at 200°C and 100 atm (wt %) ^a
C12-Ti	0.10	0.06	0.94	0.62
Li-C ₆₀ Ti	0.11	0.05	0.99	0.53
Na ₃ C ₆₀ Ti	0.11	0.048	0.96	0.62
Na-Na ₃ C ₆₀ Ti	0.09	0.04	0.85	0.58

^a Hydrogen measurement is at 60atm extrapolated to 100atm with goodness of fit (R^2)= 0.9868~0.9972.

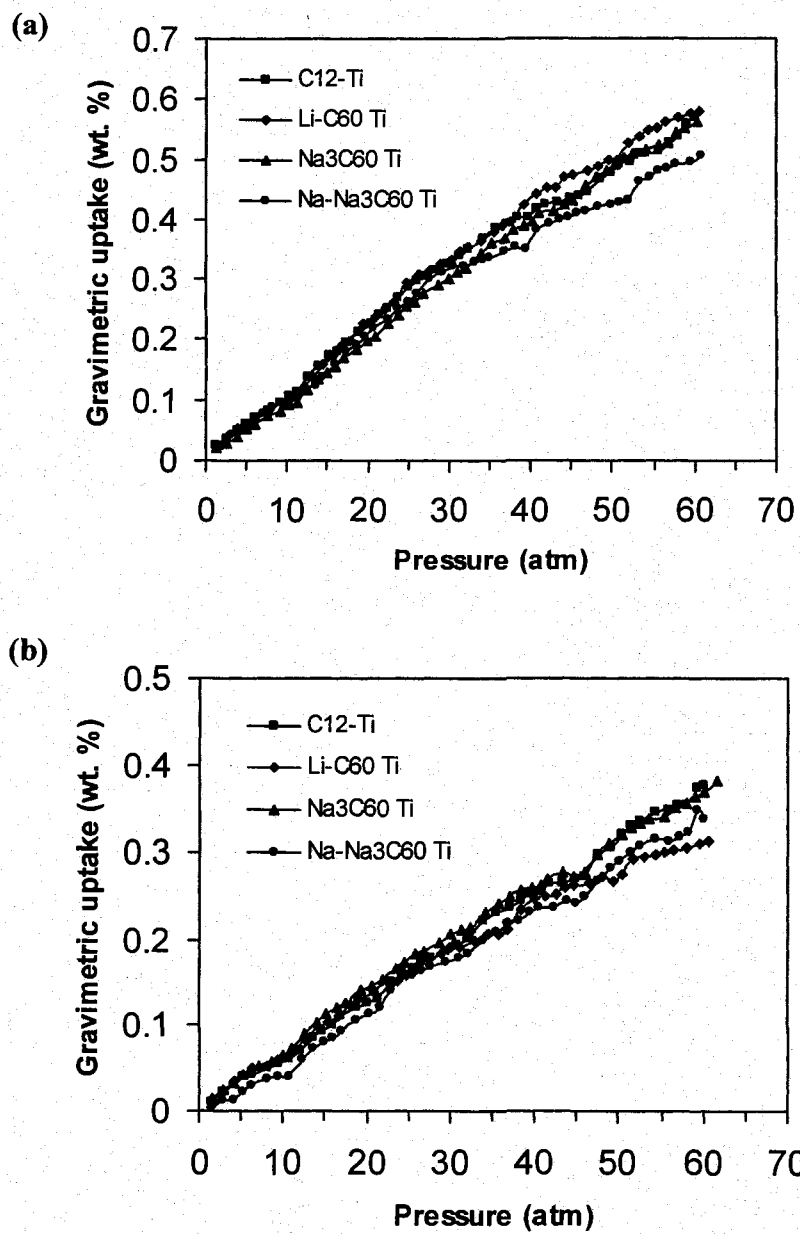


Figure 34. High-pressure H₂ isotherms of gravimetric storage for the alkali fullerides impregnated composites and unreduced material at (a) room temperature and (b) 200° C.

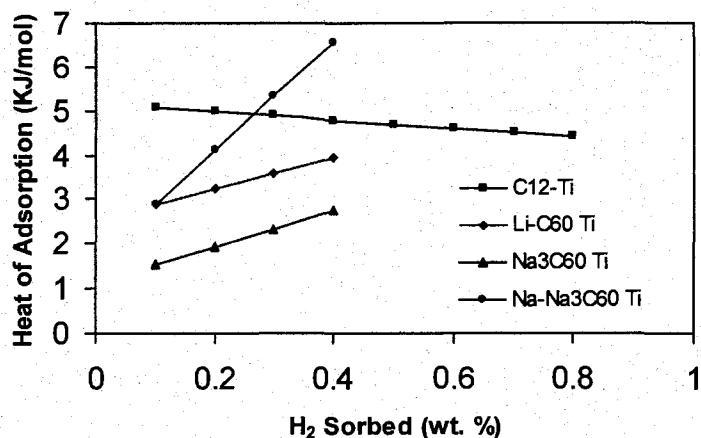


Figure 35. Enthalpies of H₂ adsorption for pristine and alkali fullerides reduced mesoporous titanium oxides.

4.2.3. X-ray Powder Diffraction (XRD) Pattern, Nitrogen Adsorption Study, Elemental Analysis and Raman Spectroscopy of Li Fulleride Composite

In order to gauge the effect of alkali cation size on this system, the analogous Li fulleride composite was prepared. When C12-Ti was treated with Li-naphthalene followed by C₆₀, a new black material (Li-C₆₀ Ti) was formed with a virtually identical XRD pattern to C12-Ti (Figure 36), a BET surface area of 143 m²/g, a BJH pore size of 20 Å, and a pore volume of 0.156 cm³/g. The nitrogen adsorption isotherm of this material is shown in Figure 37. These data are consistent with retention of the mesostructure with partial filling of the channel with fulleride units. The Raman spectrum of this new material (Figure 32c) exhibited an A_g band at 1461 cm⁻¹, which corresponds to a C₆₀ oxidation state of 0.5⁻. The elemental analysis of this material (Table 6) gave 38.78% C and 1.15% H as compared to 3.12% C and 1.36% H in the starting mesoporous Ti oxide. The percentage of Li and Ti in the composite material was 2.77 and 26.3%,

respectively, giving a molar ratio of Li/Ti/C as 0.72/1/5.88. The corresponding Li: C₆₀ ratio was 8.06:1.

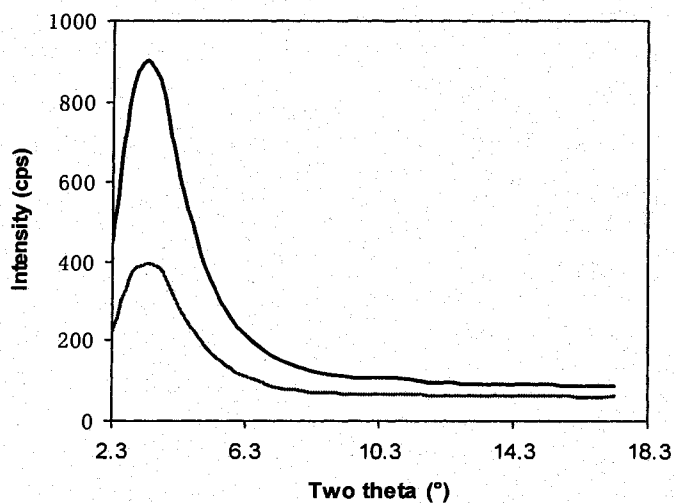


Figure 36. XRD of mesoporous titanium oxide before (upper) and after (lower) treatment with 1 eqv. of Li-naphthalene then doped with maximum C₆₀.

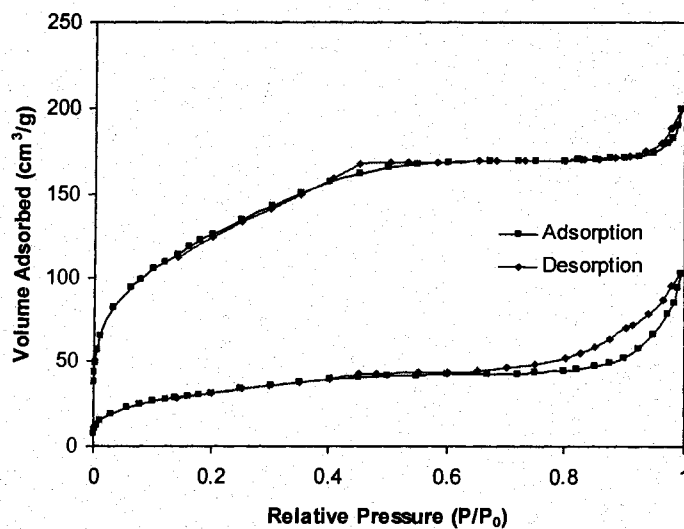


Figure 37. Nitrogen adsorption/desorption isotherms of mesoporous titanium oxide before (upper) and after (lower) treatment with 1 eqv. of Li-naphthalene then doped with maximum C₆₀.

4.2.4. Hydrogen Sorption Properties of Li Fulleride Composite

Hydrogen pressure-composition isotherms at 77 K of both adsorption and storage for 1 eqv. of Li-naphthalene reduced C12-Ti then doped with maximum C₆₀ (Li-C₆₀ Ti) are shown in Figure 33b. This material yielded a total storage of 3.74 wt% and 27.35 kg/m³ in gravimetric and volumetric uptake, respectively. The higher surface area and pore volume of this sample compared to Na₃C₆₀ Ti and Na-Na₃C₆₀ Ti may be responsible for the small increase in both gravimetric and volumetric density observed in Li-C₆₀ Ti. The decreased hydrogen adsorption capacity of Li-C₆₀ Ti, which is only 0.41 wt% and 2.997 kg/m³, compared to that of pristine and Li reduced sample can be explained by the loss of the surface areas and pore volumes, lower degree of surface reduction and less hydrogen binding sites due to the blockage effect of the intercalated fulleride units. From Table 8, we can also see that the gravimetric adsorption and storage capacity for this sample are 0.11 wt% and 0.99 wt% at room temperature and 0.05 wt% and 0.53 wt% at 200°C, similar to those of the Na analogues. The hydrogen binding enthalpy of this material is illustrated in Figure 35. As with Na₃C₆₀ Ti and Na-Na₃C₆₀ Ti, the enthalpy increased with the H₂ capacity. The maximum ΔH for Li-C₆₀ is 3.94 kJ/mol, compared with 5.44 kJ/mol for the Li C12-Ti.

4.3. Discussion

The volumetric storage capacities of this series of fulleride composites are not obviously improved compared to the pristine samples by the inclusion of fulleride units

in the pores. The reason for this may be attributed to several factors. First, alkali fullerides are much weaker reducing agents than the alkali metals or organometallic compounds of transition metals; this can be verified by our previously reported results by XPS binding energy.²¹⁸⁻²²⁴ The mean oxidation state of the Ti in mesoporous Ti oxide reduced by excess K_3C_{60} is 3.7^+ .²²² Since our previous work showed that hydrogen binding to transition metals strongly depends on the electron density at the metal, the sodium fulleride reduced Ti material should have a weaker interaction with hydrogen than its sodium reduced counterpart, which has Ti in the 3^+ oxidation state. Also, the impregnated fulleride units may block access to the active and coordinately unsaturated Ti metal centers, since fulleride addition dramatically decreases the hydrogen adsorption capacity of the materials compared with that of the pristine and fulleride-free alkali metal reduced materials, even when the skeletal density of the fulleride reduced composites is less than that of pristine and alkali metal reduced sample. In previous electrochemical studies comparing the charge transfer inside the pores of Li-reduced mesoporous Ta oxide with this same material impregnated with C_{60} , the C_{60} units hindered, rather than facilitated electron transfer through the pores.²¹⁸ This result was surprising due to the well-known conductive properties of fullerides, and was attributed to steric hindrance of the Li counterions by the fullerides. Thus, steric blockage effect may also be at play in the hydrogen storage properties of this system. The fulleride units not only reduce pore volume of the material and thus decrease the amount of compressed gas residing in the pores, but may also disrupt binding to the Ti oxide surface through steric contact. While these effects might be expected, the major disappointment of this study is that this loss

was not compensated for by the binding of hydrogen to the surface of the fulleride units, expected on the basis of the high sorption capacities of many carbon-based materials.

The increased enthalpies with the increasing of hydrogen uptake amount are consistent with our previously reported results.^{210, 217} However; the enthalpies of the alkali metal fulleride impregnated materials are less than those of fulleride-free Na- and Li-reduced counterparts. In the Li fulleride composites, this can be explained by the transfer of electron density from the walls to the electronegative fullerene phase. This process diminishes the electron density of the Ti in the mesoporous surface. For the Na fulleride composite, the lower level of framework reduction as compared to Na C12-Ti can explain the decreased hydrogen enthalpy for this material. The increased enthalpy of Na-Na₃C₆₀ Ti compared to that of Na C12-Ti can be explained by the higher level of reduction resulting from treatment with Na-naphthalene. Since all other carbon-based physisorption materials show decreasing enthalpies with increasing coverage, the reduced Ti oxide surface must provide the majority of the binding sites in these composites.

4.4. Conclusion

In this study, Li and Na fullerides composite materials were synthesized and characterized by nitrogen adsorption, XRD, Raman spectroscopy and elemental analysis. The adsorption capacities at 77 K of these new composites decreased compared to those of the unreduced pristine sample and the materials reduced with Na or Li only, while the overall storage capacity barely increased. This was attributed to the lower level of reduction of the Ti oxide framework, blockage of active binding Ti sites by the intercalated fulleride units, and the loss of surface area and pore volume without

sufficient compensation by the fulleride surface. The hydrogen sorption of these new composites at room temperature and 200°C showed even more disappointing results. The results from this work and our previous studies show that a highly reduced framework combined with accessible unsaturated metal centers and high surface area and pore volume are needed to achieve useful hydrogen storage capacity.

Chapter 5. Conclusion

Hydrogen storage has attracted a lot of interest recently, because hydrogen is an ideal energy carrier and has potential to replace custom fossil fuels which are not only limited in supply, but also are harmful to the environment. However, the storage of this lightweight and flammable fuel is crucial for the success of the new hydrogen economy. Compressed hydrogen gas and cryogenically stored liquid hydrogen are the most developed technologies, but the former method is suffered by the low hydrogen density and safety concerns about the huge pressure needed, while the large amount of energy required to liquefaction and the continuous boil-off of liquid hydrogen is the significant drawback of the latter. To overcome these problems, solids which absorb hydrogen reversibly with high gravimetric and volumetric density and operate under moderate temperature and pressures are being sought. Micro- and mesoporous Ti oxides are in many ways ideal candidates for this application because they contain ordered channels that allow hydrogen to effectively access the interior space. The synthesis is simple, highly reproducible, and cost-effective. Furthermore, the pore size, surface areas and wall thickness can be systemically modified to improve hydrogen uptake. A unique property of these materials is their ability to act as electron acceptors, due to the capacity for variable oxidation states in the transition metal oxide walls of the micro- and mesoporous structure, a feature not present in MOFs, zeolites, or porous carbon. This exceptional property combined with the coordinative unsaturation Ti centers may possibly improve hydrogen storage capacities.

In this dissertation, I synthesized, characterized and investigated the hydrogen sorption properties for a series of pristine and reduced meso- and microporous titanium oxide composite materials. In Chapter 2, chemically reducible micro- and mesoporous Ti oxides with controlled pore sizes from 12 to 26 Å were synthesized and screened for the hydrogen sorption capacity. The maximum total storage capacity both in gravimetric and volumetric of 5.36 wt% and 29.37 kg/m³ were obtained at 77 K and 100 atm in C6-Ti material, which has a surface area of 942 m²/g and a pore size of 12 Å. The general trend in this series of titanias appears to be one of increasing surface area and decreasing pore size leading to more effective hydrogen storage. Both of these factors have been implicated in hydrogen physisorption to amorphous carbons and MOFs. The binding enthalpies of unreduced materials decreased with increasing surface H₂ coverage, which is typical for physisorption. In order to explore the role of Ti oxidation state in H₂ sorption capacity, C6-Ti was reduced by Li, Na and bis(toluene) Ti. The hydrogen sorption properties of these reduced composites were conducted at the same condition with the pristine material. Surprisingly, unlike MOFs and porous carbons, the hydrogen sorption performance of these new composite materials does not depend greatly on surface area; the oxidation state of the surface Ti species had an even greater effect on the storage densities than surface area or pore size. The maximum total volumetric storage of 40.46 kg/m³ at 77 K and 100 atm was obtained for a bis(toluene) Ti reduced material with a surface area of only 208 m²/g. This value is higher than that of AX-21 which has a surface area of over 3000 m²/g. The hydrogen binding enthalpies for all reduced materials were increasing with the H₂ capacity, with a maximum of 8.08 kJ/mol for bis(toluene) Ti reduced material. This behavior is highly unusual and may reflect a different mechanism

of surface binding than simple physisorption, possibly involving a sigma-pi dihydrogen interaction.

To verify this, in Chapter 3, the microporous C6-Ti material was reduced by excess bis(benzene)V and Cr and bis(cyclopentadienyl) V and Cr. The hydrogen sorption properties investigation of these new composite materials at 77 K found that the gravimetric sorption capacity decreased in each case as compared to that of the unreduced sample, possibly due to increased density or the loss of the surface areas after reduction. However, the overall volumetric storage capacities increased, with a high of 33.42 kg/m³ recorded for the bis(benzene) vanadium reduced material at 77 K and 100 atm. This value is less than that of bis (toluene) Ti reduced material (40.46 kg/m³), due to bis(benzene) vanadium is a weaker reducing agent than bis(toluene) titanium. This emphasizes once more the importance of the reduction of the surface Ti species to the hydrogen sorption capacity. The improved volumetric storage performance of this series of composite materials relative to the untreated samples was attributed to the increased reduction level of the metal centers in the framework of the structure, which allows for more facile π -back donation to the H-H σ bond. Maximum H₂ binding enthalpies ranging from 4.57 to 8.35 kJ/mol were calculated for these reduced composites. The increasing enthalpies with hydrogen adsorption capacity are consistent with results in Chapter 2. These results indicate that further tuning of the H₂ binding enthalpies through using of appropriate reducing agent may achieve even higher hydrogen sorption levels at more moderate temperature.

In Chapter 4, mesoporous titanium oxide lithium and sodium fulleride composites were synthesized and screened for hydrogen sorption capacity at 77 K, room temperature and

200°C, respectively. Maximum overall volumetric uptake of 27.35 and 26.57 kg/m³ were obtained for the Li and Na fulleride composites at 77 K and 100 atm respectively, compared with 25.48 kg/m³ for the pristine unreduced material under the same conditions. These values were less than the fulleride-free Li (28.10 kg/m³) and Na (28.19 kg/m³) reduced materials. At room temperature and 100 atm, the maximum gravimetric storage and adsorption values of the fulleride impregnated composites were 0.99 wt% and 0.11 wt%, respectively, while the corresponding amounts for unreduced material were 0.94 wt% and 0.10 wt%. At 200°C and 100 atm, the maximum gravimetric storage and adsorption capacities of the fulleride composites were less than those of the unreduced material, which were 0.62 wt% and 0.06 wt%, respectively. These disappointing results can be attributed to the lower level of reduction of the Ti oxide framework, blockage of active binding Ti sites by the intercalated fulleride units and the loss of surface area and pore volume without sufficient compensation by the fulleride surface. Hydrogen adsorption enthalpy studies on these fulleride composites showed the increased enthalpies with the increasing of hydrogen uptake amount, which is consistent with results of Chapter 2 and 3. However, the enthalpies of the alkali metal fulleride impregnated materials are less than those of fulleride-free Na- and Li-reduced counterparts, due to the lower level of framework reduction of fulleride composites compared to that of alkali metal reduced counterparts. This can further prove that the reduced surface has a positive effect on the hydrogen storage.

In summary, in this dissertation, micro- and mesoporous Ti oxide materials with different pore sizes and surface areas were prepared and screened for hydrogen storage capacity. Surface area and pore size had some effect on storage density, while reduction

by a variety of reagents led to an even greater increase in storage capacities. This represents a radical new direction in cryogenic hydrogen storage because it is generally thought that surface area and pore size are the only important parameters in determining the storage capacities of porous carbons and MOFs. The unusual trend in enthalpies for reduced materials, which show an unprecedented increase in binding strength as the surface coverage increase was found. This indicates a different adsorption mechanism than physisorption, however the precise mechanism of hydrogen storage is still under investigation. Further efforts are required to find a suitable reducing reagent in order to reach even higher hydrogen storage densities and tune the hydrogen binding enthalpies to over 20 kJ/mol, which is proposed to be ideal value for porous samples operating at ambient temperature.

Appendix:

Hydrogen Storage of Chemically Reduced Mesoporous Ti Oxides at High Temperature.

During the first two years of my study, we collaborated with General Motors on hydrogen storage research. This project focused on the hydrogen storage properties of chemically reduced mesoporous titanium materials at elevated temperature. This appendix will show these unpublished results.

A.1. Experimental Section

A.1.1. Materials and Equipment

Unless otherwise stated, all chemicals were obtained from Aldrich. Trimethylsilyl chloride (TMSCl) was obtained from Alfa and distilled over calcium hydride. In order to remove an excess of moisture and cap OH groups on the internal surface of the titanium oxide mesostructure, which can interfere with the intercalation process by forming metal hydroxide on the internal surface, mesoporous Ti oxides samples were dried at 150°C overnight under vacuum and then stirred with excess trimethylsilyl chloride in dry ether for 12 h under nitrogen. Nitrogen adsorption and desorption data were collected on a Micromeritics ASAP 2010. Bis(toluene) titanium was synthesized by F. G. N. Cloke at the University of Sussex by metal vapor synthesis. Bis(benzene) vanadium was prepared according to the literature.²¹⁴

A.1.2. Synthesis

Synthesis of Mesoporous Titanium Oxide Materials: In a typical preparation, Titanium (IV) isopropoxide (15 g, 52.77 mmol) was warmed with dodecylamine (4.89 g, 26.39 mmol) until a homogeneous colorless solution was obtained. To this solution was added 75 mL of water with stirring. Precipitation occurred immediately. HCl (37 %, 0.2603 g, 2.639 mmol) was then added to the mixture. The mixture was allowed to sit at room temperature overnight without agitation before being transferred to an oven for aging at 40 °C for 2 days, 60 °C for 2 days, and 80 °C for 4 days. The mixture then was filtered by suction filtration, and the white solid was placed into a sealed tube and put into oven at 100 °C for 2 days, 120 °C for 2 days, and 140 °C for 2 days. The product was collected by suction filtration and washed once with a mixture of methanol (375 mL) and diethyl ether (125 mL), and four times with 500 mL methanol. The resulting materials were put into an oven at 150°C for 2 days.

Synthesis of Na Fulleride Composite: To a suspension of the trimethylsilylated sample of mesoporous titanium oxide in dry THF was added excess Na₃C₆₀ (synthesized by heating C₆₀ and Na together in a sealed tube at 200-400 °C and characterized by XRD), as calculated on the basis of 38% Ti determined from the elemental analysis data. The mesoporous Ti solid immediately changed from a light tan color to a deep gray-black. After one week of additional stirring to ensure complete absorption of the fulleride, the reduced material was collected by suction filtration and washed several

times with THF. Once synthesized, the material was dried in vacuo at 1×10^{-3} Torr on a Schlenk line until all condensable volatiles had been removed.

Synthesis of Li Fulleride Composite: Because of the intractable nature of Li fullerides, the mesoporous precursors were first reduced by Li naphthalene and then impregnated with pure C_{60} . This route was used previously by our group to synthesize mesoporous Ta oxide Li fulleride composites.²¹⁸ To a benzene suspension of trimethylsilylated sample of mesoporous titanium oxide previously reduced with 1.0 molar equivalent of lithium naphthalene with respect to Ti was added excess C_{60} . After several days of stirring to ensure complete absorption of the fullerene, the material was collected by suction filtration and washed several times with benzene. The material was dried in vacuo at 1×10^{-3} Torr on a Schlenk line until all condensable volatiles had been removed.

Synthesis of Organometallic Compounds and Li-naphthalene Reduced Mesoporous Titanium Oxides: In a typical synthesis, excess organometallic compound was added to a suspension of trimethylsilylated sample of mesoporous titanium oxide in dry toluene under nitrogen. After 2 days of stirring, the reducing materials were collected by suction filtration and wash with toluene by several times. The resulting materials were further reduced by 1 eqv. of Li-naphthalene, as calculated on the basis of metal percent derived from the elemental analysis data (ca. 38% Ti), in THF solution. After two days stirring, the sample was filtered and washed with THF for several times and dried in vacuo at 10^{-3} Torr on a Schlenk line until all volatiles had been removed.

Synthesis of TiCl₄ and Li-naphthalene Reduced Mesoporous Titanium Oxides: To a suspension of mesoporous titanium oxide in dry toluene under nitrogen was added 1 eqv. of TiCl₄ as calculated on the basis of metal percent derived from the elemental analysis data (ca. 38% Ti). The solution was stirred at 120° C for 2 days. The reduced material was collected by suction filtration under nitrogen and washed with toluene for several times. The resulting materials were dried in vacuo at 10⁻³ Torr on a Schlenk line until all volatiles had been removed. As calculated from the weight change, ca. 15% TiCl₄ was incorporated in the mesostructure. This incorporated material was treated with Li-naphthalene, 4 eqv. with respect to TiCl₄ and 1 eqv. with respect to Ti in TiO₂ in THF solution, after sufficient stirring, the resulting samples were filtered and washed with THF for 4 times then dried in vacuo at 10⁻³ Torr on a Schlenk line until all volatiles had been removed. For the incipient wetness method, the impregnated materials were collected by evaporating the solvent under the vacuum, instead of filtering the solution. Around 90-95% TiCl₄ is incorporated by this technique.

Synthesis of Complex Hydride Reduced Mesoporous Titanium Oxides: To a suspension of mesoporous titanium oxide in dry THF under nitrogen was added 0.5 eqv. of LiAlH₄ or NaBH₄ as calculated on the basis of metal percent derived from the elemental analysis data (ca. 38% Ti). After 2 days of stirring, the reduced material was collected by suction filtration under nitrogen and washed with THF for several times. The resulting materials were dried in vacuo at 10⁻³ Torr on a Schlenk line until all volatiles had been removed.

Synthesis of Superhydride Reduced Mesoporous Titanium Oxides: In a typical synthesis, 1 eqv. of superhydride, as calculated on the basis of metal percent derived from the elemental analysis data (ca. 38% Ti), was added to a suspension of trimethylsilylated sample of mesoporous titanium oxide in dry THF under nitrogen. After stirring for 2 days, the reduced materials were collected by suction filtration and wash with THF by several times. The resulting materials were dried in vacuo at 10^{-3} Torr on a Schlenk line until all volatiles had been removed.

A.2 Results

A.2.1. Hydrogen Sorption Properties of Alkali Fullerides Reduced Mesoporous Ti Oxides

The preliminary results at General Motors showed that 1 eqv. of Li-reduced mesoporous Ti oxide doped with maximum C₆₀ showed a gravimetric uptake of 8 wt% at 200 °C and 1400 PSI (Figure 38). The unreduced mesoporous Ti (IV) oxide only absorbed 1.2 wt% hydrogen and this process was not reversible (Figure 39). These results indicate that the framework must be in a reduced form to absorb hydrogen, suggesting that a mechanism other than capillary action may be involved. To repeat and optimize this promising result, a series of alkali fullerides doped mesoporous Ti oxides with different fullerene doping level, Li reduced level and fulleride doping level were synthesized and the hydrogen storage properties of these composites were investigated at high temperatures.

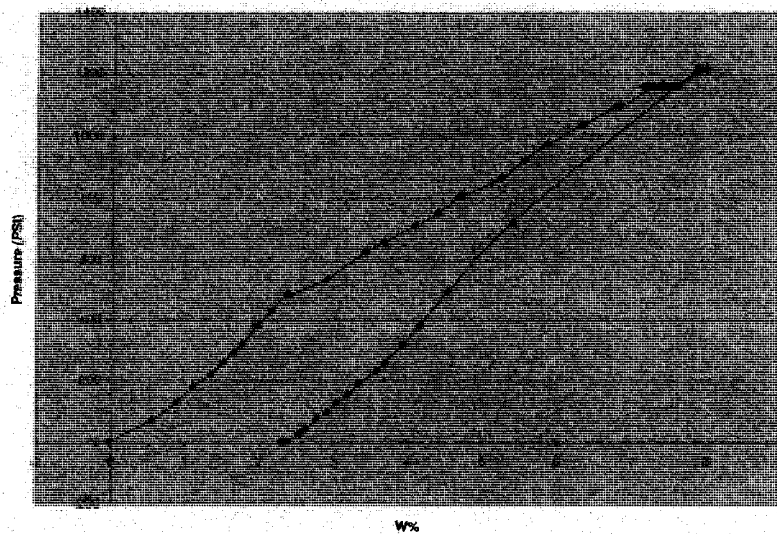


Figure 38. Hydrogen adsorption-desorption isotherm at 200 °C of mesoporous titanium oxide reduced with 1 eqv. of Li-naphthalene and treated with maximum C₆₀.

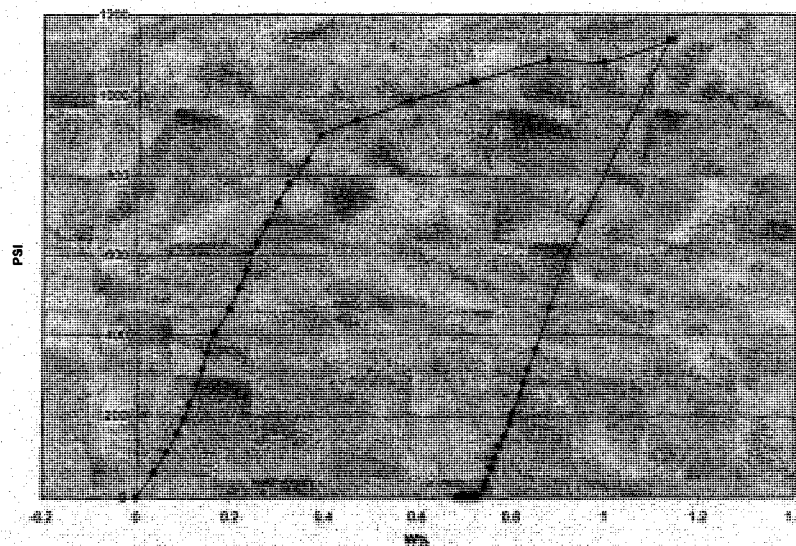


Figure 39. Hydrogen adsorption-desorption isotherm of pristine mesoporous titanium oxide at 200 °C.

A mesoporous Ti oxide synthesized using a dodecylamine template with a BET surface area of 1300 m²/g was stirred with 0.1 eqv. of TMSCl in dry ether for 12 h under nitrogen. The obtained sample had a surface area of 1200 m²/g. Reduction 1 g of this material with 1 and 0.9 eqv. of Li-naphthalene absorbs about 1.38 g of C₆₀(**1**) and 1.03 g of C₆₀ (**2**), respectively. This result was consistent with our previous study that materials treated with smaller amounts of Li are less effective reducing agents and absorb less C₆₀.^{218, 219} The same pristine sample was also reduced by excess Na₃C₆₀ (**3**). The Hydrogen pressure-composition isotherms of **1** and **3** were recorded at 200°C and the results are shown at Figure 40. These results and all other hydrogen sorption results of fulleride composites in this study are summarized in Table 9.

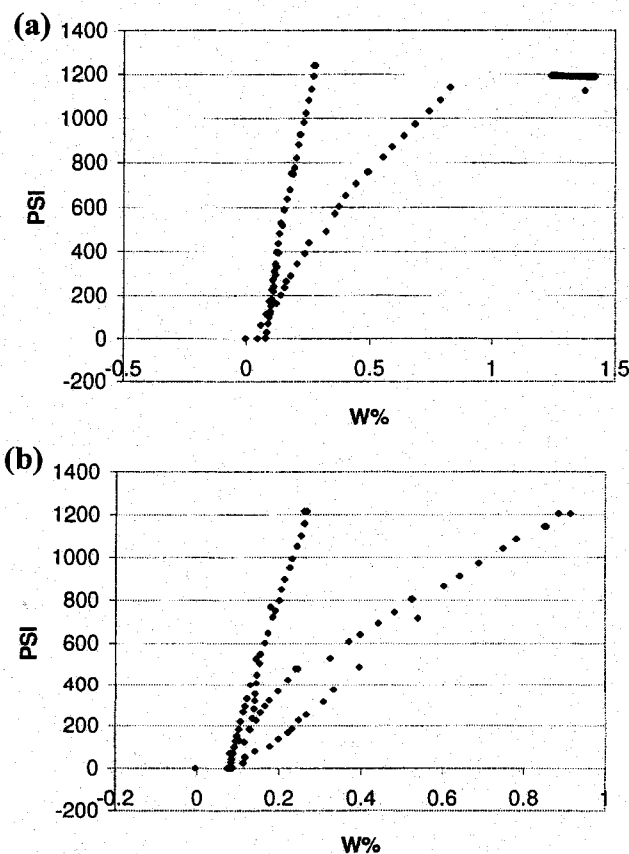


Figure 40. Hydrogen adsorption-desorption isotherms of (a) **1**, (b) **3** at 200°C.

1 absorbed 1.5 wt% of hydrogen and 3 showed a lower reversible hydrogen storage capacity of 0.9 wt%. The low capacities may be due to the fact that these materials were not rigorously dried under high temperature as before. Previous study also indicate that excess TMSCl treated material is advantageous and hence the new reduced materials were prepared using excess TMSCl treated TiO₂ which was subjected to pre and post heat treatments (i.e. Ti oxides was heated at 150 °C before and after the reduction reaction) before the hydrogen storage study. A newly synthesized mesoporous Ti oxides with BET surface area of 662 m²/g was reduced with 1 eqv. of Li-naphthalene and 1.023 g C₆₀/g of TiO₂ was absorbed (4). This sample showed a hydrogen capacity of 2.8 wt% at 200°C; however, only 0.8 wt% was desorbed. The hydrogen storage isotherm of 4 is shown in Figure 41.

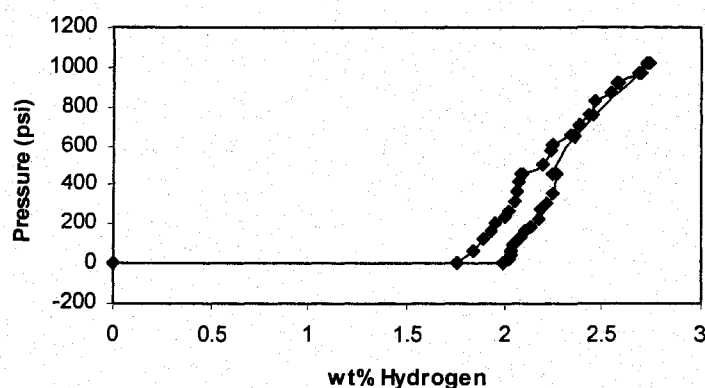


Figure 41. Hydrogen adsorption-desorption isotherm of 4 at 200°C.

The enhanced hydrogen storage capacity of the new sample suggested that heat treatments of materials at 150°C before and after reduction under high vacuum in order to remove any residual solvent/water is essential for improved hydrogen sorption capacity. To gauge the effect of temperature and the surface area on the hydrogen storage capacity,

two new batches of mesoporous Ti oxide materials were synthesized with BET surface area of 407 and 643 m²/g, respectively. The Ti oxide material with the surface area of 407 m²/g was reduced by 1 eqv. of Li-naphthalene and 0.431 g C₆₀/g TiO₂ was absorbed (5). This sample was also reduced with over-excess Na₃C₆₀ (6). The hydrogen storage isotherms were recorded at 150° C for 5 and 6. The results are shown in Figure 42.

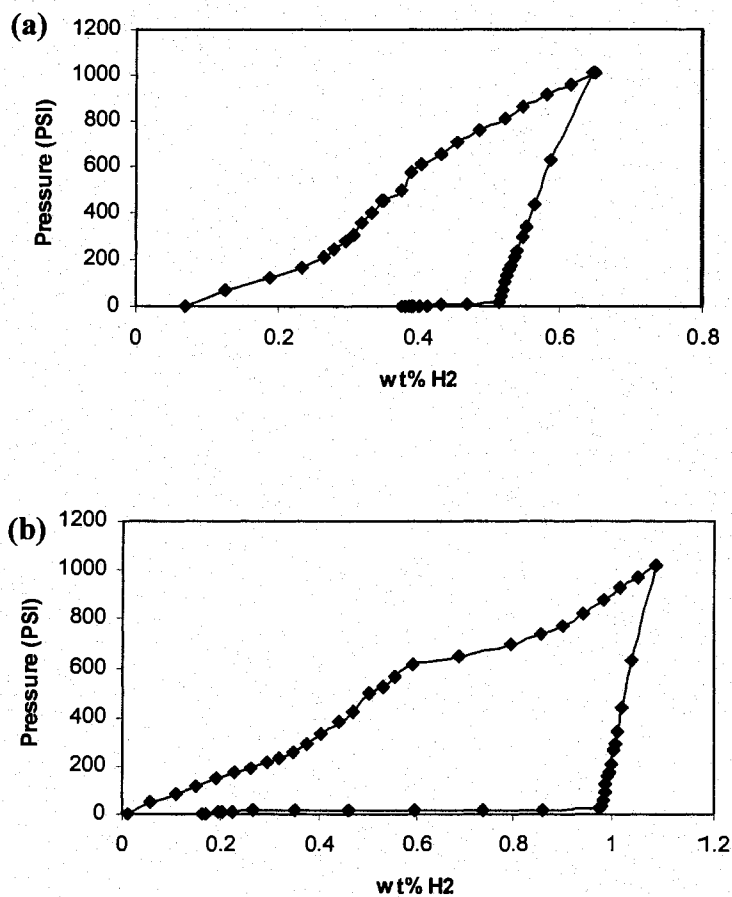


Figure 42. Hydrogen adsorption-desorption isotherms of (a) 5, and (b) 6 at 150°C.

In order to compare, the sample with the BET surface area of 643 m²/g was also reduced by 1 eqv. of Li-naphthalene then doped 0.932 g C₆₀/g TiO₂ (7) and excess Na₃C₆₀ (8). These two samples were tested for hydrogen storage capacity under the same

conditions as 5 and 6, yielding hydrogen storage capacities of 1 wt% and 0.5 wt%, respectively. The isotherms are shown in Figure 43.

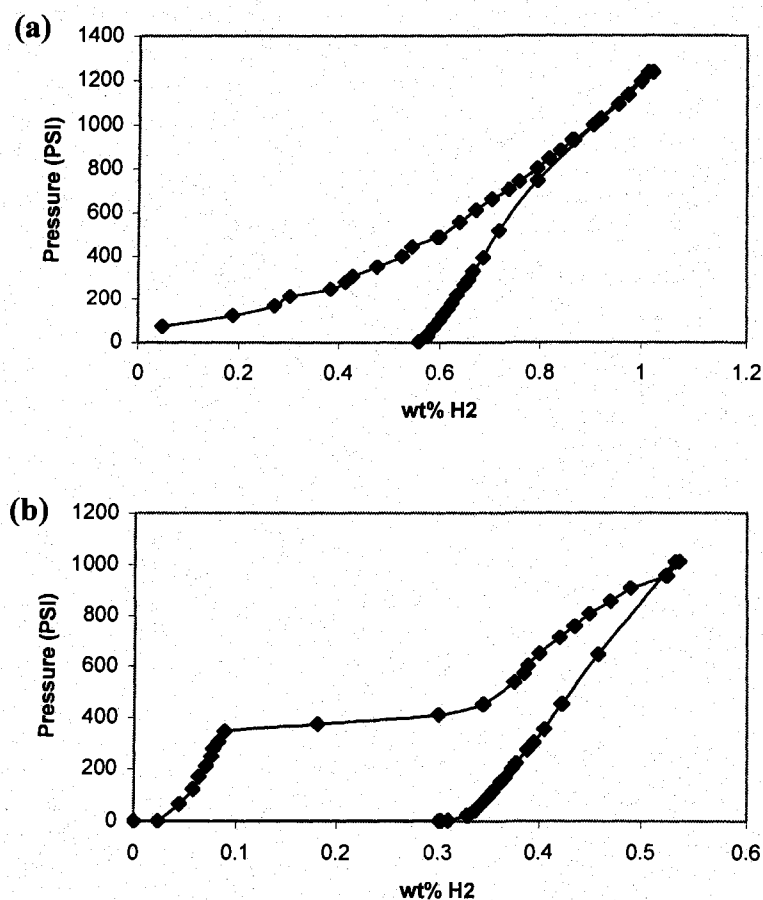


Figure 43. Hydrogen adsorption-desorption isotherms of (a) 7, and (b) 8 at 150°C.

The hydrogen storage capacities decreased substantially with a temperature drop from 200°C to 150°C. Sample 4 had a hydrogen storage capacity of 2.8 wt% at 200°C, while sample 7 showed only 1 wt% of hydrogen uptake at 150°C. Considering similar surface area and similar doped quantity of C₆₀ in these two samples, these results strongly suggest that high temperature is important for hydrogen storage in these types of materials. Accordingly, TiO₂ (surface area 643 m²/g) reduced with 1 eqv. of Li-

naphthalenide doped with 0.932 C₆₀ g/g of TiO₂ (sample 7) showed up to 1 wt% hydrogen absorption. While TiO₂ (surface area 407 m²/g) reduced with 1 eqv. of Li-naphthalene doped with 0.431 C₆₀ g/g of TiO₂ (sample 5) showed only 0.6 wt% hydrogen absorption. Thus it appears that the increase in surface area leading to high doped quantity of C₆₀ is advantageous for increased hydrogen absorption. Notwithstanding, for the samples doped with Na₃C₆₀, the hydrogen storage ability of the over-excess doped Na₃C₆₀ in a lower surface area TiO₂ material (surface area 407 m²/g) was superior to that of a higher surface area TiO₂ material (surface area 643 m²/g) with less Na₃C₆₀ doped. This may indicate that the increasing C amount in the sample is more beneficial for the hydrogen storage than surface area of the material.

From above results, we can see that samples of this class of materials typically have adsorption maxima near 3 wt% at 200°C, but also underperformed at lower temperature.

Table 9. Hydrogen adsorption data for Li reduced mesoporous TiO₂ doped with C₆₀ and mesoporous Ti oxides doped with Na₃C₆₀.

No	TiO ₂ Surface area m ² /g	TMSCl	Li-Naphthalene, eqv.	C ₆₀ g/g of TiO ₂	Na ₃ C ₆₀ g/g of TiO ₂	H ₂ abs, wt%
1	1200	0.1eqv.	1	1.3848		1.5 ^d
2	1200	0.1eqv.			1.066	0.9 ^d
3	1200	0.1eqv.	0.9	1.0353		1.5 ^d
4 ^a	662	excess	1	1.023		2.8 ^d
5 ^a	407	excess	1	0.431		0.6 ^c
6 ^a	407	excess			0.9826 ^b	1 ^c
7 ^a	643	excess	1	0.932		1 ^c
8 ^a	643	excess			0.9148	0.5 ^c

^a pre and post treated

^b over-excess Na₃C₆₀

^c hydrogen test temperature is 150°C

^d hydrogen test temperature is 200°C

A.2.2. Hydrogen Sorption Properties of Organometallic Compounds Reduced Mesoporous Ti Oxides

Initial results at GM showed that the excess bis(toluene) titanium-reduced material absorbs up to 5% hydrogen at 200 °C and 1200 PSI (Figure 44). This material is particularly attractive as a hydrogen storage material because of the simplicity of their elemental composition, essentially containing only Ti and O with a small amount of hydrogen from the water absorbed on or beneath the surface of the Ti gel structure in the walls. This makes it relatively simple to study and characterize.

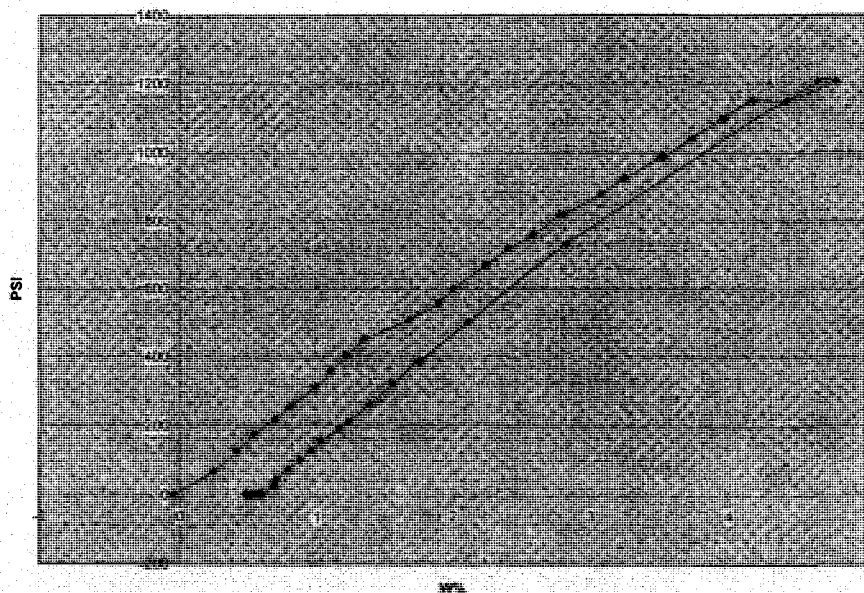


Figure 44. Hydrogen adsorption-desorption isotherm at 200 °C of mesoporous titanium oxide treated with excess bis(toluene) titanium.

To repeat and optimize this initial promising result and better understand the hydrogen storage mechanism in these reduced composites, a series of mesoporous Ti oxides reduced by a variety of organometallic compounds were synthesized and screened at high

temperatures. Previously prepared mesoporous titanium oxide material having a surface area of approximately $1200 \text{ m}^2/\text{g}$ was first treated with 0.1 molar equivalent of TMSCl and was then reduced with 0.5 molar equivalent of bis(toluene) titanium. This material (9) showed only about 0.8 wt% reversible hydrogen adsorption at 200°C and 1200 PSI (Figure 45A). When reduced with 1 molar equivalent of bis(toluene) titanium at a temperature of $60\text{-}80^\circ\text{C}$ (10), the adsorption capacity increased to 3.3 wt% at 200°C and 700 PSI (Figure 45B). However, the desorption was only about 1 wt%. This indicates that by increasing the surface metallic character by reducing the mesoporous titanium oxide, the hydrogen adsorption capacity can be improved.

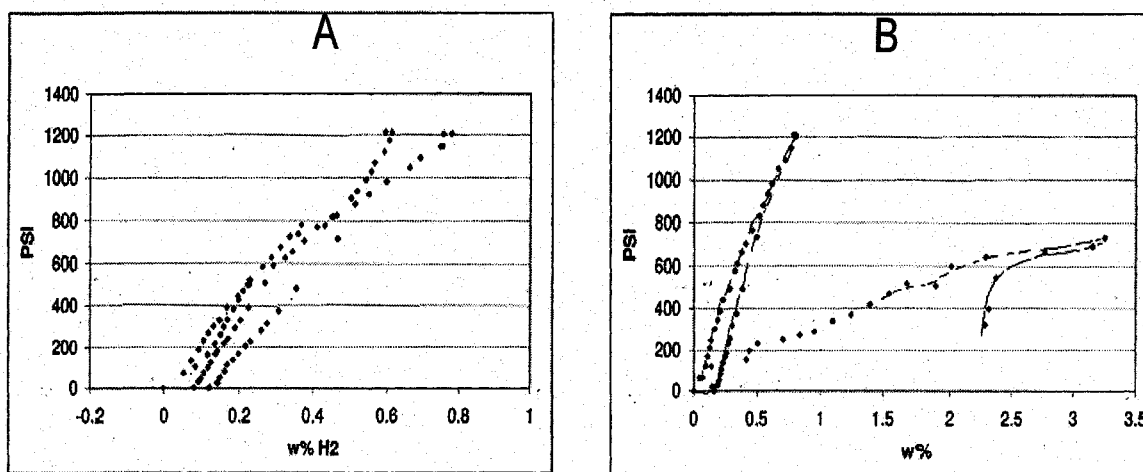


Figure 45. Hydrogen adsorption-desorption isotherms of (A) 9, (B) 10.

The material (with surface area of $1200 \text{ m}^2/\text{g}$) treated with excess of TMSCl and then reduced with 0.6 molar equivalents each of bis(toluene)titanium and lithium naphthalene (11) showed 3.3 wt% reversible hydrogen adsorption (Figure 46). This material was prepared from the pre and post heat treated TiO_2 mentioned above.

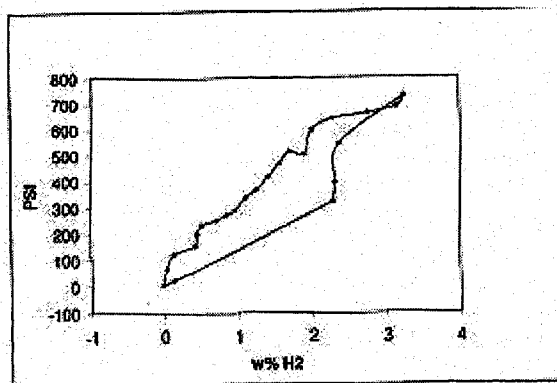


Figure 46. Hydrogen adsorption-desorption isotherm of **11**.

In our previous study, it was found that bis(toluene) titanium reduces the Ti centers in the mesostructure, while also depositing a thin coat of low valent Ti on the surface of the material. The more bis(toluene) titanium absorbed by the material, the lower the ostensible oxidation state of the material. Room temperature absorption usually proceeds until roughly 1 equivalent of organometallic is consumed per unit Ti in the structure. Unpublished results have demonstrated that higher temperatures lead to even more than 1 equivalent of the organometallic being consumed. It is believed that the first process is electrochemical in nature, the mesostructure effectively oxidizing the organometallic to an unstable species which decomposes on the surface and liberates free toluene, while the second is thermally induced, as autocatalytic decomposition of bis(toluene) titanium occurs at elevated temperatures. A new trimethylsilated mesoporous Ti oxide material (with surface area of 516 m²/g) was reduced by 3 eqv. of bis(toluene) Ti at 60°C under excess N₂ (**12**), 1 eqv. of bis(toluene) Ti at room temperature under excess N₂ (**13**), 1 eqv. of bis(benzene) vanadium and bis(toluene) Ti at room temperature under excess N₂ (**14**), 1 eqv. of bis(toluene) Ti and Li-naphthalenide at room temperature under excess N₂ (**15**),

1 eqv. of bis(toluene) Ti and superhydride at room temperature under excess N₂ (16) and 1 eqv. of bis(toluene) Ti at 60°C under excess Ar (17), respectively. The hydrogen storage tests were conducted at 200 °C and the results are summarized in Table 10.

Table 10. Hydrogen sorption data for mesoporous TiO₂ reduced using different methods.

No.	Reducing agent, eqv.	H ₂ sorption, wt%
12	Bis(toluene)Ti, 3 eqv. at 60°C under excess N ₂	1.4
13	Bis(toluene)Ti, 1 eqv. at room temperature under excess N ₂	1.1
14	Bis(benzene)vanadium, 1 eqv. and Bis(toluene)Ti, 1 eqv. at room temperature under excess N ₂	1.2
15	Bis(toluene)Ti, 1 eqv. and Li-naphthalene, 1 eqv. at room temperature under excess N ₂	1.5
16	Bis(toluene)Ti, 1 eqv. and Superhydride, 1 eqv. at room temperature under excess N ₂	1.2
17	Bis(toluene)Ti, 1 eqv. at 60°C under argon	1.5

From the data we can see that the results show only about 1.5 wt% absorption capacities, much lower than the expected 3-5 wt% based on previous research. The reason for these disappointing results is not understood, but may be related to inadvertent oxidation of these samples, which could have occurred during the synthesis of the samples, the flame sealing of the samples, the transportation process, or during measurement (possible leak in pressure-composition isotherms system or impure hydrogen). The extreme air sensitivity of these materials suggests that mesoporous titanium oxide reduced with bis(toluene) titanium, a very difficult compound to synthesize in the first place, may not be a practical alternative as a hydrogen storage material, even though initial results demonstrated adsorption capacity of 3-5% for some

materials. An alternative method to incorporate low valent Ti on TiO₂ surface is to convert the surface –OH groups of TiO₂ to –OTiCl₃ or –OTiCl₂O– with TiCl₄ and then perform the reduction. Approximately 15% TiCl₄ was incorporated by this method and is reduced (4 eqv. with respect to TiCl₄ and 1 eqv. with respect to Ti in TiO₂) with Li-naphthalenide (**18**). Another effective way to get highly reduced Ti species on the surface is to incorporate the required amount TiCl₄ by incipient wetness method and to reduce suitably. Thus 1 equivalent of TiCl₄ is incorporated (approx 90-95 % incorporation) by this method and reduced with Li-naphthalenide (4 eqv. with respect to TiCl₄ and 1 eqv. with respect to Ti in TiO₂), washed several times with THF to get rid of naphthalene and LiCl formed (**19**) and dried properly. The hydrogen storage properties of these two samples were investigated at 150°C. The hydrogen storage isotherms are shown in Figure 47 and the results are summarized in Table 11.

Table 11. Hydrogen sorption data for mesoporous TiO₂ reduced with TiCl₄ and Li-naphthalene.

No.	TiO ₂ Surface area m ² /g	Reducing agent, eqv.	H ₂ sorption, wt%
18^a	762 ^b	Li-naphthalene, 4 eqv. with respect to TiCl ₄ and 1 eqv. with respect to Ti in TiO ₂	1.1 ^d
19^a	762 ^b	Li-naphthalene, 4 eqv. with respect to TiCl ₄ and 1 eqv. with respect to Ti in TiO ₂ ^c	1.3 ^d

^aReduction is carried out at 120 °C

^bTiO₂ without TMSCl treated.

^cPreparation of TiCl₄-TiO₂ by incipient wetness method.

^dHydrogen test temperature is 150 °C

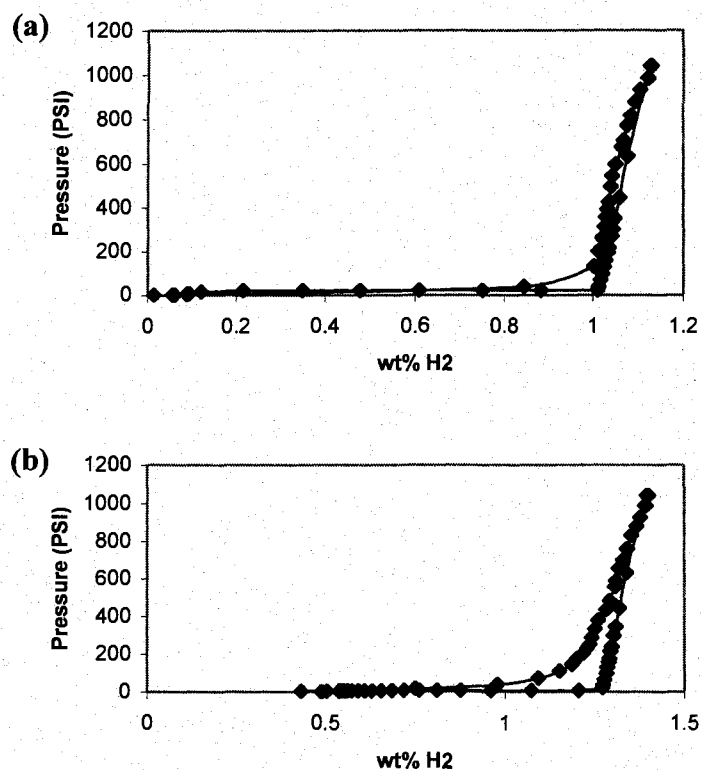


Figure 47. Hydrogen adsorption-desorption isotherms of (a) **18**, (b) **19** at 150 °C.

From these results, it is apparent that the incipient wetting method of introducing TiCl_4 is more effective than the standard method. This finding may be attributable to the higher amount of TiCl_4 incorporated into the mesostructure of the Ti oxides by the incipient wetting method. This route was introduced as a way of obtaining low-valent Ti species on the surface without resorting to use of bis(toluene) titanium. It is envisioned that first anchoring TiCl_4 onto the mesoporous surface followed by reduction with Li-naphthalene and washing away excess naphthalene and LiCl with THF, should lead to low valent Ti on the surface. The lower values as compared to the 3-5 wt% obtained with bis(toluene) titanium can be attributed either to the lower temperatures (the bis(toluene) titanium material was never tested at 150°C), residual Li-Cl on the surface due to incomplete

washing, or incomplete reduction of the Ti-Cl bonds. Thus, this method needs to be investigated further for more definite conclusions to be drawn. Similar to bis(toluene) titanium, bis(benzene) vanadium loses its benzene ligands and deposits a small amount of a low-valent unsaturated vanadium species on the surface of the mesostructure. Bis(benzene) vanadium is also more readily prepared than bis(toluene) Ti and can be obtained in good yield by solution methods.²¹⁴

The hydrogen storage properties of mesoporous Ti oxides reduced by different amounts of bis(benzene) vanadium and other reduction agents were also investigated. A trimethylsilylated mesoporous Ti oxide material (with surface area of 902 m²/g) was reduced by 0.46 eqv. of bis(benzene) vanadium at 60°C (**20**). This material demonstrated 1.9 wt % H₂ adsorption at 200°C, however, only 0.6 wt% was desorbed. In order to incorporate more vanadium on mesoporous TiO₂ by reduction with higher equivalents of bis(benzene) vanadium, the reduction was conducted at higher temperature. Correspondingly, a mesoporous Ti oxide material (with a surface area of 662 m²/g) was reduced by excess bis(benzene) vanadium and 1 eqv. of Li-naphthalene at 120°C (**21**). This sample showed a hydrogen storage capacity of 1.6 wt% reversibly under the same conditions as **20** and the isotherm is shown in Figure 48. Although the hydrogen storage capacity of **21** is less than that of **20**, which can be attributed to the low surface area of the precursor material, it is still a promising result because further levels of reduction can be obtained in this class of materials and reduction level is clearly important in hydrogen adsorption for these materials. What is particularly promising is that the isotherm shows that this material can absorb hydrogen at very low pressure (under 200 PSI), and also

release hydrogen reversibly at low pressure. These pressures are by far the lowest used through the duration of this project and emphasize the promise of these materials.

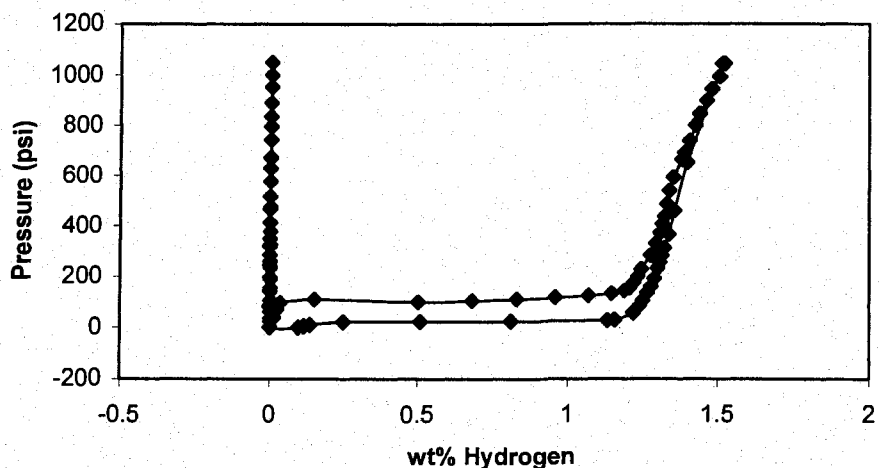


Figure 48. Hydrogen adsorption-desorption isotherm of **21** at 200°C.

To further gauge the effects of test temperature and surface reduction on the hydrogen storage capacity for bis(benzene) vanadium reduced materials, mesoporous Ti oxide with a surface area of 662 m²/g was reduced by excess bis(benzene) vanadium (**22**), and 1 eqv. of bis(benzene) vanadium (**23**) and tested for hydrogen storage at 150°C. The isotherms of these samples are shown in Figure 49 and the results of the bis(benzene) vanadium reduced materials are summarized in Table 12.

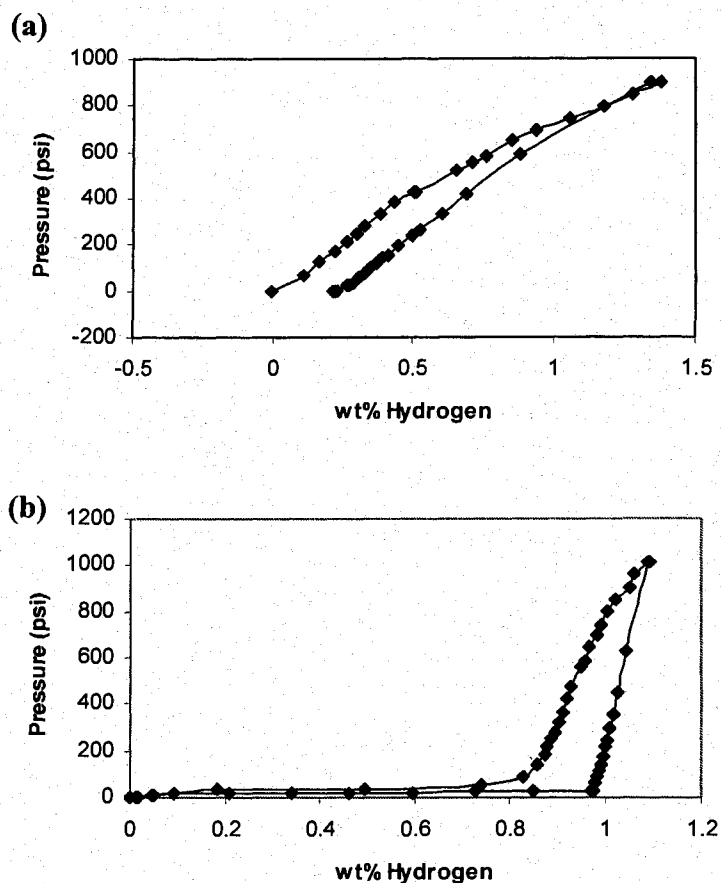


Figure 49. Hydrogen adsorption-desorption isotherms of (a) 22, (b) 23 at 150 °C.

Table 12. Hydrogen sorption data for mesoporous TiO₂ reduced with bis(benzene) vanadium.

No.	TiO ₂ Surface area m ² /g	Reducing agent, eqv.	H ₂ sorption, wt%
20	902	Bis(benzene)V, 0.46 ^b	1.3-1.9 ^c
21	662	Bis(benzene)V, excess and Li-naphthalene 1 ^a	1.6 ^c
22	662	Bis(benzene)V, excess ^a	1.4 ^d
23	662	Bis(benzene)V, 1 ^a	1.1 ^d

^a Reduction is carried out at 120°C

^b Reduction is carried out at 60-80°C

^c Hydrogen test temperature is 200°C

^d Hydrogen test temperature is 150°C

From the data we can see that the hydrogen storage capacities decreased when the temperature dropped from 200°C to 150°C, consistent with the results obtained for the fulleride composites. When compared to the results of **22** and **23**, it is clear that higher reduction in the surface Ti species is beneficial to the hydrogen storage capacity.

A.2.3. Hydrogen Sorption Properties of LiAlH₄ and NaBH₄ Reduced Mesoporous Ti Oxides

Since alanates and borates, especially those prepared as nanocomposites with titanium metal or titanium nitride, are some of the best materials for hydrogen storage, we wanted to explore the anchoring of these inorganic hydrides on the inner surface of the mesoporous titanium oxide framework. Also because alanates and borates are powerful reducing agents, we felt we could reduce the surface of the mesoporous structure, while also maximizing the accessibility of aluminum hydride functionalities by exploiting the massive surface area of the mesostructure. Furthermore, the reduced titanium oxide mesostructure might act as a catalyst in the reversible chemisorption of hydrogen by the alanate, in the same way that TiN or Ti metal does in the nanocomposites studied by Bogdanovic and coworkers.^{187, 188} Two samples were obtained by reducing mesoporous TiO₂ with LiAlH₄ (**24**) and NaBH₄ (**25**) respectively. The hydrogen sorption isotherms are shown in Figure 50 and 51.

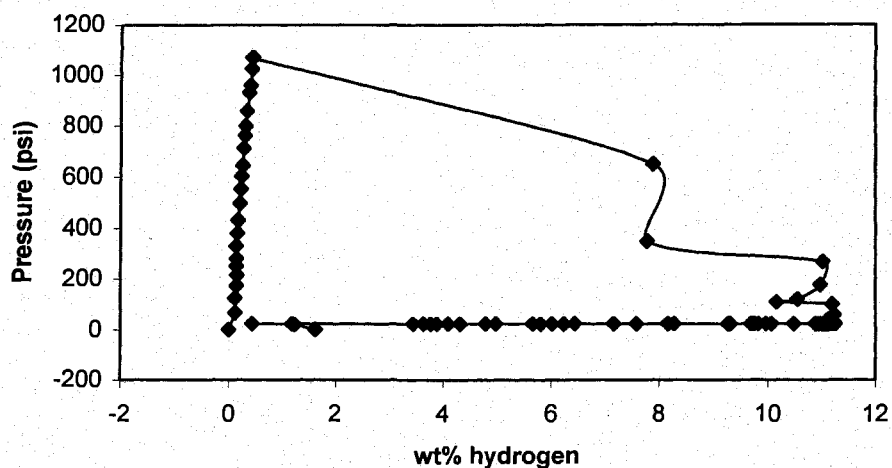


Figure 50. Hydrogen adsorption-desorption isotherm of **24** at 200 °C.

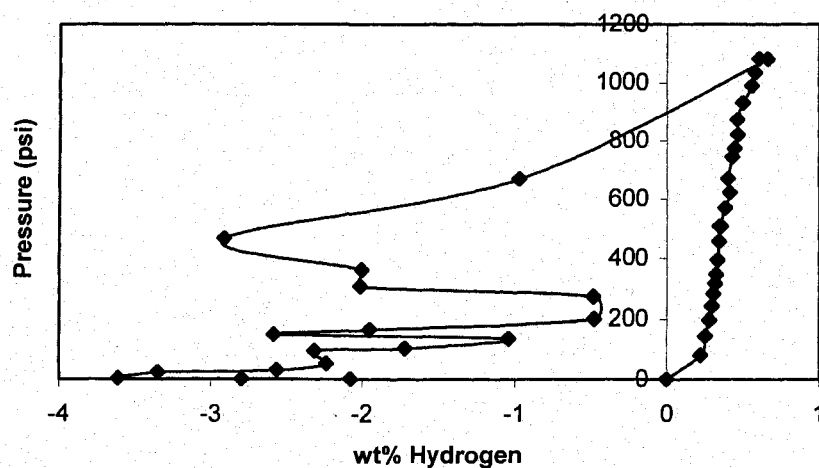


Figure 51. Hydrogen adsorption-desorption isotherm of **25** at 200 °C.

From Figure 50, we can see that **24** shows less than 2 wt% hydrogen absorption. While the desorption branch of the isotherm can desorb hydrogen up to 11 wt%. This is most likely due to decomposition of LiAlH_4 during desorption process. From this we can see that surface reduction of the Ti in the structure by the metal hydrides does indeed lead to increased activity, while the anchored alanate species which remain on the surface can

further contribute to the activity of the materials. The unusually large hysteresis in these curves is not yet understood. Thus, at this stage the unusual hydrogen storage behavior of the **25** can not be explained.

A.2.4. Hydrogen Sorption Properties of Superhydride Reduced Mesoporous Ti Oxides

Mesoporous titanium oxides with different surface areas were reduced by different amounts of superhydride, and the obtained samples were tested for hydrogen storage activity at 200°C. A trimethylsilated mesoporous Ti oxide material possessing a surface area of 902 m²/g) was reduced by 2.5 eqv. of superhydride (**26**) and 1 eqv. of superhydride (**27**), respectively. Another mesoporous titanium oxide material with lower surface area (546 m²/g) reduced by 1 eqv. of superhydride (**28**) was prepared for comparison. The hydrogen storage results are summarized at Table 13.

Table 13. Hydrogen sorption data for mesoporous TiO₂ reduced with super-hydride.

No.	TiO ₂ Surface area m ² /g	Reducing agent, eqv.	H ₂ sorption, wt%	
			1 st cycle	2 nd cycle
26	902	Superhydride, 2.5	2.1–1.7	1.5–1.3
27	902	Superhydride, 1	1.8–1.6	1.4–1.2
28	546	Superhydride, 1	1.4–1.1	0.9–0.8

From these data we can see that increase in surface area and reduction with higher equivalents of reducing agents is advantageous for increased hydrogen absorption. Thus, mesoporous TiO₂ with a surface area of 902 m²/g reduced with 2.5 equivalents of

superhydride gave up to 2.1 wt% H₂ absorption. However, during the reduction process with this reagent, the possibility of forming some stable Ti-H species cannot be ruled out. This may reduce the overall efficiency and because of this, other reduction methods need to be explored.

A.3 Summary

Based on above obtained results, several factors appear to be contributing to the hydrogen capacity of these materials at high temperature. These are:

1. Heat treatment of the mesoporous Ti oxide materials at 150°C before and after the reduction under vacuum in order to remove any residual solvent/water is essential for improved hydrogen sorption capacity.
2. Higher temperatures have an enormous effect on the hydrogen storage ability.
3. The reduction of the Ti surface is of crucial to hydrogen storage. Increasing the surface metallic character by incorporating Ti or V is beneficial for the capacity of hydrogen storage.
4. Increase in surface area leads to higher hydrogen adsorption.

At high temperature, the maximum hydrogen storage capacity for all materials in this study was just over 3 wt%, which falls far short of the DOE 2015 system goal. In an effort to improve these results we concentrated on cryogenic hydrogen storage for the remainder of this study in order to exploit the high surface areas, small pore size and the unique property of tunable oxidation states in the surface of the mesostructure of these materials.

References

1. Schlapbach, L.; Züttel, A. *Nature* **2001**, 414, 353.
2. Zuttel, A. *Mater. Today* **2003**, 6, 24.
3. Liu, C.; Cheng, H. *J. Phys. D: Appl. Phys.* **2005**, 38, R231.
4. Dillon, A.; Heben, M. *Appl. Phys. A: Mater. Sci. Process.* **2001**, 72, 133.
5. Becher, M.; Haluska, M.; Hirscher, M.; Quintel, A.; Skakalova, V.; Dettlaff-Weglikovksa, U.; Chen, X.; Hulman, M.; Choi, Y.; Roth, S.; Meregalli, V.; Parrinello, M.; Strobel, R.; Jorissen, L.; Kappes, M.; Fink, J.; Zuttel, A.; Stepanek, I.; Bernier, P. *C. R. Physique* **2003**, 4, 1055.
6. Ding, R.; Lu, G.; Yan, Z.; Wilson, M. *J. Nanosci. Nanotechnol.* **2001**, 1, 7.
7. Strobel, R.; Garche, J.; Moseley, P.; Jorissen, L.; Wolf, G. *J. Power Sources* **2006**, 159, 781.
8. Chen, Y.; Wu, F. *Appl. Phys. A: Mater. Sci. Process.* **2004**, 78, 989.
9. Hirscher, M.; Becher, M. *J. Nanosci. Nanotechnol.* **2003**, 3, 3.
10. Cheng, H.; Yang, Q.; Liu, C. *Carbon* **2001**, 39, 1447.
11. Rzepka, M.; Lamp, P.; de la Casa-Lillo, M. *J. Phys. Chem. B* **1998**, 102, 10894.
12. Williams, K.; Eklund, P. *Chem. Phys. Lett.* **2000**, 320, 352.
13. Wang, Q.; Johnson, J. *J. Chem. Phys.* **1999**, 110, 577.
14. Wang, Q.; Johnson, J. *J. Phys. Chem. B* **1999**, 103, 4809.
15. Wang, Q.; Johnson, J. *J. Phys. Chem. B* **1999**, 103, 277.
16. Darkrim, F.; Levesque, D. *J. Phys. Chem. B* **2000**, 104, 6773.
17. Yin, Y.; Mays, T.; McEnaney, B. *Langmuir* **2000**, 16, 10521.

18. Guay, P.; Stansfield, B.; Rochefort, A. *Carbon* **2004**, 42, 2187.
19. Volpe, M.; Cleri, F. *Chem. Phys. Lett.* **2003**, 371, 476.
20. Lee, S.; Lee, Y. *Appl. Phys. Lett.* **2000**, 76, 2877.
21. Lee, S.; Park, K.; Choi, Y.; Park, Y.; Bok, J.; Bae, D.; Nahm, K.; Choi, Y.; Yu, S.; Kim, N.; Frauenheim, T.; Lee, Y. *Syn. Met.* **2000**, 113, 209.
22. Lee, S.; An, K.; Lee, Y.; Seifert, G.; Frauenheim, T. *J. Am. Chem. Soc.* **2001**, 123, 5059.
23. Ma, Y.; Xia, Y.; Zhao, M.; Wang, R.; Mei, L. *Phys. Rev. B* **2001**, 63, 115422.
24. Zhang, X.; Cao, D.; Chen, J. *J. Phys. Chem. B* **2003**, 107, 4942.
25. Bauschlicher, C. W., Jr. *Nano Lett.* **2001**, 1, 223.
26. Cheng, H.; Pez, G.; Cooper, A. *J. Am. Chem. Soc.* **2001**, 123, 5845.
27. Han, S.; Kang, J.; Lee, H.; van Duin, A.; Goddard III, W. *Appl. Phys. Lett.* **2005**, 86, 203108.
28. Lee, J.; Kim, H.; Lee, J.; Kang, J. *Appl. Phys. Lett.* **2006**, 88, 143126.
29. Dillon, A.; Jones, K.; Bekkedahl, T.; Kiang, C.; Bethune, D.; Heben, M. *Nature* **1997**, 386, 377.
30. Dillon, A.; Gennett, T.; Jones, K.; Alleman, J.; Parilla, P.; Heben, M. *Proceedings of the 2000 hydrogen program review NREL/CP-507-28890*, **2000**.
31. Hirscher, M.; Becher, M.; Haluska, M.; Dettlaff-Weglikowska, U.; Quintel, A.; Duesberg, G.; Choi, Y.; Downes, P.; Hulman, M.; Roth, S.; Stepanek, I.; Bernier, P. *Appl. Phys. A: Mater. Sci. Process.* **2001**, 72, 129.

32. Hirscher, M.; Becher, M.; Haluska, M.; Quintel, A.; Skakalova, V.; Choi, Y.; Dettlaff-Weglikowska, U.; Roth, S.; Stepanek, I.; Bernier, P.; Leonhardt, A.; Fink, J. *J. Alloys Compd.* **2002**, 330-332, 654.
33. Hirscher, M.; Becher, M.; Haluska, M.; von Zeppelin, F.; Chen, X.; Dettlaff-Weglikowska, U.; Roth, S. *J. Alloys Compd.* **2003**, 356-357, 433.
34. Dillon, A.; Gilbert, K.; Alleman, J.; Gennett, T.; Jones, K.; Parilla, P.; Heben, M. *Proceedings of the 2001 U. S. DOE hydrogen program review NREL/CP-507-30535*, **2001**.
35. Dillon, A.; Gilbert, K.; Parilla, P.; Alleman, J.; Hornyak, G.; Jones, K.; Heben, M. *Proceedings of the 2002 U. S. DOE hydrogen program review NREL/CP-610-32405*, **2002**.
36. Ye, Y.; Ahn, C.; Witham, C.; Fultz, B.; Liu, J.; Rinzler, A.; Colbert, D.; Smith, K.; Smalley, R. *Appl. Phys. Lett.* **1999**, 74, 2307.
37. Liu, C.; Fan, Y.; Liu, M.; Cong, H.; Cheng, H.; Dresselhaus, M. *Science* **1999**, 286, 1127.
38. Chambers, A.; Park, C.; Baker, R.; Rodriguez, N. *J. Phys. Chem. B* **1998**, 102, 4253.
39. Park, C.; Anderson, P.; Chambers, A.; Tan, C.; Hidalgo, R.; Rodriguez, N. *J. Phys. Chem. B* **1999**, 103, 10572.
40. Ahn, C.; Ye, Y.; Ratnakumar, B.; Witham, C.; Bowman, Jr., R.; Fultz, B. *Appl. Phys. Lett.* **1998**, 73, 3378.
41. Tibbetts, G.; Meisner, G.; Olk, C. *Carbon* **2001**, 39, 2291.
42. Ritschel, M.; Uhlemann, M.; Gutfleisch, O.; Leonhardt, A.; Graff, A.; Täschner, C.; Fink, J. *Appl. Phys. Lett.* **2002**, 80, 2985.

43. Lueking, A.; Yang, R.; Rodriguez, N.; Baker, R. *Langmuir* **2004**, *20*, 714.
44. Fan, Y.; Liao, B.; Liu, M.; Wei, Y.; Lu, M.; Cheng, H. *Carbon* **1999**, *37*, 1649.
45. Cheng, H.; Liu, C.; Fan, Y.; Li, F.; Su, G.; Cong, H.; He, L.; Liu, M. *Zeitschrift fuer Metallkunde* **2000**, *91*, 306.
46. Chen, P.; Wu, X.; Lin, J.; Tan, K. *Science* **1999**, *285*, 91.
47. Yang, R. *Carbon* **2000**, *38*, 623.
48. Skakalova, V.; Quintel, A.; Choi, Y.; Roth, S.; Becher, M.; Hirscher, M. *Chem. Phys. Lett.* **2002**, *365*, 333.
49. Pinkerton, F.; Wicke, B.; Olk, C.; Tibbetts, G.; Meisner, G.; Meyer, M.; Herbst, J. *J. Phys. Chem. B* **2000**, *104*, 9460.
50. Nijkamp, M.; Raaymakers, J.; van Dillen, A.; de Jong, K. *Appl. Phys. A: Mater. Sci. Process.* **2001**, *72*, 619.
51. Züttel, A.; Nützenadel, C.; Sudan, P.; Mauron, P.; Emmenegger, C.; Rentsch, S.; Schlapbach, L.; Weidenkaff, A.; Kiyobayashi, T. *J. Alloys Compd.* **2002**, *330*, 676.
52. Zuttel, A.; Sudan, P.; Mauron, P.; Emmenegger, S.; Schlapbach, L. *Int. J. Hydrogen Energy* **2002**, *27*, 203.
53. Kajiura, H.; Tsutsui, S.; Kadono, K.; Kakuta, M.; Ata, M.; Murakami, Y. *Appl. Phys. Lett.* **2003**, *82*, 1105.
54. Poirier, E.; Chahine, R.; Benard, P.; Cossement, D.; Lafi, L.; Melancon, E.; Bose, T.; Deilets, S. *Appl. Phys. A: Mater. Sci. Process.* **2004**, *78*, 961.
55. Schimmel, H.; Kearley, G.; Nijkamp, M.; Visser, C. de Jong, K.; Mulder, F. *Chem. Eur. J.* **2003**, *9*, 4764.

56. Schimmel, H.; Nijkamp, G.; Kearley, G.; Rivera, A.; de Jong, K.; Mulder, F. *Mater. Sci. Eng. B* **2004**, 108, 124.
57. Benard, P.; Chahine, R. *Langmuir* **2001**, 17, 1950.
58. Panella, B.; Hirscher, M.; Roth, S. *Carbon* **2005**, 43, 2209.
59. Hirscher, M.; Panella, B. *J. Alloys Compd.* **2005**, 404-406, 399.
60. Kadono, K.; Kajiura, H.; Shiraishi, M. *Appl. Phys. Lett.* **2003**, 83, 3392.
61. Ströbel, R.; Jörissen, L.; Schliermann, T.; Trapp, V.; Schütz, W.; Bohmhammel, K.; Wolf, G.; Garche, J. *J. Power Sources* **1999**, 84, 221.
62. Zuttel, A.; Sudan, P.; Mauron, P.; Wenger, P. *Appl. Phys. A: Mater. Sci. Process.* **2004**, 78, 941.
63. Chen, Y.; Shaw, D.; Bai, X.; Wang, E.; Lund, C.; Lu, W.; Chung, D. *Appl. Phys. Lett.* **2001**, 78, 2128.
64. Cao, A.; Zhu, H.; Zhang, X.; Li, X.; Ruan, D.; Xu, C.; Wei, B.; Liang, J.; Wu, D. *Chem. Phys. Lett.* **2001**, 342, 510.
65. Wang, Q.; Zhu, C.; Liu, W.; Wu, T. *Int. J. Hydrogen Energy* **2002**, 27, 497.
66. Hou, P.; Yang, Q.; Bai, S.; Xu, S.; Liu, M.; Cheng, H. *J. Phys. Chem. B* **2002**, 106, 963.
67. Hou, P.; Xu, S.; Ying, Z.; Yang, Q.; Liu, C.; Cheng, H. *Carbon* **2003**, 41, 2471.
68. Shiraishi, M.; Takenobu, T.; Yamada, A.; Ata, M.; Kataura, H. *Chem. Phys. Lett.* **2002**, 358, 213.
69. Shiraishi, M.; Takenobu, T.; Kataura, H.; Ata, M. *Appl. Phys. A: Mater. Sci. Process.* **2004**, 78, 947.

70. Gundiah, G.; Govindaraj, A.; Rajalakshmi, N.; Dhathathreyan, K.; Rao, C. *J. Mater. Chem.* **2003**, 13, 209.
71. Gao, H.; Wu, X.; Li, J.; Wu, G.; Lin, J.; Wu, K.; Xu, D. *Appl. Phys. Lett.* **2003**, 83, 3389.
72. Jang, J.; Lee, C.; Oh, C.; Lee, C. *J. Appl. Phys.* **2005**, 98, 074316.
73. Anson, A.; Callejas, M.; Benito, A.; Maser, W.; Izquierdo, M.; Rubio, B.; Jagiello, J.; Thommes, M.; Parra, J.; Martínez, M. *Carbon* **2004**, 42, 1243.
74. Lawrence, J.; Xu, G. *Appl. Phys Lett.* **2004**, 84, 918.
75. Chen, C.; Huang, C. *Int. J. of Hydrogen Energy* **2007**, 32, 237.
76. Zacharia, R.; Kim, K.; Hwang, S.; Nahm, K. *Catalysis Today* **2007**, 120, 426.
77. Gupta, B.; Srivastava, O. *Int. J. Hydrogen Energy* **2000**, 25, 825.
78. Marella, M.; Tomaselli, M. *Carbon* **2006**, 44, 1404.
79. Blackman, J.; Patrick, J.; Arenillas, A.; Shi, W.; Snape, C. *Carbon* **2006**, 44, 1376.
80. Browning, D.; Gerrard, M.; Lakeman, J.; Mellor, I.; Mortimer, R.; Turpin, M. *Nano Lett.* **2002**, 2, 201.
81. Hong, S.; Kim, D.; Jo, S.; Kim, D.; Chin, B.; Lee, D. *Catalysis Today* **2007**, 120, 413.
82. Chahine, R.; Bose, T. *Int. J. Hydrogen Energy* **1994**, 19, 161.
83. Zhou, L.; Zhou, Y.; Sun, Y. *Int. J. Hydrogen Energy* **2004**, 29, 475.
84. De la Casa-Lillo, M.; Lamari-Darkrim, F.; Cazorla-Amoros, D.; Linares-Solano, A. *J. Phys. Chem B* **2002**, 106, 10930.
85. Texier-Mandoki, N.; Dentzer, J.; Piquero, T.; Saadallah, S.; David, P.; Vix-Guterl, C. *Carbon* **2004**, 42, 2744.
86. Zhao, X.; Xiao, B.; Fletcher, A.; Thomas, K. *J. Phys. Chem. B* **2005**, 109, 8880.

87. Kabbour, H.; Baumann, T.; Satcher, J. Jr.; Saulnier, A.; Ahn, C. *Chem. Mater.* **2006**, 18, 6085.
88. Orimo, S.; Majer, G.; Fukunaga, T.; Zuttel, A.; Schlapbach, L.; Fujii, H. *Appl. Phys. Lett.* **1999**, 75, 3093.
89. Orimo, S.; Matsushima, T.; Fujii, H.; Fukunaga, T.; Majer, G. *J. Appl. Phys.* **2001**, 90, 1545.
90. Chen, D.; Ichikawa, T.; Fujii, H.; Ogita, N.; Udagawa, M.; Kitano, Y.; Tanabe, E. *J. Alloys Compd.* **2003**, 354, L5-L9.
91. Pang, J.; Hanpsev, J.; Wu, Z.; Hu, Q.; Lu, Y. *Appl. Phys. Lett.* **2004**, 85, 4887.
92. Shao, X.; Wang, W.; Xue, R.; Shen, Z. *J. Phys. Chem. B* **2004**, 108, 2970.
93. Gogotsi, Y.; Dash, R.; Yushin, G.; Yildirim, T.; Laudisio, G.; Fischer, J. *J. Am. Chem. Soc.* **2005**, 127, 16006.
94. Yang, Z.; Xia, Y.; Mokaya, R. *J. Am. Chem. Soc.* **2007**, 129, 1673.
95. Terres, E.; Panella, B.; Hayashi, T.; Kim, Y.; Endo, M.; Dominguez, J.; Hirscher, M.; Terrones, H.; Terrones, M. *Chem. Phys. Lett.* **2005**, 403, 363.
96. Yang, F.; Yang, R. *Carbon* **2002**, 40, 437.
97. Lueking, A.; Yang, R. *J. Catal.* **2002**, 206, 165.
98. Lueking, A.; Yang, R. *Appl. Catal. A* **2004**, 265, 259.
99. Lachawiec, A.; Qi, G.; Yang, R. *Langmuir* **2005**, 21, 11418.
100. Yang, F.; Lachawiec, A.; Yang, R. *J. Phys. Chem. B* **2006**, 110, 6236.
101. Mu, S.; Tang, H.; Qian, S.; Pan, M.; Yuan, R. *Carbon* **2006**, 44, 762.
102. Zacharia, R.; Rather, S.; Hwang, S.; Nahm, K. *Chem. Phys. Lett.* **2007**, 434, 286.
103. Lee, Y.; Kim, Y.; Hong, J.; Suh, J.; Cho, G. *Catalysis Today* **2007**, 120, 420.

104. Eddaoudi, M.; Li, H.; Reineke, T.; Fehr, M.; Kelley, D.; Groy, T.; Yaghi, O. *Top. Catal.* **1999**, *9*, 105.
105. Eddaoudi, M.; Moler, D.; Li, H.; Chen, B.; Reineke, T.; O’Keeffe, M.; Yaghi, O. *Acc. Chem. Res.* **2001**, *34*, 319.
106. Chae, H.; Siberio-Perez, D.; Kim, J.; Go, Y.; Eddaoudi, M.; Matzger, A.; O’Keeffe, M.; Yaghi, O. *Nature* **2004**, *427*, 523.
107. Yaghi, O.; O’Keeffe, M.; Ockwig, N.; Chae, H.; Eddaoudi, M.; Kim, J. *Nature* **2003**, *423*, 705.
108. Li, H.; Eddaoudi, M.; O’Keeffe, M.; Yaghi, O. *Nature* **1999**, *402*, 279.
109. Rowsell, J.; Yaghi, O. *Microporous Mesoporous Mater.* **2004**, *73*, 3.
110. Kitagawa, S.; Kitaura, R.; Noro, S. *Angew. Chem., Int. Ed.* **2004**, *43*, 2334.
111. Janiak, C. *Dalton Trans.* **2003**, *14*, 2781.
112. Rowsell, J.; Yaghi, O. *Angew. Chem., Int. Ed.* **2005**, *44*, 4670.
113. Rosseinsky, M. *Microporous Mesoporous Mater.* **2004**, *73*, 15.
114. Fletchera, A.; Thomas, K.; Rosseinsky, M. *J. Solid State Chem.* **2005**, *178*, 2491.
115. Rosi, N.; Eckert, J.; Eddoudi, M.; Vodak, D.; Kim, J.; O’Keeffe, M.; Yaghi, O. *Science* **2003**, *300*, 1127.
116. Rowsell, J.; Milward, A.; Park, K.; Yaghi, O. *J. Am. Chem. Soc.* **2004**, *126*, 5666.
117. Panella, B.; Hirscher, M. *Adv. Mater.* **2005**, *17*, 538.
118. Wong-Foy, A.; Matzger, A.; Yaghi, O. *J. Am. Chem. Soc.* **2006**, *128*, 3494.
119. Langmi, H.; Walton, A.; Al-Mamouri, M.; Johnson, S.; Book, D.; Speight, J.; Edwards, P.; Gameson, I.; Anderson, P.; Harris, I. *J. Alloys Compd.* **2003**, *356–357*, 710.

120. Pan, L.; Sander, M.; Huang, X.; Li, J.; Smith, M.; Bittner, E.; Bockrath, B.; Johnson, J. *J. Am. Chem. Soc.* **2004**, 126, 1308.
121. Kesanli, B.; Cui, Y.; Smith, M.; Bittner, E.; Bockrath, B.; Lin, W. *Angew. Chem., Int. Ed.* **2005**, 44, 72.
122. Dybsteve, D.; Chun, H.; Yoon, S. H.; Kim, D.; Kim, K. *J. Am. Chem. Soc.* **2004**, 126, 32.
123. Dybsteve, D.; Chun, H.; Kim, K. *Angew. Chem., Int. Ed.* **2004**, 43, 5033.
124. Lee, E.; Suh, M. *Angew. Chem., Int. Ed.* **2004**, 43, 2798.
125. Kubota, Y.; Takata, M.; Matsuda, R.; Kitaura, R.; Kitagawa, S.; Kato, K.; Sakata, M.; Kobayashi, T. *Angew. Chem., Int. Ed.* **2005**, 44, 920.
126. Chen, B.; Ockwig, N.; Millward, A.; Contreras, D.; Yaghi, O. *Angew. Chem., Int. Ed.* **2005**, 44, 4745.
127. Chen, B.; Ma, S.; Zapata, F.; Lobkovsky, E.; Yang, J. *Inorg. Chem.* **2006**, 45, 5718.
128. Lee, J.; Pan, L.; Kelly, S.; Jagiello, J.; Emge, T.; Li, J. *Adv. Mater.* **2005**, 17, 2703.
129. Chun, H.; Dybsteve, D.; Kim, H.; Kim, K. *Chem. Eur. J.* **2005**, 11, 3521.
130. Zhao, X.; Xiao, B.; Fletcher, A.; Thomas, K.; Bradshaw, D.; Rosseinsky, M. *Science* **2004**, 306, 1012.
131. Kaye, S.; Long, J. *J. Am. Chem. Soc.* **2005**, 127, 6506.
132. Chapman, K.; Southon, P.; Weeks, C.; Kepert, C. *Chem. Commun.* **2005**, 3322.
133. Dinca, M.; Long, J. *J. Am. Chem. Soc.* **2005**, 127, 9376.
134. Kaye, S.; Long, J. *Catalysis Today* **2007**, 120, 311.
135. Yang, Q.; Zhong, C. *J. Phys. Chem. B* **2005**, 109, 11862.
136. Yang, Q.; Zhong, C. *J. Phys. Chem. B* **2006**, 110, 655.

137. Krawiec, P.; Kramer, M.; Sabo, M.; Kunschke, R.; Frode, H.; Kaskel, S. *Adv. Eng. Mater.* **2006**, *8*, 293.
138. Lee, J.; Li, J.; Jagiello, J. *J. Solid State Chem.* **2005**, *178*, 2527.
139. Panella, B.; Hirscher, M.; Putter, H.; Muller, U. *Adv. Funct. Mater.* **2006**, *16*, 520.
140. Peterson, V.; Liu, Y.; Brown, C.; Kepert, C. *J. Am. Chem. Soc.* **2006**, *128*, 15578.
141. Ferey, G.; Latroche, M.; Serre, C.; Millange, F.; Loiseau, T.; Percheron-Guegan, A. *Chem. Commun.* **2003**, 2976.
142. Ferey, G.; Mellot-Draznieks, C.; Serre, C.; Millange, F.; Dutour, J.; Surble, S.; Margiolaki, L. *Science* **2005**, *309*, 2040.
143. Latroche, M.; Surble, S.; Serre, C.; Mellot-Draznieks, C.; Llewellyn, P.; Lee, J.; Chang, J.; Jhung, S.; Ferey, G. *Angew. Chem., Int. Ed.* **2006**, *45*, 8227.
144. Surble, S.; Millange, F.; Serre, C.; Duren, T.; Latroche, M.; Bourrelly, S.; Llewellyn, P.; Ferey, G. *J. Am. Chem. Soc.* **2006**, *128*, 14889.
145. Sun, D.; Ma, S.; Ke, Y.; Collins, D.; Zhou, H. *J. Am. Chem. Soc.* **2006**, *128*, 3896.
146. Ma, S.; Zhou, H. *J. Am. Chem. Soc.* **2006**, *128*, 11734.
147. Dinca, M.; Yu, A.; Long, J. *J. Am. Chem. Soc.* **2006**, *128*, 8904.
148. Dinca, M.; Dailly, A.; Liu, Y.; Brown, C.; Neumann, D.; Long, J. *J. Am. Chem. Soc.* **2006**, *128*, 16876.
149. Forster, P.; Eckert, J.; Chang, J.; Park, S.; Ferey, G.; Cheetham, A. *J. Am. Chem. Soc.* **2003**, *125*, 1309.
150. Foster, P.; Eckert, J.; Heiken, B.; Parise, J.; Yoon, J.; Jhung, S.; Chang, J.; Cheetham, A. *J. Am. Chem. Soc.* **2006**, *128*, 16846.
151. Dailly, A.; Vajo, J.; Ahn, C. *J. Phys. Chem. B* **2006**, *110*, 1099.

152. Lin, X.; Jia, J.; Zhao, X.; Thomas, K.; Blake, A.; Walker, G.; Champness, N., Hubberstey, P.; Schroder, M. *Angew. Chem., Int. Ed.* **2006**, 45, 7358.
153. Jhung, S.; Kim, H.; Yoon, J.; Chang, J. *J. Phys. Chem. B* **2006**, 110, 9371.
154. Dietzel, P.; Panella, B.; Hirscher, M. Blom, R.; Fjellvag, H. *Chem. Commun.* **2006**, 959.
155. Frost, H.; Duren, T.; Snurr, R. *J. Phys. Chem. B* **2006**, 110, 9565.
156. Li, Y.; Yang, R. *J. Am. Chem. Soc.* **2006**, 128, 726.
157. Li, Y.; Yang, R. *J. Am. Chem. Soc.* **2006**, 128, 8136.
158. Weitkamp, J.; Fritz, M.; Ernst, S. *Int. J. Hydrogen Energy* **1995**, 20, 967.
159. Kazansky, V.; Borovkov, V.; Serich, A.; Karge, H. *Microporous Mesoporous Mater.* **1998**, 22, 251.
160. Takagi, H.; Hatori, H.; Soneda, Y.; Yoshizawa, N. Yamada, Y. *Mater. Sci. Eng. B* **2004**, 108, 143.
161. Langmi, H.; Book, D.; Walton, A.; Johnson, S.; Al-Mamouri, M.; Speight, J.; Edwards, P.; Harris, I.; Anderson, P. *J. Alloys Compd.* **2005**, 404-406, 637.
162. Vitillo, J.; Ricchiardi, G.; Spoto, G.; Zecchina, A. *Phys. Chem. Chem. Phys.* **2005**, 7, 3948.
163. Zecchina, A.; Bordiga, S.; Vitillo, J.; Ricchiardi, G.; Lamberti, C.; Spoto, G.; Bjorgen, M.; Lillerud, K. *J. Am. Chem. Soc.* **2005**, 127, 6361.
164. Regli, L.; Zecchina, A.; Vitillo, J.; Cocina, D.; Spoto, G.; Lamberti, C.; Lillerud, K.; Olsbye, U.; Bordiga, S. *Phys. Chem. Chem. Phys.* **2005**, 7, 3197.
165. Areat, C.; Delgado, M.; Palomino, G.; Rubio, M.; Tsyganenko, N.; Tsyganenko, A.; Garrone, E. *Microporous Mesoporous Mater.* **2005**, 80, 247.

166. Li, Y.; Yang, R. *J. Phys. Chem. B* **2006**, 110, 17175.
167. Hu, Y.; Ruckenstein, E. *Angew. Chem., Int. Ed.* **2006**, 45, 2011.
168. Mao, W.; Mao, H.; Goncharov, A.; Struzhkin, V.; Guo, Q.; Hu, J.; Shu, J.; Hemley, R.; Somayazulu, M.; Zhao, Y. *Science* **2002**, 297, 2247.
169. Mao, W.; Mao, H. *Proc. Natl. Acad. Sci. USA* **2004**, 101, 708.
170. Patchkovskii, S.; Tse, J. *Proc. Natl. Acad. Sci. USA* **2003**, 100, 14645.
171. Florusse, L.; Peters, C.; Schoonman, J.; Hester, K.; Koh, C.; Dec, S.; Marsh, K.; Sloan, D. *Science* **2004**, 306, 469.
172. Lee, H.; Lee, J.; Kim, D.; Park, J.; Seo, Y.; Zeng, H.; Moudrakovski, I.; Ratcliffe, C.; Ripmeester, J. *Nature* **2005**, 434, 743.
173. Strobel, T.; Taylor, C.; Hester, K.; Dec, S.; Koh, C.; Miller, K.; Sloan, E., Jr. *J. Phys. Chem. B* **2006**, 110, 17121.
174. Chapoy, A.; Anderson, R.; Tohidi, B. *J. Am. Chem. Soc.* **2007**, 129, 746.
175. Zuttel, A. *Naturwissenschaften* **2004**, 91, 157.
176. Schulz, R.; Huot, J.; Liang, G.; Boily, S.; Lalande, G.; Denis, M.; Dodelet, J. *Mater. Sci. Eng. A* **1999**, 267, 240.
177. Zaluska, A.; Zaluski, L.; Strom-Olsen, J.; *J. Alloy Compd.* **1999**, 288, 217.
178. Zaluska, A.; Zaluski, L.; Strom-Olsen, J. *Appl. Phys. A: Mater. Sci. Process.* **2001**, 72, 157.
179. Liang, G.; Huot, J.; Boily, S.; Van Neste, A.; Schulz, R. *J. Alloy Compd.* **1999**, 291, 295.
180. Liang, G.; Huot, J.; Boily, S.; Schulz, R. *J. Alloy Compd.* **2000**, 305, 239.
181. Von Zeppelin, F.; Reule, H.; Hirscher, M. *J. Alloy Compd.* **2002**, 330-332, 727.

182. Orimo, S.; Fujii, H. *Appl. Phys. A: Mater. Sci. Process.* **2001**, 72, 167.
183. Zeng, K.; Klassen, T.; Oelerich, W.; Bormann, R. *J. Alloy Compd.* **1999**, 283, 213.
184. Gutfleisch, O.; Schlorke-de Boer, N.; Ismail, N.; Herrich, M.; Walton, A.; Speight, J.; Harris, I.; Pratt, A.; Züttel, A. *J. Alloy Compd.* **2003**, 356-357, 598.
185. Bobet, J.; Pechev, S.; Chevalier, B.; Darriet, B. *J. Mater. Chem.* **1999**, 9, 315.
186. Bogdanovic, B.; Schwickardi, M. *J. Alloy Compd.* **1997**, 253-254, 1.
187. Bogdanovic, B.; Brand, R.; Marjanovic, A.; Schwickardi, M.; Tolle, J. *J. Alloy Compd.* **2000**, 302, 36.
188. Bogdanovic, B.; Felderhoff, M.; Kaskel, S.; Pommerin, A.; Schlichte, K.; Schuth, F. *Adv. Mater.* **2003**, 15, 1012.
189. Zidan, R.; Satoshi, T.; Hee, A.; Jensen, C. *J. Alloy Compd.* **1999**, 285, 119.
190. Anton, D. *J. of Alloy Compd.* **2003**, 356-357, 400.
191. Jensen, C.; Zidan, R.; Mariels, N.; Hee, A.; Hagen, C. *Int. J. Hydrogen Energy* **1999**, 24, 461.
192. Zaluska, A.; Zaluski, L.; Strom-Olsen, J. *J. Alloy Compd.* **2000**, 298, 125.
193. Gross, K.; Sandrock, G.; Thomas, G. *J. Alloy Compd.* **2002**, 330-332, 691.
194. Thomas, G.; Gross, K.; Yang, N.; Jensen, C. *J. Alloy Compd.* **2002**, 330-332, 702.
195. Zuttel, A.; Wenger, P.; Rentsch, S.; Sudan, P.; Mauron, Ph.; Emmenegger, Ch. *J. Power Sources* **2003**, 118,1.
196. Seayad, A. M.; Antonelli, D. *Adv. Mater.* **2004**, 16, 765.
197. Antonelli, D. *Microporous Mesoporous Mater.* **1999**, 30, 315.
198. He, X.; Antonelli, D. *Angew. Chem., Int. Ed.* **2002**, 41, 214.
199. Kubas, G. *J. Organomet. Chem.* **2001**, 635, 37.

200. Zhao, Y.; Kim, Y.; Dillon, A.; Heben, M.; Zhang, S. *Phys. Rev. Lett.* **2005**, *94*, 155504.
201. Yildirim, T.; Ciraci, S. *Phys. Rev. Lett.* **2005**, *94*, 155504.
202. Kubas, G.; Ryan, R.; Swanson, B.; Vergamini, P.; Wasserman, H. *J. Am. Chem. Soc.* **1984**, *106*, 450.
203. Vettrano, M.; Trudeau, M.; Antonelli, D. *Adv. Mater.* **2000**, *12*, 337.
204. Vettrano, M.; Trudeau, M.; Antonelli, D. *Inorg. Chem.* **2001**, *40*, 2088.
205. Lezau, A.; Skadtchenko, B.; Trudeau, M.; Antonelli, D. *Dalton Trans.* **2003**, *21*, 4115.
206. Vettrano, M.; Trudeau, M.; Lo, A.; Schurko, R.; Antonelli, D. *J. Am. Chem. Soc.* **2002**, *124*, 9567.
207. Sun, T.; Ying, J. *Nature* **1997**, *389*, 704.
208. Menon, P. *Chem. Rev.* **1968**, *68*, 277.
209. Roquerol, F.; Rouquerol, J.; Sing, K. *Adsorption by Powders and Solids: Principles, Methodology, and Applications*, Academic Press: London, **1999**.
210. Hu, X.; Skadtchenko, B.; Trudeau, M.; Antonelli, D. *J. Am. Chem. Soc.* **2006**, *128*, 11740.
211. He, X.; Trudeau, M.; Antonelli, D. *Adv. Mater.* **2000**, *12*, 1036.
212. He, X.; Trudeau, M.; Antonelli, D. *Inorg. Chem.* **2001**, *40*, 6463.
213. He, X.; Trudeau, M.; Antonelli, D. *M. Chem. Mater.* **2001**, *13*, 4808.
214. Fischer, E.; Reckziegel, A. *Chem. Ber.* **1961**, *94*, 2204.
215. Binder, H.; Elschenbroich, C. *Angew. Chem., Int. Ed.* **1973**, *12*, 659.

216. Handbook of X-ray Photoelectron Spectroscopy, Physical Electronics Division, Perkin-Elmer Corp.: Eden Prairie, MN.
217. Hu, X.; Trudeau, M.; Antonelli, D. *Chem. Mater.* **2007**, 19, 1388.
218. Skadtchenko, B.; Trudeau, M.; Kwon, C. W.; Dunn, B.; Antonelli, D. *Chem. Mater.* **2004**, 16, 2886.
219. Ye, B.; Trudeau, M.; Antonelli, D. *Chem. Mater.* **2002**, 14, 2774.
220. Ye, B.; Trudeau, M.; Antonelli, D. *Adv. Mater.* **2001**, 12, 29.
221. Ye, B.; Trudeau, M.; Antonelli, D. *Adv. Mater.* **2001**, 13, 561
222. Ye, B.; Trudeau, M.; Antonelli, D. *Chem. Mater.* **2001**, 13, 2730.
223. Skadtchenko, B.; Trudeau, M.; Schurko, R.; Willans, M.; Antonelli, D. *Adv. Funct. Mater.* **2003**, 13, 671.
224. Skadtchenko, B.; Trudeau, M.; Schurko, R.; Lo, A.; Antonelli, D. *Chem. Mater.* **2005**, 17, 1467.
225. Kosaka, M.; Tanigaki, K.; Prassides, K.; Margadonna, S.; Lappas, A.; Brown, C.; Fitch, A. *Phys. Rev. B* **1999**, 59, 6628.

VITA AUCTORIS

Name: Xin Hu

Place of Birth: Liaoning, China

Year of Birth: 1976

Education: Liaoning University of Science and Technology, China
1994-1998 B. Sc.

Liaoning University of Science and Technology, China
1998-2001 M. Sc.

University of Windsor, Canada
2003-2007 Ph. D.

List of Publications:

1. **Xin Hu**, Boris O. Skadtchenko, Michel Trudeau, David M. Antonelli, "Hydrogen Storage in Chemically Reducible Mesoporous and Microporous Ti Oxides", *Journal of American Chemical Society*, **2006**, 128, 11740–11741.
2. **Xin Hu**, Michel Trudeau, David M. Antonelli, "Hydrogen Storage in Microporous Titanium Oxides Reduced by Early Transition Metal Organometallic Sandwich Compounds", *Chemistry of Materials*, 2007, 19, 1388-1395.
3. **Xin Hu**, Michel Trudeau, David M. Antonelli, "Hydrogen Storage in Mesoporous Titanium Oxides Alkali Fulleride Composites", submitted to *Inorganic Chemistry*.

Presentations:

1. **Xin Hu**, David Antonelli, “Chemically reduced mesoporous and microporous Ti oxides and alkali fulleride composites as novel materials for hydrogen storage”, 234th National Meeting of American Chemical Society, Aug. 19th-23th, **2007**, Boston, Massachusetts, USA. (Poster)
2. **Xin Hu**, David Antonelli, “Hydrogen Storage in Chemically Reducible Mesoporous and Microporous Ti Oxides”, 9th Annual Chemistry and Biochemistry Graduate Research Conference, Nov. 24th-25th, **2006**, Montreal, Québec, Canada. (Poster)
3. **Xin Hu**, David Antonelli, “Mesoporous Ti Oxide Composites of alkali Fullerides and Organometallic Guests: Novel Hydrogen Storage Materials”, 209th Meeting of the Electrochemical Society, May 7th-12th, **2006**, Denver, Colorado, USA. (Co-author)
4. **Xin Hu**, David Antonelli, “Mesoporous Transition Metal Oxides as Novel Materials for Hydrogen Storage”, Pacificchem 2005, Dec. 15th-21st, **2005**, Honolulu, Hawaii, USA. (Oral presenter)